論文 / 著書情報
Article / Book Information

題目(和文)	
Title(English)	Mechanical properties, corrosion behavior and biocompatibility of biodegradable Mg matrix in situ composites
著者(和文)	CaoNguyen Quang
Author(English)	Nguyen Cao
出典(和文)	学位:博士(工学), 学位授与機関:東京工業大学, 報告番号:甲第10947号, 授与年月日:2018年9月20日, 学位の種別:課程博士, 審査員:小林 郁夫,曽根 正人,史 蹟,多田 英司,生駒 俊之
Citation(English)	Degree:Doctor (Engineering), Conferring organization: Tokyo Institute of Technology, Report number:甲第10947号, Conferred date:2018/9/20, Degree Type:Course doctor, Examiner:,,,,
学位種別(和文)	博士論文
Type(English)	Doctoral Thesis

DOCTORAL THESIS

Mechanical properties, corrosion behavior and biocompatibility of biodegradable Mg matrix *in situ* composites

CAO QUANG NGUYEN

Department of Metallurgy and Ceramics Science

Tokyo Institute of Technology

2018

Table of Contents

CHAPTER 1

GENERAL INTRODUCTION

1.1. Motivation

According to the AAOS (American Academy of Orthopedic Surgeons), each year, there are over 6 million bone fractures in the United States [1], this number is predicted to increase significantly in the coming years [2].The illustration of this increasing trend is shown in Figure 1.1 [3]. Specifically, it is estimated that approximately 1 million hip replacements and 250,000 knee replacements are carried out per year. This number is expected to double between 1999 and 2025 as a result of aging populations worldwide and growing demand for a higher quality of life. Another statistical data estimated that by the end of 2030, the number of total hip replacements will increase by 174% and total knee arthoplasties is predicted to grow by 673% from the present rate. Other statistics on hip and knee replacement surgery per 100,000 population in selected countries are shown in Figure 1.2 [4].

Undoubtedly, the increasing demand for implants makes it crucial to accelerate efforts on biomaterial research.

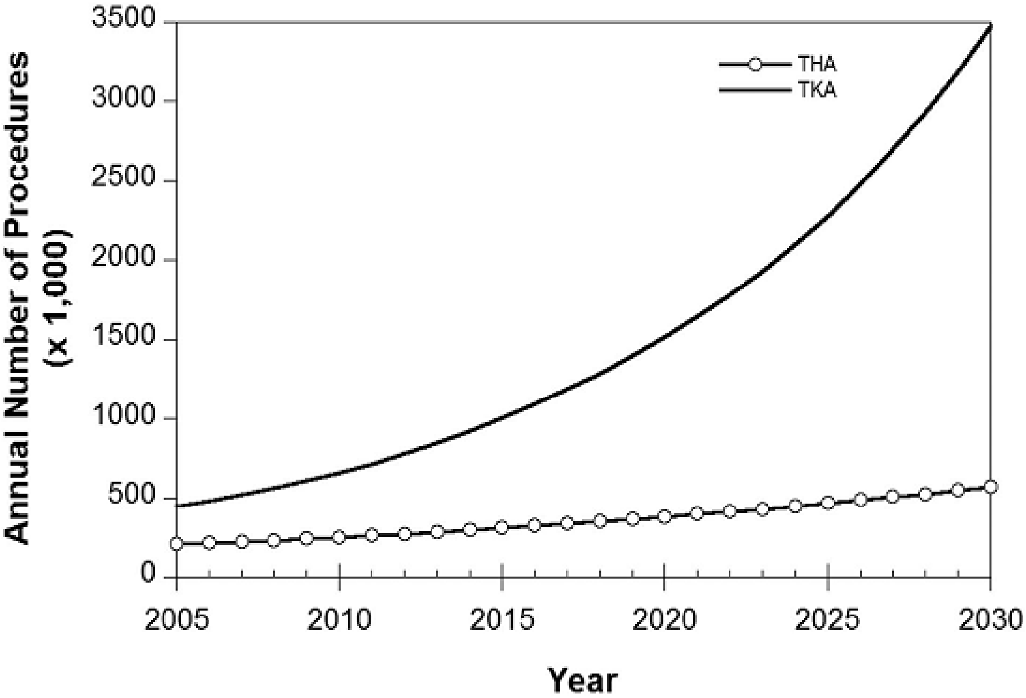

Figure 1.1. The projected number of primary total hip arthroplasty (THA) and Total knee arthroplasty (TKA) procedures in the United States from 2005 to 2030 [3].

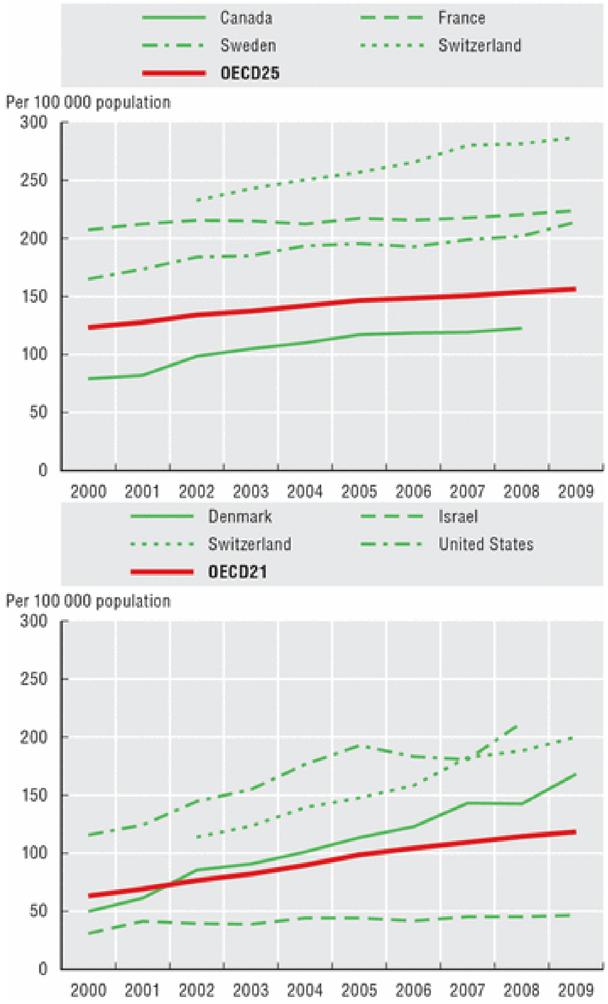

Figure 1.2. Trend in hip and knee replacements per 100,000 population in selected countries

(OECD:Organisation for Economic Co-operation and Development)

(OECD25: average of 25 selected countries)

(OECD 21: average of 21 selected countries)

1.2. Back ground

Looking back to the history of the development of biomaterial during the last 70 years to understand the advancement in biomaterials research and their clinical availability, the evolution process was divided in to three generations, bioinert materials (first generation), bioactive materials (second generation), and biodegradable and bioabsorbable materials (third generation) [5]. In the last decade, there have been an enormous number of researches in Mg based biomaterials since they can be considered as a part of biodegradable and bioabsorbable materials (third generation). Magnesium (Mg) is a light weight metal with density of 1.74 g/cm^3, high specific strength and Young's modulus equivalent to that of bone [6]. In addition, Mg is one of the most essential elements in human body fluid [7,8]. More interestingly, Mg is biodegradable and bioabsorbable [9,10]. These outstanding properties make Mg based materials gain a great interest for biodegradable and bioabsorbable implant applications [9,10].

Currently, Titanium alloys, cobalt-chromium alloys and stainless steels are the most widely applied as implant biomaterials [9,11]. However, these traditional metallic biomaterials raised some issue including: long term bio-incompatibility since released ions may cause infection or inflammation [6, [12-14], high Young's modulus resulting in stress shielding effect [6]. Another disadvantage of above traditional implant materials is that secondary surgery is required to remove the implants from the body after the healing. This secondary surgenry is expensive and latents some risks for patients.

On another hand, Mg with many advantages including low Young's modulus, good biocompatibility, and especially biodegradability is very potential candidate for temporary implant applications. With the biodegradability, Mg based implants do not require the secondary surgery for removal of implant after healing. Figure 1.3 is one example of biodegraded process of Mg implant during 32 weeks of implantation [15]. It can be seen that Mg degraded gradually in the rabbit femur.

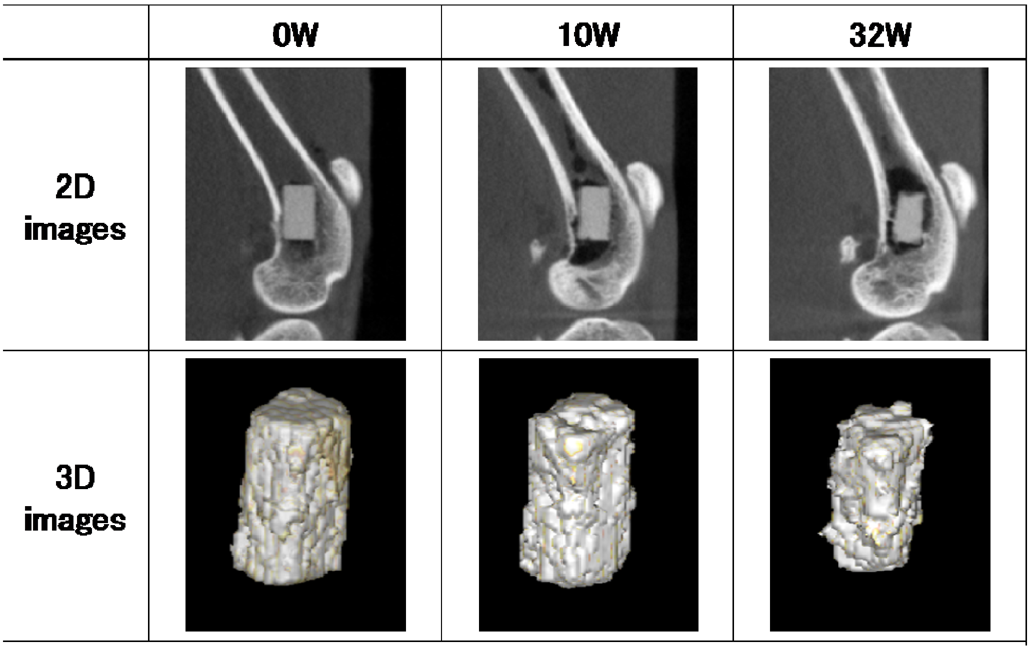

Figure 1.3. Biodegraded process of Mg during implantation into the rabbit femur for 32 weeks.

The major drawback of Mg for temporary implant applications is its fast corrosion rate, which which results in fast deterioration of mechanical properties of the implant before healing process [16]. There are many methods to improve the corrosion resistance of Mg. Among of theses methods, adding reinforcement additive and surface modification are the most atractive for the research. The former is very effective to improve both mechanical properties and corrosion resistance of Mg, while the latter is very effective to enhance the corrosion resistance of Mg significantly [17-22]. However, the selection of additives and surface modification method are very essential, because the additives and surface treatment substances are required to be biocompatible and biodegradable as well. Therefore, the with the purpose of development of new Mg based biomaterials with good mechanical properties, low corrosion rate, and good biocompatibility, both additive and surface modification are applied to improve these properties of Mg based biodegradable implant materials.

1.3. The objective of thesis:

The following objectives are main goals of this doctoral thesis:

(1) Design new Mg matrix *in situ* composites with a controllable corrosion rate and good mechanical properties;

(2) Investigate composition, microstructure and mechanical properties of fabricated composites.

(3) Evaluate corrosion and *in vitro* biocompatibility of the fabricated composites.

(4) Surface modification for fabricated Mg matrix *in situ* composites.

(5) Evaluate corrosion and *in vitro* biocompatibility of the composites after surface modification.

1.4. Mg matrix *in situ* composites

Mg matrix composites belongs to light weight material family and have been applied widely in industry. With high specific strength, biocompatibility and biodegradability [9,10], they would be ideal objective of research on the field of biodegradable materials as well. In recent years, researchers paid a great attention on development of Mg matrix composites for temporary implant applications. However, conventional Mg matrix composites shows limitation in mechanical integrity or corrosion resistance. Such a situation, Mg matrix *in situ* composites could be involved.

In situ composites are multiphase materials where the reinforcing phase is synthesized through chemical reactions within the matrix during composite fabrication. This reinforcing phase is produced as very fine particle form and thermodynamically stable within the matrix resulting in high thermodynamic compatibility at the matrix-reinforcement interface [23,24]. As a result, the *in situ* composites exhibits preeminent mechanical properties [25–28]. In the field of light weight materials, which gain a great interest for industry applications due to their superior specific mechanical properties, Al-based *in situ* composites have been received meticulous attention by researchers [29–33]. On the other hand, researches on Mg based *in situ* composites which recently emerged as not only for industry applications but also are potential candiate for the biodegradable materials is still limitted. Therefore, this project aims to design new Mg matrix *in situ* composites with good mechanical properties as well as controllable corrosion resistance.

1.5. Motivation for selection of additive, fabrication technique and surface modification method

Additive selection:

There are many additive can be reinforcement of Mg matrix composites including ceramics, metals, rare earth elements. However, it should be aware that the reinforcement should be biocompatible and biodegradable. The most popular additives related to aluminum (Al), Aluminum Oxide, and rare earth elements. However, the rare earth elements (Pr, Ce, Y, etc.) might cause hepatotoxicity [34]. Recently researches showed that Zn is an effective additive that improve the mechanical properties as well as corrosion resistance of Mg based biomaterials [35–37]. In addition, Zn is also biocompatible and biodegradable with daily moderate amount of allowance [38,39]. Moreover, the degradation process did not raise the serum Mg^{2+} level and no kidney disorders were observed. Zn is one of the most abundant nutritionally essential elements in the human body [39], and has basic safety for biomedical applications. Furthermore, Zn can improve the corrosion resistance and mechanical properties of magnesium alloys. For example, the corrosion rate of magnesium could be reduced by increasing the mass fraction of Zn in magnesium [35]. Moreover, Zn can effectively strengthen magnesium through a solid solution hardening mechanism [36]. In this study, with the target of employing Zn and its' compounds as reinforcement, Mg matrix *in situ* composites with high mechanical properties for biomaterial applications will be fabricated from homogeneously mixed Mg-ZnO powder.

Fabrication technique selection:

In the last decades, spark plasma sintering (SPS) has received increasing attention as a high-speed powder consolidation technology. During SPS process, spark plasma is generated by direct pulse current and employed simultaneously with a uniaxial pressure on powders. With rapid heating on powders surface, the metal powders with different melting temperatures can be synthesized easily. SPS working temperatures are lower than that of conventional sintering, and its process time is approximately within a range of 10 minutes. These advantages of SPS make it capable to prepare Mg based composites [40,41].

Surface modification selection:

Surface coating is very effective method to enhance the corrosion resistance of materials [17-22]. Especially, hydroxyapatite (HAp) and some other calcium phosphate compounds are potential coating materials to reduce severe corrosion of Mg materials [17-22]. Because HAp is main component of bone and the calcium phosphates precipitated from simulated body fluids enhancing the corrosion resistance of Mg [42,43]. Recent researches of Hiromoto *et al.* demonstrated that HAp grows well on surface of Mg alloys and shows very effective in improvement of corrosion properties and biocompatibility of Mg alloys [44-46]. Therefore, in this project, HAp coating was selected as surface modification method.

In summary, in this project, Mg matrix *in situ* composites were fabricated via SPS from mixed Mg-ZnO powder. The composition, microstructure, mechanical, and corrosion properties of the fabricated composites were evaluated. HAp coating was applied to enhance the corrosion resistance of the composites. The *in vitro* corrosion and biocompatible properties of HAp coated composites were evaluated for practical applications.

Reference

[1] Stevens B, Yang Y, Mohandas A, Stucker B, Nguyen KT. A review of materials, fabrication methods, and strategies used to enhance bone regeneration in engineered bone tissues. J Biomed Mater Res - Part B Appl Biomater. 85, 2008, 573–582.

[2] Kurtz S, Ong K, Lau E, Mowat F, Halpern M. Projections of primary and revision hip and knee arthroplasty in the United States from 2005 to 2030. J Bone Joint Surg Am. 89, 2007, 780–785.

[3] Marjan BN, Mohd RH. Metallic biomaterials of knee and hip - A review. Trends Biomater Artif Organs. 24, 2010, 69–82.

[4] Oecd. Hip and knee replacement. Heal a Glance 2011 OECD Indic 2011:92–93.

[5] Hanson ET, Lewis RL, Auerbach R, Thomson JA. Applica- B. Third-Generation Biomedical Materials 2002:295.

[6] Staiger MP, Pietak AM, Huadmai J, Dias G. Magnesium and its alloys as orthopedic biomaterials: A review. Biomaterials. 27, 2006, 1728-1734.

[7] Saris NE, Mervaala E, Karppanen H, Khawaja JA, Lewenstam A.. Magnesium - An update on physiological, clinical and analytical aspects. Clinica Chimica Acta. 294, 2000, 1-26.

[8] Brink EJ, Beynen AC. Nutrition and magnesium absorption - a review. Progress in Food and Nutrition Science. 16, 1992, 125-162.

[9] Witte F. The history of biodegradable magnesium implants: A review. Acta Biomaterialia. 6, 2010, 1680-1692.

[10] Zeng R, Dietzel W, Witte F, Hort N, Blawert C. Progress and challenge for magnesium alloys as biomaterials. Advanced Engineering Materials. 10, 2008, B3-B14.

[11] Witte F, Fischer J, Nellesen J, Crostack HA, Kaese V, Pisch A, Beckmann FS, Windhagen H. In vitro and in vivo corrosion measurements of magnesium alloys. Biomaterials. 27, 2006, 1013-1018.

[12] Heublein B, Rohde R, Kaese V, Niemeyer M, Hartung W, Haverich A. Biocorrosion of magnesium alloys: a new principle in cardiovascular implant technology? Heart. 89, 2003, 651-656.

[13] Yaremchuk MJ, Fiala TG, Barker F, Ragland R. The effects of rigid fixation on craniofacialgrowth of rhesus-monkeys. Plastic and Reconstructive Surgery. 93, 1994, 1-10.

[14] Gilardino MS, Chen E, Bartlett SP. Choice of internal rigid fixation materials in the treatment of facial fractures. Craniomaxillofacial trauma & reconstruction. 2, 2009, 49-60.

[15] Akane I, Jun T, Toshikazu A, Tomokazu H, Takkan M, Masataka D. Animal study of consecutive CT monitoring of biodegradable materials - biodegradation of pure Mg implanted in rabbit femur. Front. Bioeng. Biotechnol. Conference Abstract: 10th World Biomaterials Congress.

[16] Witte F, Hort N, Vogt C, Cohen S, Kainer KU, Willumeit R, Feyerabend F. Degradable biomaterials based on magnesium corrosion. Curr.Opin.Solid State Mater. Sci. 12, 2008, 63–72.

[17] Al-Abdullat Y, Tsutsumi S, Nakajima N, Ohta M, Kuwahara H, Ikeuchi K. Surface Modification of Magnesium by NaHCO3 and Corrosion Behavior in Hank's solution for New Biomaterial Applications. Mater. Trans. 42, 2001, 1777–1780.

[18] Longchuan L, Jiacheng G, Yong W. Evaluation of cyto-toxicity and corrosion behavior of alkali-heat-treated magnesium in simulated body fluid. Surf. Coat. Tech. 185, 2004, 92–98.

[19] Song YW, Shan DY, Han EH. Electrodeposition of hydroxyapatite coating on AZ91D magnesium alloy for biomaterial application. Mater. Lett. 62, 2008, 3276–3279.

[20] Yang JX, Jiao YP, Cui FZ, Lee IS, Yin QS, Zhang Y. Modification of degradation behavior of magnesium alloy by IBAD coating of calcium phosphate. Surf. Coat. Tech. 202, 2008, 5733–5736.

[21] Cuilian W, Shaokang G, Li P, Chenxing R, Xiang W, Zhonghua H. Characterization and degradation behavior of AZ31 alloy surface modified by bone-like hydroxyapatite for implant applications. Appl. Surf. Sci. 255, 2009, 6433–6438.

[22] Zhang Y, Zhang G, Wei M. Controlling the biodegradation rate of magnesium using biomimetic apatite coating. J. Biomed. Mater. Res. 89B, 2009, 408–414.

[23] Chunxiang C, Shen YT, Meng FB, Kang SB. Review on Fabrication Methods of in situ Metal Matrix Composites, J. Mater. Sci. Technol. 16, 2000, 619–626.

[24] Aikin RM. The Mechanical Properties of In-Situ Composites, JOM. 49, 1997, 35–39.

[25] Zhang Q, Xiao BL, Wang WG, Ma ZY. Reactive mechanism and mechanical properties of in situ composites fabricated from an Al–TiO2 system by friction stir processing, Acta Mater. 60, 2012, 7090–7103.

[26] Hao S, Cui L, Guo F, Liu Y, Shi X, Jiang D, Brown DE, Ren Y. Achieving large linear elasticity and high strength in bulk nanocompsite via synergistic effect, Sci. Rep. 5, 2015, 8892.

[27] Liuyi X, Fen W, Jianfeng Z, Xiaofeng W. Mechanical properties and microstructure of Al2O3/TiAl in situ composites doped with Cr2O3, Mater. Sci. Eng. A. 528, 2011, 3337–3341.

[28] Hyun BL , Hiroyasu T, Equo K, Tatsuo S, Kee DW. Fabrication and Mechanical Properties of Al-Based In Situ Nano-Composites Reinforced by Al2O3 and Intermetallic Compounds, Mater. Trans. 53, 2012, 428–434.

[29] Ramesh CS, Pramod S, Keshavamurthy R. A study on microstructure and mechanical properties of Al 6061–TiB2 in-situ composites, Mater. Sci. Eng. A. 528, 2011, 4125–4132.

[30] Daoush W, Francis A, Lin Y, German R. An exploratory investigation on the in-situ synthesis of SiC/AlN/Al composites by spark plasma sintering, J. Alloys Compd. 622, 2015, 458–462.

[31] Sreekumar VM, Hari BN, Eskin DG, Fan Z. Structure–property analysis of in-situ Al–MgAl2O4 metal matrix composites synthesized using ultrasonic cavitation, Mater. Sci. Eng. A. 628, 2015, 30–40.

[32] Xu K, , Wongpreedee K, Russell AM. Microstructure and strength of a deformation processed Al-20%Sn in situ composite, Scr. Mater. 44, 2001, 935–940.

[33] Ku CH, Pioletti DP, Browne M, Gregson PJ. Effect of different Ti–6Al–4V surface treatments on osteoblasts behaviour. Biomaterials. 23, 2002, 1447–1454.

[34] Nakamura Y, Tsumura Y, Tonogai Y, Shibata T, Ito Y. Differences in behavior among the chlorides of seven rare earth elements administered intravenously to rats. Fundam Appl Toxicol. 37, 1997, 106–116.

[35] Haferkamp H, Bach FW, Kaese V, Möhwald K, Niemeyer M, Schreckenberger H, Tai PT. Magnesium corrosion-processes, protection of anode and cathode. In:Kainer KU, editor. Magnesium-alloys and technology. Weinheim: Wiley-VCH; 2003. p. 226–7.

[36] Peter H, Mordike BL. Physical metallurgy. In: Friedrich HE, Mordike BL, editors. Magnesium technology –metallurgy, design data, applications. Berlin: Springer; 2006. p. 76–7.

[37] Zhang X. In vivo biodegradable binary Mg–Zn alloy. Chinese Patent no. ZL 200510111795.4.

[38] Trumbo P, Yates AA, Schlicker S, Poos M Dietary reference intakes: Vitamin A, Vitamin K, Arsenic, Boron, Chromium, Copper, Iodine, Iron, Manganese, Molybdenum, Nickel, Silicon, Vanadium and Zinc, J. Am. Diet. Assoc. 101, 2001, 294–301.

[39] Tapiero H, Tew KD.. Trace elements in human physiology and pathology: zinc and metallothioneins., Biomed. Pharmacother. 57, 2003, 399–411.

[40] Bowen PK, Shearier ER, Zhao S, Guillory RJ, Zhao F, Goldman J, Drelich JW. Biodegradable Metals for Cardiovascular Stents: from Clinical Concerns to Recent Zn-Alloys. Adv Healthc Mater. 5, 2016, 1121–1140.

[41] Omori M. Sintering, consolidation, reaction and crystal growth by the spark plasma system (SPS). Mater. Sci. Eng. A. 287, 2000, 183–188.

[42] Hideyuki K, Al-Abdullat Y, Naoko M, Sadami T, Tatsuhiko A. Precipitation of Magnesium Apatite on Pure Magnesium Surface during Immersing in Hank's Solution. Mater. Trans. 42, 2001, 1317–1321.

[43] Hiromoto S, Shishido T, Yamamoto A, Maruyama N, Somekawa H, Mukai T. Precipitation control of calcium phosphate on pure magnesium by anodization. Corr. Sci. 50, 2008, 2906–2913.

[44] Hiromoto S, Tomozawa M. Hydroxyapatite coating of AZ31 magnesium alloy by a solution treatment and its corrosion behavior in NaCl solution. Surf. Coat. Technol. 205, 2011, 4711–4719.

[45] Hiromoto S, Tomozawa M. Corrosion Behavior of Magnesium with Hydroxyapatite coatings Formed by Hydrothermal Treatment. Mater. Trans. 51, 2010, 2080–2087.

[46] Hiromoto S, Inoue M, Taguchi T, Yamane M, Ohtsu N. In vitro and in vivo biocompatibility and corrosion behaviour of a bioabsorbable magnesium alloy coated with octacalcium phosphate and hydroxyapatite. Acta Biomater. 11, 2015, 520–530.

CHAPTER 2

EVOLUTIONS OF MICROSTRUCTURE AND MECHANICAL PROPERTIES OF BIOMEDICAL Mg-MATRIX *IN SITU* COMPOSITES

2.1. Introduction

In situ composites are multiphase materials where the reinforcing phase is synthesized through chemical reactions within the matrix during composite fabrication. This reinforcing phase is produced as very fine particle form and thermodynamically stable within the matrix resulting in high thermodynamic compatibility at the matrix-reinforcement interface [1,2]. As a result, the *in situ* composites exhibits preeminent mechanical properties [3–6]. In the field of light weight materials, which gain a great interest for industry applications due to their superior specific mechanical properties, Al-based *in situ* composites have been received meticulous attention by researchers [7–11]. On the other hand, research on Mg based *in situ* composites which recently emerged as not only for industry applications but also are potential candiate for biodegradable materials is still limitted. Magnesium-based materials show their not only biocompatible but also attribute to stimulate bone growth and healing process [12,13]. So far, there have been many researches on Mg matrix composites for biomedical applications. However, as-produced composites either showed limitted mechanical properties [14–16] or not fully biodegradable [17–19] due to very low solubility of reinforcements in vivo [20]. In such situation, Mg matrix *in situ* composites become prospective candidates of research.

Deng *et al* [21] investigated the formation of Mg matrix *in situ* composite from Mg and ZnO as initial powders. The research showed that MgO and intermetallic compounds formed and created reinforcement from *in situ* reactions during sintering process from room temperature to 550 ^{o}C. However, the mechanical performance of the Mg marix *in situ* composite was not revealed. Lei *et al* [22] investigated the corrosion behaviour of Mg matrix *in situ* composites fabricated by hot press from mixed Mg-20 wt% ZnO powder. The result indicated that *in situ* reaction products including MgO and Mg-Zn intermetallic compounds contributed in the considerable improvement of corrosion resistance of the composites. However, the as-produced

Mg matrix *in situ* composites still exhibited poor mechanical performance for practical applications. Recently, researches showed that Zn is an effective additive that improve the mechanical properties as well as corrosion resistance of Mg based biomaterials [23–26]. In addition, Zn is also biocompatible and biodegradable with daily moderate amount of allowance [27,28]. In this study, with the target of employing Zn and its' compounds as reinforcement, Mg matrix *in situ* composites will be fabricated from homogeneously mixed Mg-ZnO powder by Spark Plasma Sintering (SPS) technique.

In the last decades, SPS has received increasing attention as a high-speed powder consolidation technology. During SPS process, spark plasma is generated by direct pulse current and employed simultaneously with a uniaxial pressure on powders. With rapid heating on powders surface, the metal powders with different melting temperatures can be synthesized easily. SPS working temperatures are lower than that of conventional sintering, and its process time is approximately within a range of 10 minutes. These advantages of SPS make it capable to prepare Mg based composites[29,30].

2.2. Experimental Procedures

Figure 2.1 illustrates the general experiment procedure of this chapter.

At the beginning, Mg and ZnO powder were mixed, then Spark Plasma Sintering or Differential Thermal Analysis (DTA).

The sintered samples were characterized by X-ray diffractometry (XRD), Optical Microscopy (OM), Scanning Electron Microscopy (SEM), energy dispersive X-ray spectroscopy (EDS). The mechanical properties ò the composites were evaluated by micro Vicker's hardness tests and compression tests.

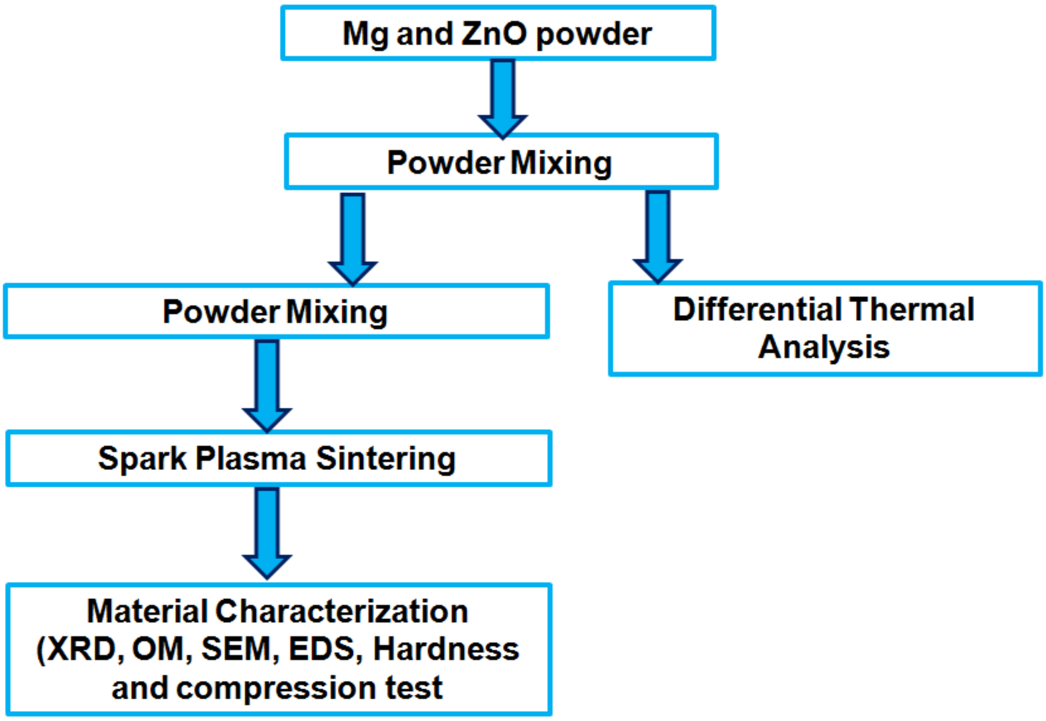

Figure 2.1. Schematic illustration of experiment procedure.

2.2.1. Powder Mixing

Mg powder of 99.5% purity, 180 μm grain size and ZnO of 99.9% purity, 1 μm grain size supplied by Kujundo Chemical Laboratory were used for sample preparation.

Various mass ratios of Mg/ZnO including Mg-50 mass% ZnO, Mg-20 mass% ZnO, Mg-10 mass% ZnO and Mg-5 mass% ZnO powders were mixed in argon atmosphere by a Planetary micro mill pulverisette 7 classic line for different purposes of investigation.

2.2.2. Differential Thermal Analysis

Thermo plus EVO II TG8120, Rigaku Differential Thermal Analysis (DTA) was conducted on well-mixed Mg-50 mass% ZnO powders to determine possible *in situ* reactions occurred. In the analysis process, the powder was heating from room temperature up to 550 ^{o}C in argon atmosphere with the heating rate of 10 ^{o}C per minute.

2.2.3. Sample Sintering

Homogeneously mixed powder was set inside the Tungsten-Carbide die with 120 mm in length and 15mm in diameter for sample sintering by 511S, Syntex SPS system.

In order to avoid leakage of liquid phase possibly produced during sintering process[21], the powder was set inside the SPS die with 120 mm in length and 15mm in diameter as model described in figure 2.2. Firstly, Alumina powder was set into the bottom of the Tungsten Carbide die, then well-mixed Mg-ZnO powder was set onto Alumina powder inside the die, finally, Alumina powder was set onto the top of the die. This will ensure that, even there is liquide phase formed during sintering process, it cannot be leaked out during sintering.

After setting inside the die, the powder was applied under pressure of 10MPa in 1 minute to form green compacts. And then the die was set into furnace of SPS system.

Mg-50 mass% ZnO compacts were used for sintering by SPS at 450, 500 and 550 ^{o}C in 30 minutes with pressure of 50 MPa and heating rate of 50 ^{o}C per minute.

Mg-50 mass% ZnO compacts was also used for sintering in a vacuum furnace without pressure at 500 and 550 °C in 30 minutes for investigating the effect of pressure on the composition and microstructure evolutions of the composites.

For the purpose of implant applications, since Zn is biocompatible with moderate amount of using [26,28] but harmful with excessive amount of allowance [27], composites with smaller fractions of ZnO should be produced. In this work, Mg-5 mass% ZnO, Mg-10 mass% ZnO and Mg-20 mass% ZnO compacts were used for SPS at 550 °C in 30 minutes with pressure of 50MPa and heating rate of 50°C per minute.

All sintering processes were carried out in high vacuum chamber of SPS system vacuum furnace. After sintering, the SPS system was powered off for cooling down the samples to room temperature inside the vacuum furnace.

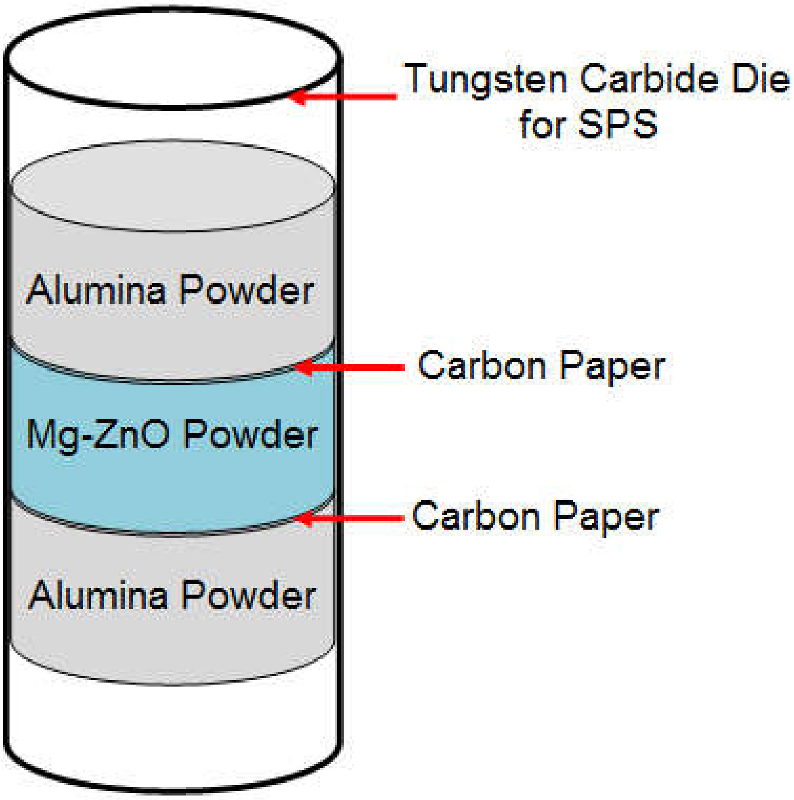

Figure 2.2. Model of setting powder inside SPS die

2.2.4. Material Characterization

a) Composition and microstructure analysis

Sintered composites were cut into plate shape with the size of 10x5x2 (mm), then polishing by SiC papers up to 4000 grit, successively polished with ¼ µm diamond paste, ultrasonically cleaned by ethanol and dried before characterization. X-ray diffractometry (XRD) was conducted by RINT2100 RIGAKU diffractometer for composition analysis. The samples were exposed to Cu K_α radiation ($\lambda = 0.15406$ nm) at a scanning speed of 10 degree per minute. Optical micrographs were obtained from Olympus GX71 Optical Microscope. Further microstructure and composition characterization analyzed by Scanning Electron Microscopy (SEM) and energy dispersive X-ray spectroscopy (EDS) were conducted by JEOL JSM 7000F Field Emission Scanning Electron Microscope.

b) Mechanical property evaluation

Mechanical behaviour of the composites was examined by micro Vicker's Hardness tests and compression tests. Pure sintered Mg was also evaluated for comparison.

Micro Vicker's Hardness tests were performed according to ASTM E384 standard [31] by Matsuzawa MMT X3A automatic digital micro hardness testing system.

Shimadzu SFL-100KNAG mechanical testing machine was employed for compression tests according to ASTM E9-89a standard [32].

2.3. Results and Discussion

2.3.1. *In situ* reactions

Figure 2.3 shows DTA curve conducted on well-mixed Mg-50 mass% ZnO powder from room temperature up to 550 ^{o}C. As shown, there was one exothermic peak started at about 480 ^{o}C. This indicated that there was at least one *in situ* reaction occurred at about this temperature.

In order to further investigate the details of these *in situ* reactions, XRD patterns of composites sintered at 450, 500 and 550 ^{o}C in 30 minutes were observed showing on Figure 2.4. As could be seen that, for the composite sintered at 450 ^{o}C, there were only peaks corresponding to α-Mg and ZnO identified, while peaks of Zn and MgO were detected accompanied with peaks of α-Mg and ZnO for the sample sintered at 500 °C. This suggested that Zn and MgO are reaction products of *in situ* reaction detected at about 480 °C on DTA curve. In other words, the *in situ* reaction could be expressed as following chemical equation [21,22]:

$$Mg_{(s)} + ZnO_{(s)} \xrightarrow{480\,^{\circ}C} MgO_{(s)} + Zn_{(l)} \tag{1}$$

Where the subscripts (s) and (l) refer to solid and liquid state, respectively.

This result is in accordance with findings reported in previous work [21] except the temperature of the *in situ* reaction. The difference of this temperature may come from effect of pressure applied on the powder or the atmosphere of DTA process. In this work, there was no pressure apply on the mixed powder before conducting DTA and the process was carried out in argon atmosphere.

Further comparison between XRD patterns of composites sintered at 500 and 550 °C indicated that, except peaks belong to α-Mg, ZnO, Zn and MgO, there were peaks of intermetallic compounds detected for the composite sintered at 550 °C. Specifically, peaks corrosponding to MgZn, Mg_2Zn_3 and Mg_7Zn_3intermetallics were identified. Accordingly, it is predicted that following *in situ* reactions occurred during heating process from 500 to 550 °C and cooling process [21,22].

$$Mg_{(s)} + Zn_{(l)} \xrightarrow{500-550\,^{\circ}C} Mg\text{-}Zn_{(l)} \tag{2}$$

$$Mg\text{-}Zn_{(l)} \xrightarrow{Cooling} Mg_xZn_y \tag{3}$$

Where Mg_xZn_y includes MgZn, Mg_2Zn_3 and Mg_7Zn_3 intermetallic compounds.

Scanning Electron Microscopy images revealing microstructure of Mg-50 mass% ZnO composites sintered at 450, 500 and 550 °C in 30 minutes are showed in Figure 2.5. Comparison between SEM images of samples sintered at 450 and 500 °C give confirmation of DTA and XRD results.

As shown in Figure 2.5(a), the composite sintered at 450 °C was composed of two identifiable phases, the dark region is α-Mg phase and ZnO displays brightness on SEM image since it is non conductive. This could be taken from EDS analysis of composites sintered at 500 ^{o}C as shown in Figure 2.6. The composition of area marked 001 in Figure 2.6(a) is indicated in Figure 2.6(b), it could be seen that the atomic ratio of Zn:O in this region is approximately 1:1, this implies that this phase is ZnO. The composition of region marked 002 is shown in Figure 2.6(c), as could be seen that this phase contains only α-Mg. This demonstrated that there was no reaction occurred below 450 ^{o}C.

On the other hand, for the composite sintered at 500 ^{o}C, there are three different phase constituents as shown in Figure 2.5(b). The composition of each phase was analyzed as Figure 2.7. As shown, the composition of region marked 001 in figure 2.7(a) is indicated in Figure 2.7(b), the atomic ratio of Zn:O in this region is approximately 1:1, this implies that this phase is ZnO. The composition of region marked 002 in Figure 2.7(a) is shown in Figure 2.7(c). As shown, this region contains Mg, Zn and O with atomic ration of 17 : 36 :46, this indicated that, the constituent should include MgO, ZnO and Zn. The composition of phase marked 003 in Figure 2.7(a) is shown in figure 2.7d, it is clearly that this phase contains only α-Mg. This result is in agreement with DTA and XRD result which showed*in situ* reaction (1) occurred at about 480 ^{o}C and the reaction products are MgO and Zn.

For the composite sintered at 550^{o}C, the main constituent is reaction products which appeared as similar colouring of reaction product region on SEM image of composite sintered at 500 ^{o}C. EDS analysis shown in Figure 2.8 indicated that this reaction product region was composed of Zn, MgO, Mg and ZnO remained, and some kinds of intermetallic compounds. Combination with XRD pattern of this sample, it is predicted that these intermetallic compounds consist of MgZn, Mg_2Zn_3 and Mg_7Zn_3. This result is consistent with the prediction related to *in situ* reactions (2) and (3) occurring during sintering and cooling process, respectively. There was small fraction of remained Mg displayed as dark region on SEM image of the composite sintered at 550 ^{o}C, this indicates that the majority of Mg was involved in *in situ* reaction during sintering process.

The above analysis was additionally confirmed by optical images in Figure 2.9. Since the composite sintered at 450 ^{o}C consisted of only white region of α-Mg phase and grey ZnO, while the composite sintered at 500 ^{o}C included brown region of reaction products accompanied with region of α-Mg phase and grey ZnO. For the composite sintered at 550 ^{o}C, the brown region is reponsible for reaction product phase, while randomly detected white particles are remained α-Mg.

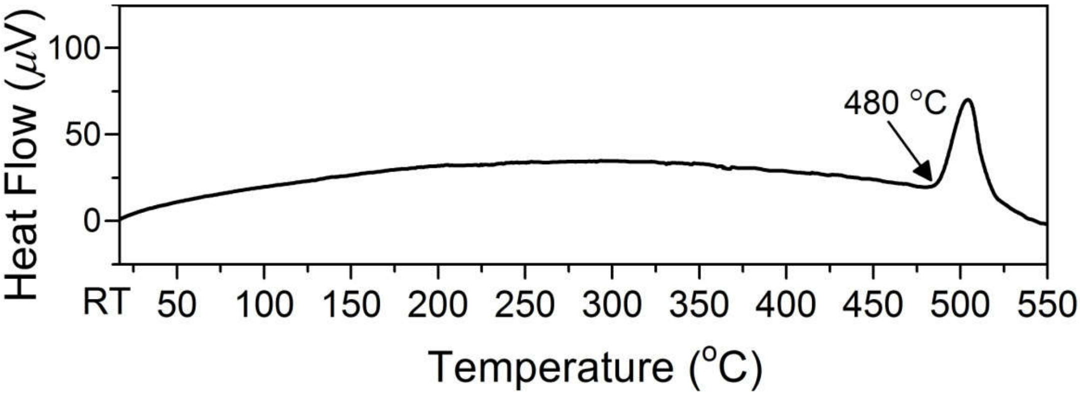

Figure 2.3. DTA curve conducting on Mg- 50 mass% ZnO powder from room temperature to 550 ^{o}C with heating rate of 10 ^{o}C per minute in argon atmosphere.

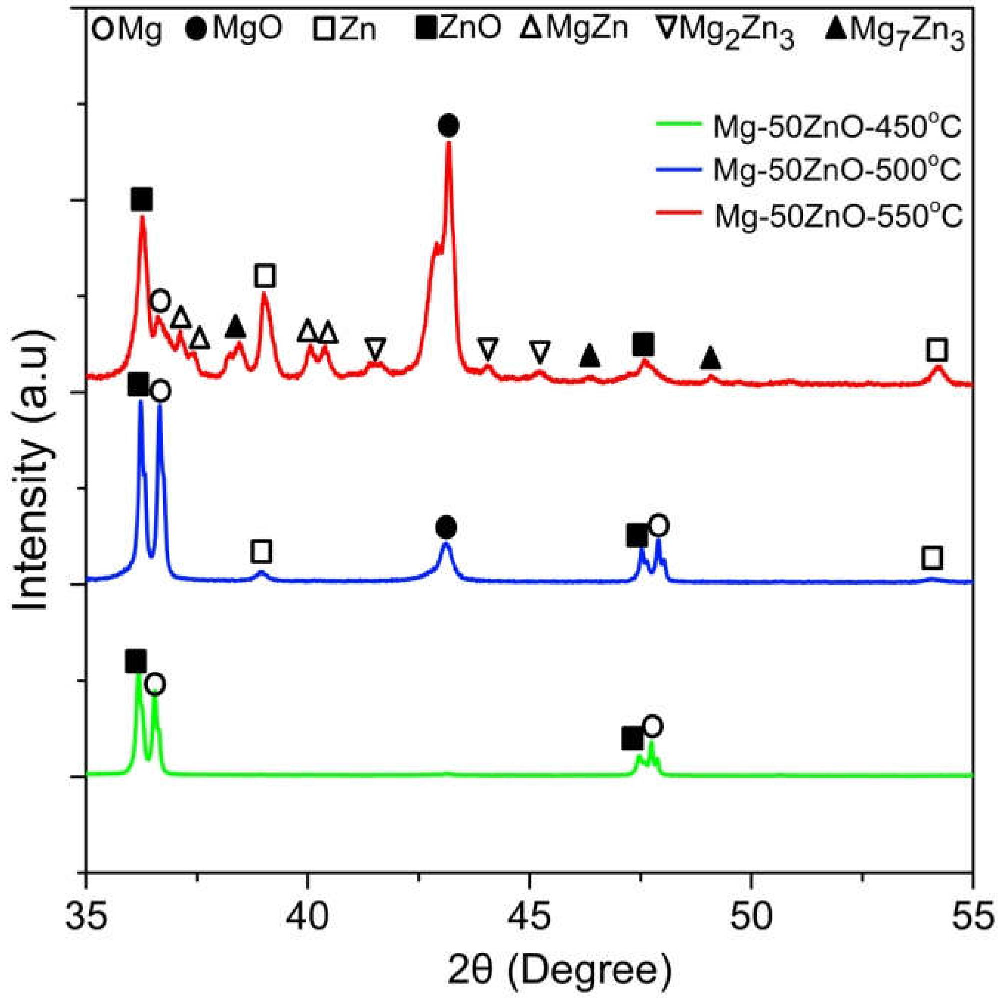

Figure 2.4. XRD patterns of Mg-50 mass% ZnO composites sintered by SPS at 450, 500 and 550 °C.

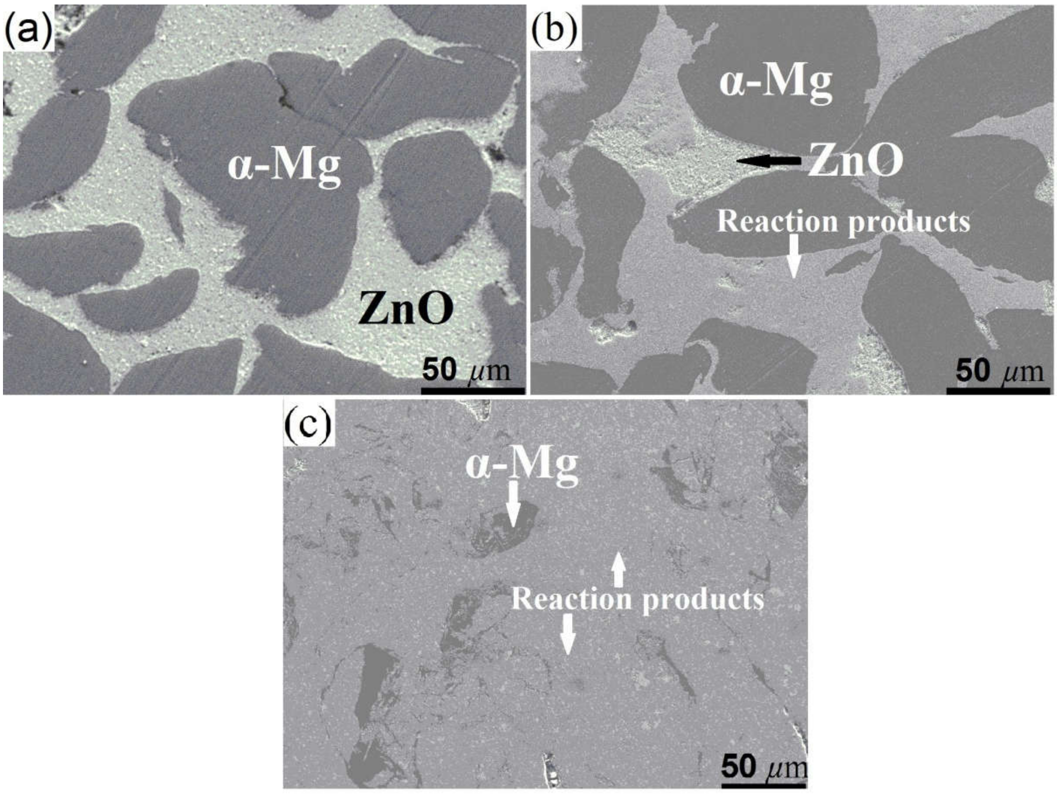

Figure 2.5. SEM micrographs of Mg-50 mass% ZnO composites sintered by SPS at (a): 450 °C, (b): 500 °C, and (c): 550 °C

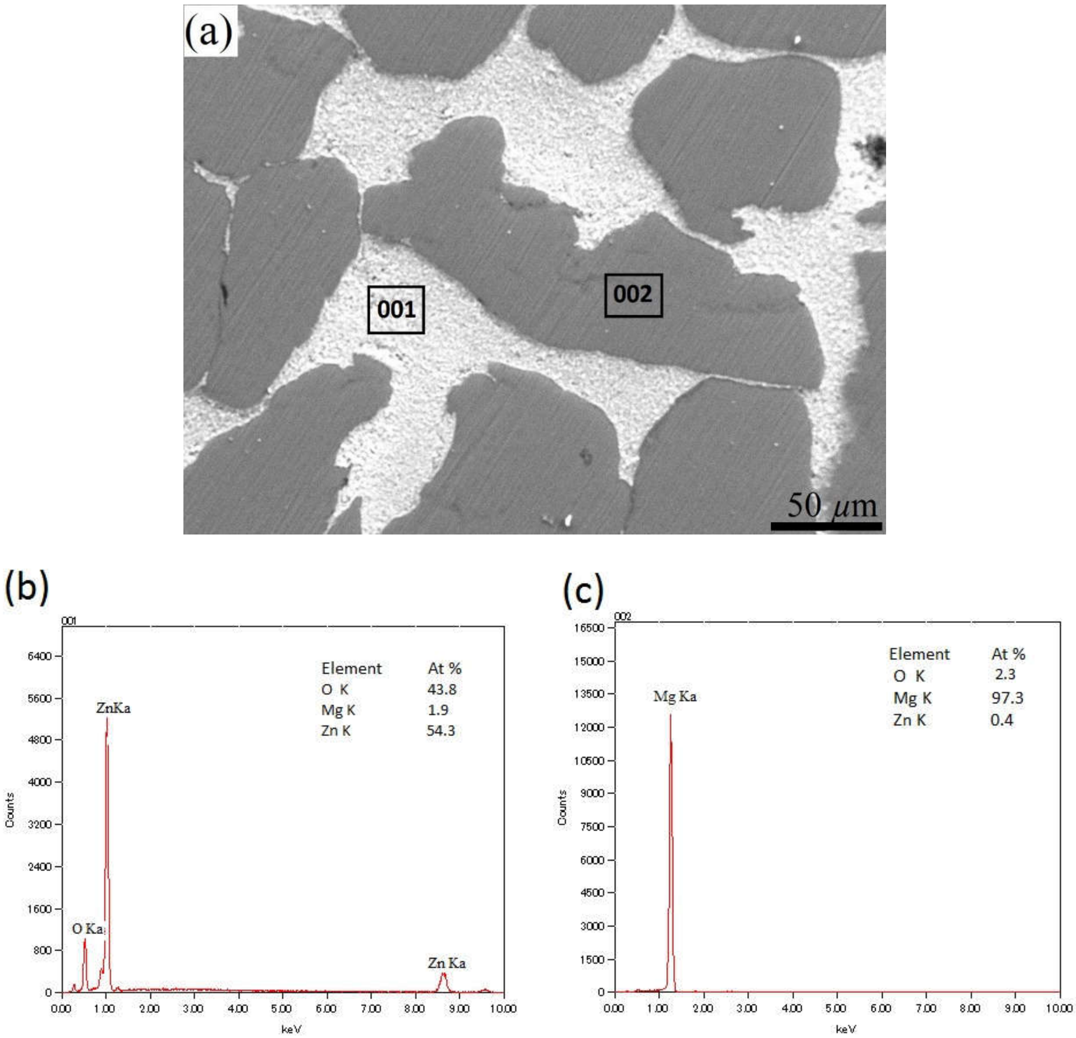

Figure 2.6. SEM-EDS analysis of composite sintered at 450 °C

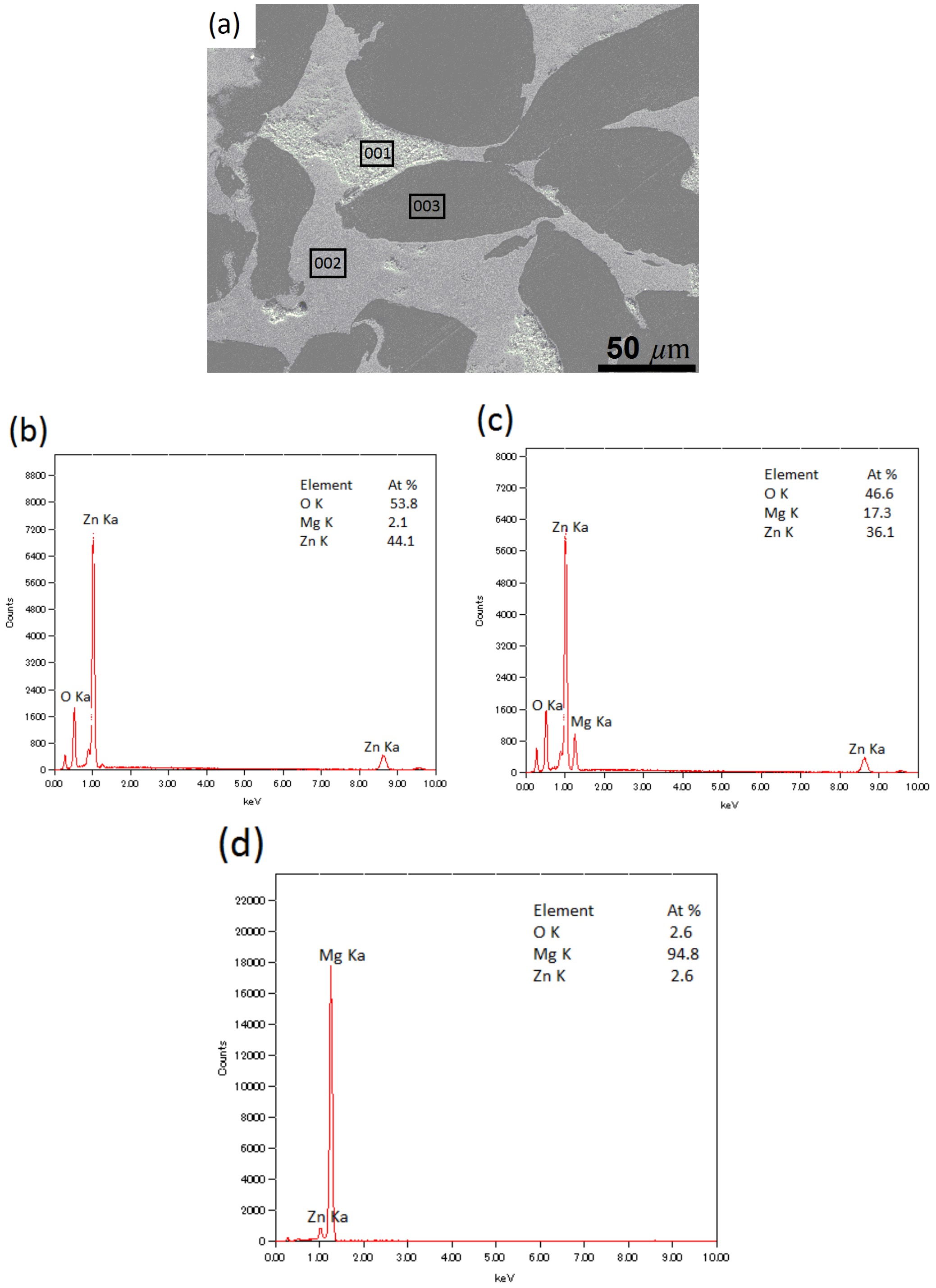

(b)

Element	At %
O K	53.8
Mg K	2.1
Zn K	44.1

(c)

Element	At %
O K	46.6
Mg K	17.3
Zn K	36.1

(d)

Element	At %
O K	2.6
Mg K	94.8
Zn K	2.6

Figure 2.7. SEM-EDS analysis of composite sintered at 500 ^{o}C

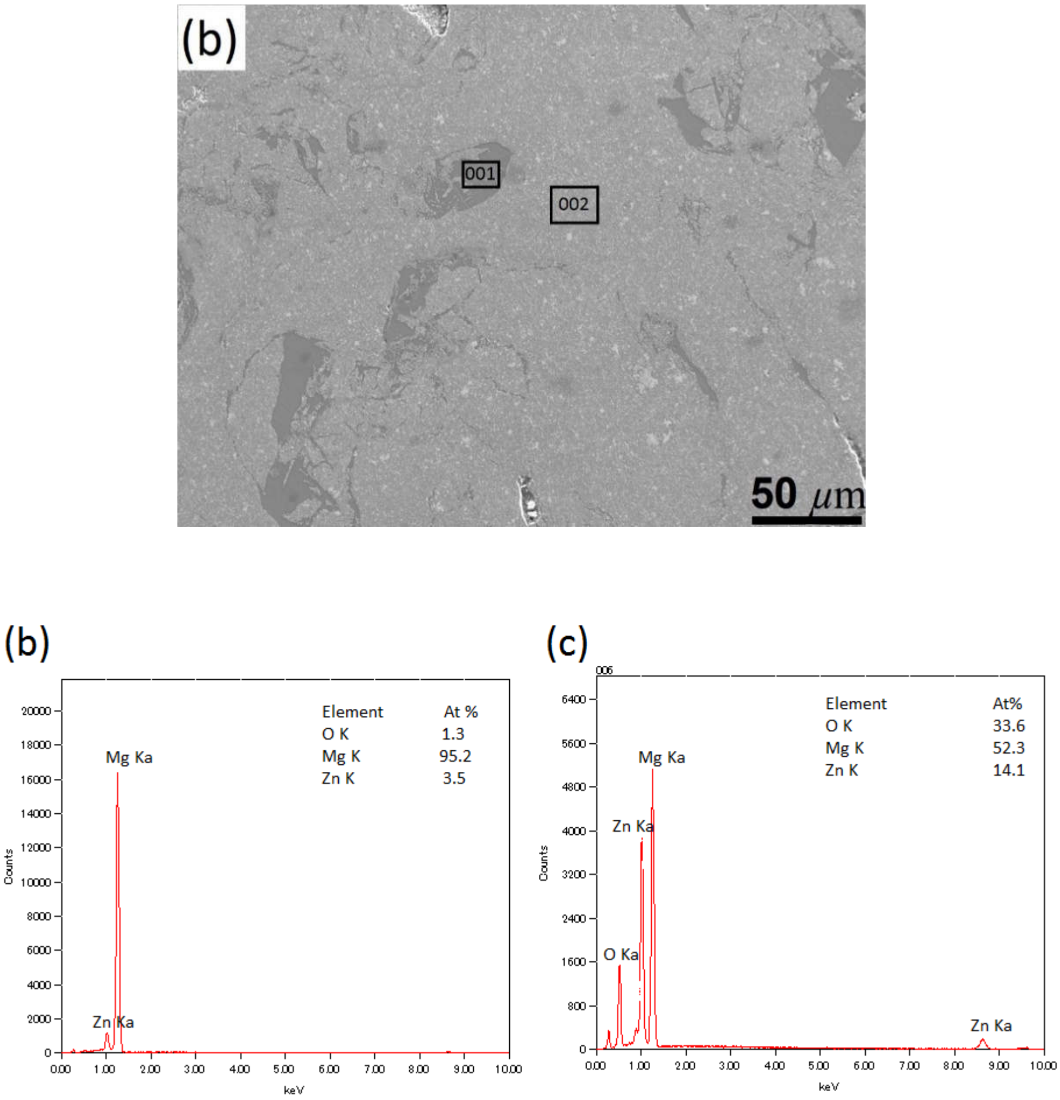

Figure 2.8. SEM-EDS analysis of composite sintered at 550 ^{o}C

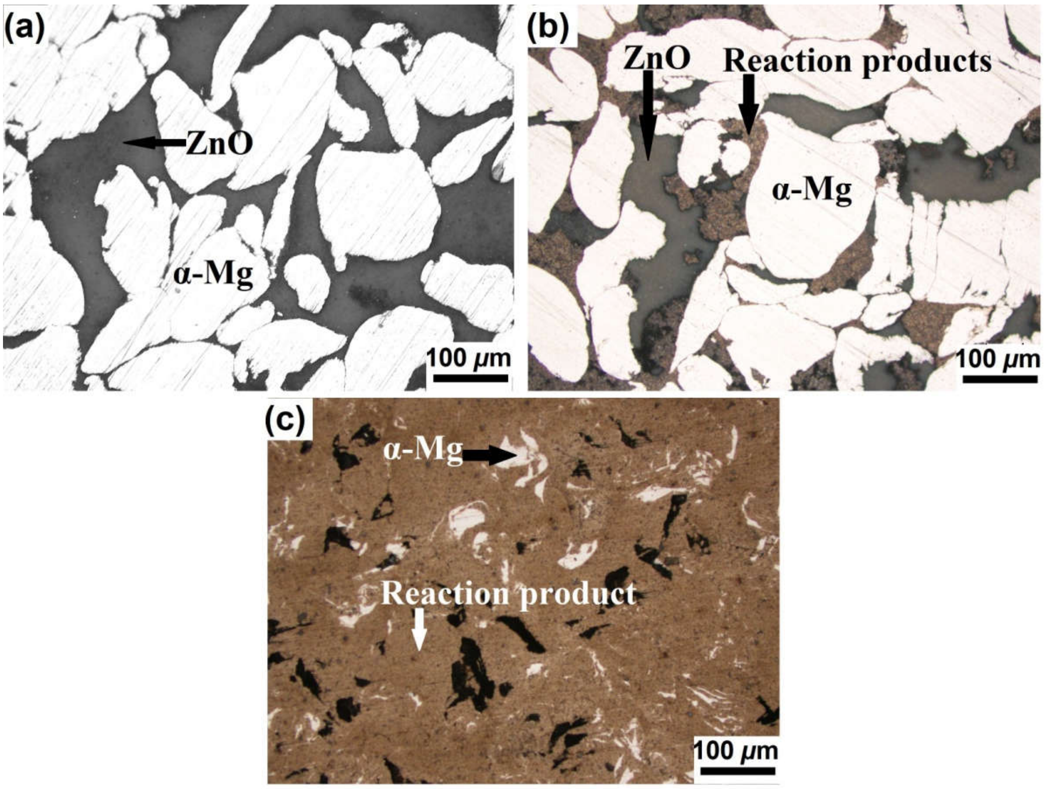

Figure 2.9. Optical Micrographs of Mg-50 mass% ZnO composites sintered by SPS at 450, 500 and 550 °C.

2.3.2. Effect of pressure on the *in situ* reactions

It should be noticed that there was conflict between DTA result showed in Fig. 1 and XRD-SEM-EDS analysis since there was no peak of reaction detected in the range of 500-550 ^{o}C on the DTA curve, however, XRD, SEM and EDS analysis demonstrated that reaction (2) occurred during heating process from 500 to 550 ^{o}C. This conflict may come from effect of pressure applying on the powder during heating process and will be described in details as following.

Figure 2.10 provides comparison between XRD patterns of Mg-50 mass% ZnO composites sintered at 500 ^{o}C in 30 minutes by vacuum furnace without pressure and by SPS with pressure of 50 MPa. As shown in the graph, only difference between these two XRD patterns is intensity of the peaks, especially, peaks related to reaction products including MgO and Zn. The intensity of Zn and MgO peaks of sample sintered by SPS is higher than those of sample sintered by vacuum furnace. This implied that pressure only have effect on the rate of *in situ* reaction (1) but not responsible for activating this reaction. The higher pressure applied on the powder, the higher amount of reaction products produced. Without pressure applied, the reaction (1) still occurred, however, the reaction rate became slow and smaller amount of reation products formed resulting in lower intensity of Zn and MgO peaks for this sample. This effect is also illustrated in Figure 2.11 since SEM image of sample sintered by vacuum furnace showed less fraction of reaction products and more remained ZnO fraction compared to those of sample sintered by SPS.

On the other hand, comparison of XRD patterns and SEM images of composites sintered at 500 and 550 ^{o}C indicated that applied pressure plays an important role in activating the *in situ* reaction (2). As shown in Figure 2.12, XRD patterns indicated that reaction products of Mg-50 mass% ZnO composites sintered at 500 ^{o}C in 30 minutes by vacuum furnace without pressure consisted of only Zn and MgO, while the sample sintered at 550 ^{o}C by SPS with pressure of 50 MPa showed presence of Mg-Zn intermetallic compounds beside Zn and MgO. This implied that the *in situ* reaction (2) was not occurred in the sample sintered by vacuum furnace where no pressure applied during sintering process, however, this reation occurred in the sample sintered by SPS with pressure of 50 MPa applying during sintering. It is predicted that, for the sample sintered by vacuum furnace, new MgO produced from *in situ* reaction (1) formed boundaries or shell layers to avoid Mg reacting with newly formed Zn, while for the sample sintered by SPS, high pressure broke down these MgO shell layers, then Mg easily reacted with newly formed Zn. Thus, the convincing explanation for the confliction between DTA result and XRD-SEM-EDS result came from effect of pressure. Since during DTA process, there was no pressure applied on the powder, therefore, the reaction (2) did not occurred, consequently, peaks related to this reaction was not found from DTA curve. On the contrary, for the sample sintered by SPS, high pressure contributed as activating agent for the reaction (2). As a result, Mg-Zn intermetallic compounds were detected from this sample.

The effect of pressure as activating agent of *in situ* reaction (2) was further confirmed by SEM micrographs as shown in Figure 2.13. There was distinct difference between microstructure of these two samples. The sample sintered by vacuum furnace consisted of three different phases corresponding to α-Mg, ZnO and reaction product phase of *in situ* reaction (1), while the sample sintered by SPS as analysed previously consisted of reaction products of both *in situ* reactions (1) and (2) as main constituent.

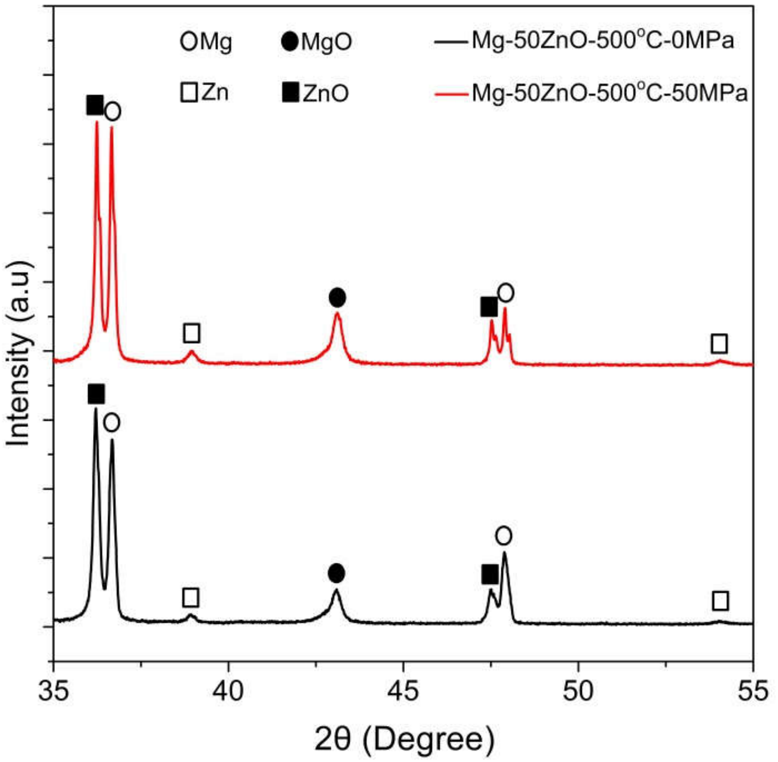

Figure 2.10. XRD patterns of Mg-50 mass% ZnO composites sintered at 500 °C by vacuum furnace without pressure and by SPS under pressure of 50 MPa.

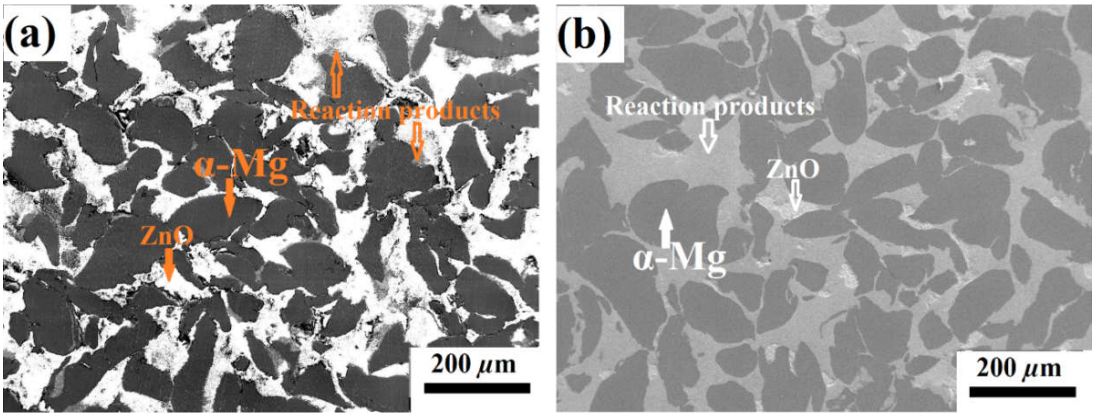

Figure 2.11. SEM micrographs of Mg-50 mass% ZnO composites sintered at 500 °C: (a) by vacuum furnace without pressure, (b) by SPS under pressure of 50 MPa.

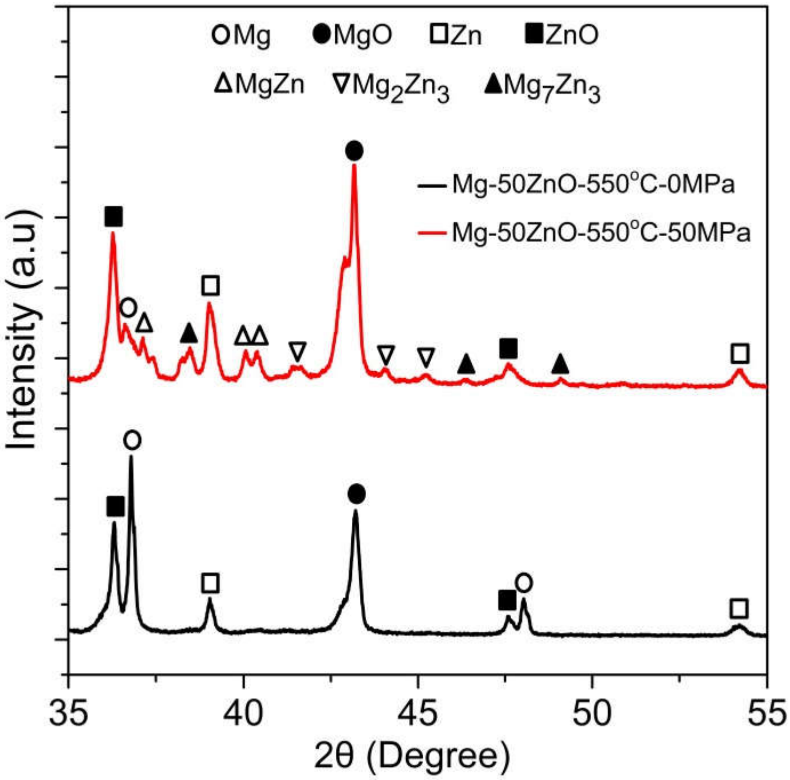

Figure 2.12. XRD patterns of Mg-50 mass% ZnO composites sintered at 550 °C by vacuum furnace without pressure and by SPS under pressure of 50 MPa.

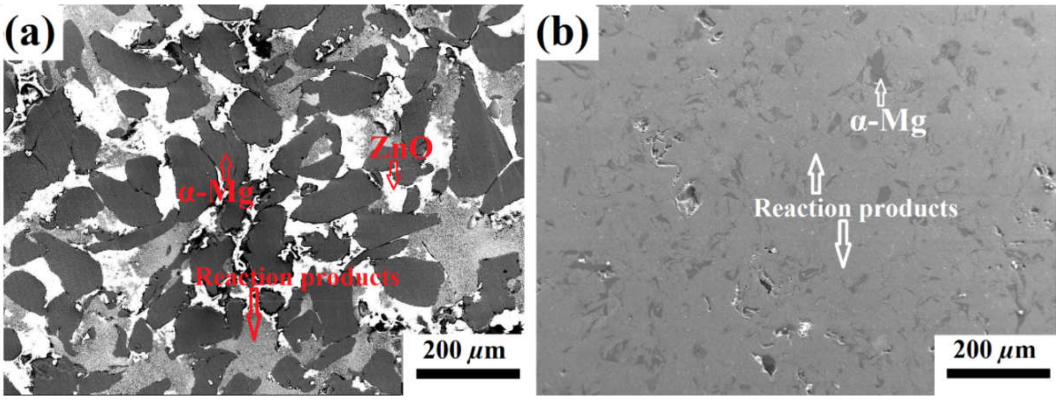

Figure 2.13. SEM micrographs of Mg-50 mass% ZnO composites sintered at 550 ^{o}C: (a) by vacuum furnace without pressure, (b) by SPS under pressure of 50 MPa.

2.3.3. Composites with lower fraction of ZnO for biomedical applications.

a) Microstructure

Figure 2.14-(a), (b) and (c) show optical micrographs of Mg-5 mass% ZnO, Mg-10 mass% ZnO and Mg-20 mass% ZnO composites. All the samples were sintered by SPS at the same conditions of 550 ^{o}C in 30 minutes with pressure of 50 MPa. As shown, there were reaction products distributed quite uniformly in α-Mg particles and almost no remarkable aggregation found. In addition, the density of reaction products increased with the weight fraction of initial ZnO powder. Figure. 2.14-(d), (e) and (f) show optical micrographs of Mg-5 mass% ZnO, Mg-10 mass% ZnO and Mg-20 mass% ZnO composites with higher magnification. As could be seen that, there was almost no ZnO remained in the samples of Mg-5 mass% ZnO and Mg-10 mass% ZnO composites, while there were black ZnO particles remained randomly distributed in reaction product phase of Mg-20 mass% ZnO sample. This indicated that, with sintering time of 30 minutes, *in situ* reaction (1) occurred completely in the Mg-5 mass% ZnO and Mg-10 mass% ZnO samples, however, this reaction was not finished in the Mg-20 mass% ZnO sample. These high magnified images also show well bonding between reaction product phase and α-Mg matrix indicating high quality of sintering of these composites.

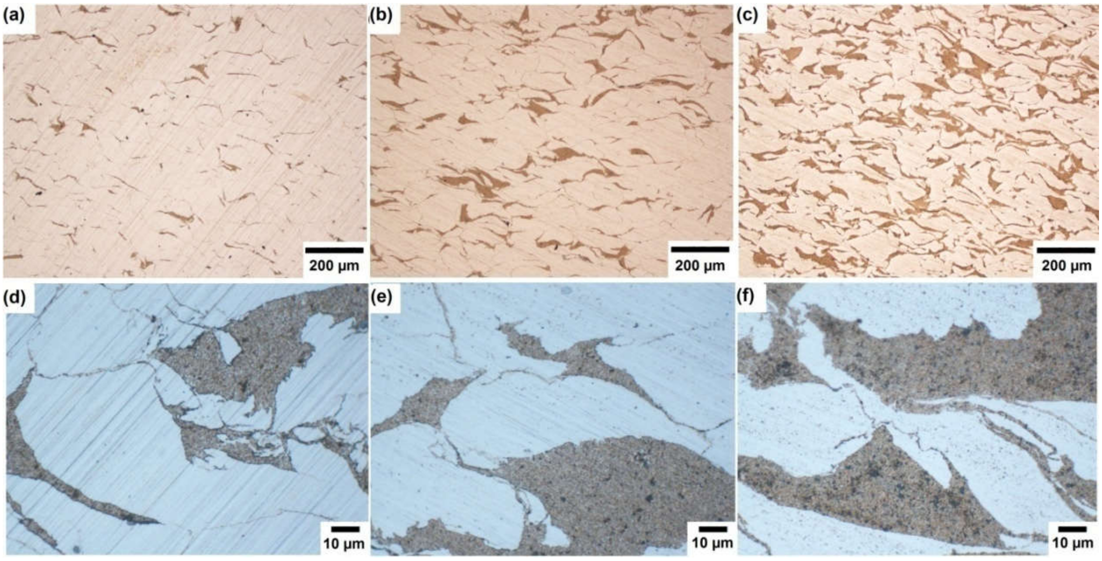

Figure 2.14. optical micrographs of Mg-5 mass% ZnO, Mg-10 mass% ZnO and Mg-20 mass% ZnO composites.

b) *Mechanical properties*

Hardness

Figure 2.16 shows the results of micro Vicker's Hardness tests of pure Mg, Mg-5 mass% ZnO, Mg-10 mass% ZnO, and Mg-20 mass% ZnO composites. From microstructure of these composites, it can be seen obviously two different regions of α-Mg and reaction product phase. Therefore, micro Vicker's hardness tests were conducted separately on each region as illustrated in Figure 2.15. For each region, 5 tests were conducted randomly and the values were then taken average. As shown in Figure 2.16, the hardness of α-Mg improved gradually with the increase of ZnO fraction. While the hardness of α-Mg phase in pure sinter Mg sample was 40 Hv only, this value of the composites were 53 Hv, 57 Hv and 64 Hv for Mg-5 mass% ZnO, Mg-10 mass% ZnO, and Mg-20 mass% ZnO sample, respectively. This suggested that there was positive effect of reaction products on the hardness of α-Mg phase of these composites and this effect became stronger with the increase of initial ZnO fraction. On the other hand, the hardness of reaction product phases were much higher than that of α-Mg phase. Similar trend in increase of hardness with the higher fraction of initial ZnO was achieved. Specifically, hardness of reaction product phase in the Mg-5 mass% ZnO composite was 158 Hv, this increased to 192 Hv for the Mg-10 mass% ZnO sample, and reached the highest at 195 Hv for the Mg-20 mass% ZnO sample.

Compression Tests

Figure 2.17. shows compression stress-strain curves of pure Mg, Mg-5 mass% ZnO, Mg-10 mass% ZnO and Mg-20 mass% ZnO composites sintered at 550 ^{o}C. As could be seen that, Mg-matrix *in situ* composites exhibited not only much higher compression strengths but also higher strains at failure compared to those of pure Mg. Specifically, the highest strength at 380 MPa was observed in Mg-20 mass% ZnO composite, and the highest failure strain at 12.9% was achieved in Mg-5 mass% composite compared to 156 MPa strength and 10.2% failure strain of pure Mg 10.2%. These improvements in the strength and ductility of the composites are attributed as the positive effects of *in situ* reaction products, which act as reinforcements increasing both strength and ductility. As indicated from XRD analysis, there were liquid phases of Zn and Mg-Zn intermetallics formed from *in situ* reactions during

sintering. These liquid phases created well bonding of both Mg particles-reinforcements and Mg-Mg particles resulting in improvement of both strength and failure strain of the composites. In other words, the formation of liquid *in situ* products strongly contributed to the enhancement of strength and ductility of the fabricated composites compared to pure Mg. Further comparison between as-produced composites and cortical bones indicated that the strength of the composites are much higher than that of cortical bones (100-230MPa) [33]. On another aspect, the failure strain of the composites decreased with the increase of ZnO fraction. This is due to the effect of ZnO remained. As indicated from previous works [34–36] since ZnO and metal oxides are reinforcements which improve the strength however has negative effect on the ductility of the composites. Since Mg-20 mass% ZnO sample has highest amount of ZnO remained, the failure strain of this sample is lowest at 11.2%, while Mg-5 mas% ZnO composite with almost no ZnO remained has highest failure strain at 12.9%.

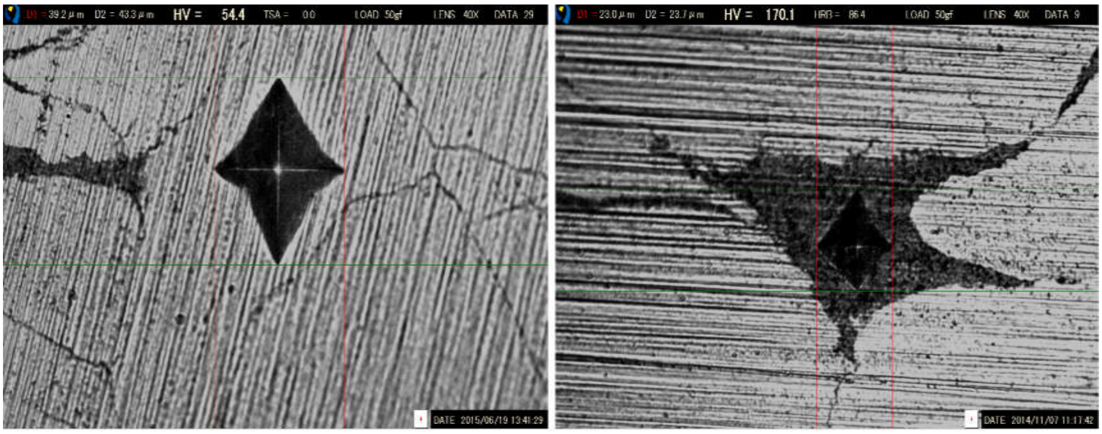

a) b)

Figure 2.15. Illustration of hardness measurement on: a) Mg matrix phase, b) reaction product phase.

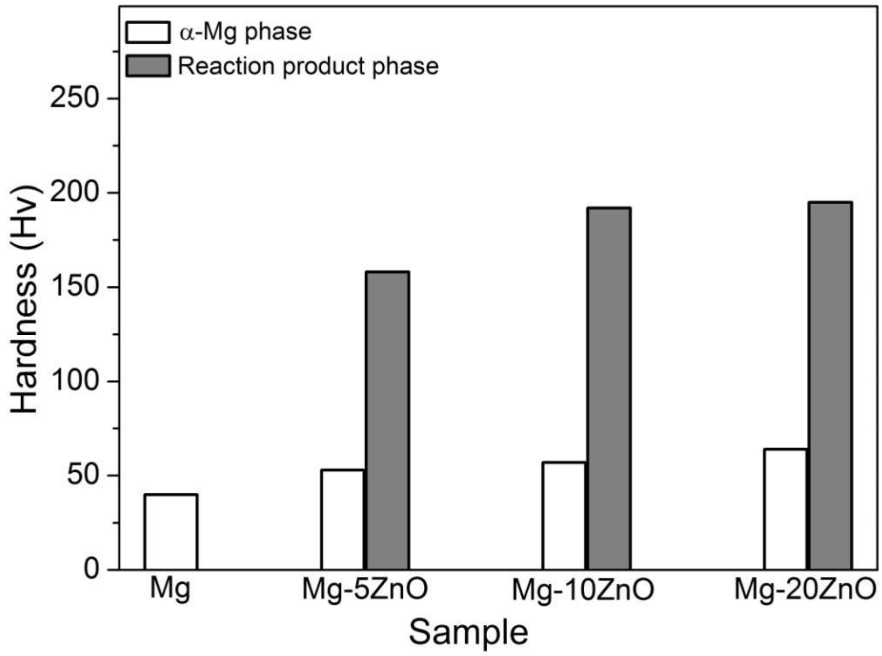

Figure 2.16. Hardness of Mg-5 mass% ZnO, Mg-10 mass% ZnO and Mg-20 mass% ZnO composites sintered at 550 °C by SPS in 30 minutes.

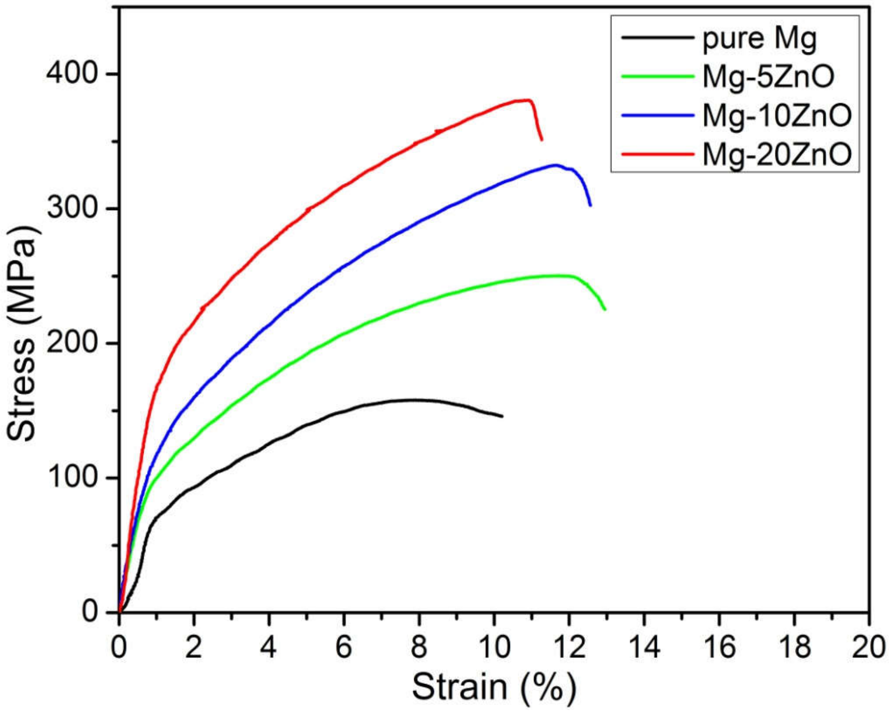

Figure 2.17. Stress-strain curve from compression tests of Mg-5 mass% ZnO, Mg-10 mass% ZnO and Mg-20 mass% ZnO composites sintered at 550 °C by SPS in 30 minutes

Table 2.1 showed statistic of mechanical properties of the composites, pure Mg and cortical bone. For application of implant materials, one important requirement should be taken into account is Young's modulus. Young's modulus of the applied materials should be equivalent to that of bone in order to avoid stress shielding effect which cause failure in implantation. As could be seen from table 2.1, Young's modulus of the fabricated composites are very similar to that of bone. So far, there have been no other metallic biomaterials have as close Young's modulus to that of bone as fabricated composites in this work.

Table 2.1. Mechanical properties of fabricated composites, pure Mg and cortical bone.

Materials	Young’s Modulus (GPa)	Yield strength (MPa)	Ultimate compression strength (MPa)	Elongation to failure (%)
Mg 30 minutes	6.1	71	156	10.2
Mg-5ZnO 10 minutes	10.2	89	238	12.8
Mg-5ZnO 30 minutes	12.4	96	250	12.9
Mg-10ZnO 10 minutes	15.2	120	283	11.9
Mg-10ZnO 30 minutes	16.5	126	332	12.5
Mg-20ZnO 10 minutes	24.8	205	359	7.7
Mg-20ZnO 30 minutes	23.3	180	380	11.2
Cortical bone	11-21	-	70-280	-

Figure 2.18 compares strength of as-produced composites in this work and other conventional Mg based biomaterials. As could be seen, as-fabricated composites exhibited much higher strength compared to other conventional applied Mg based biomaterials.

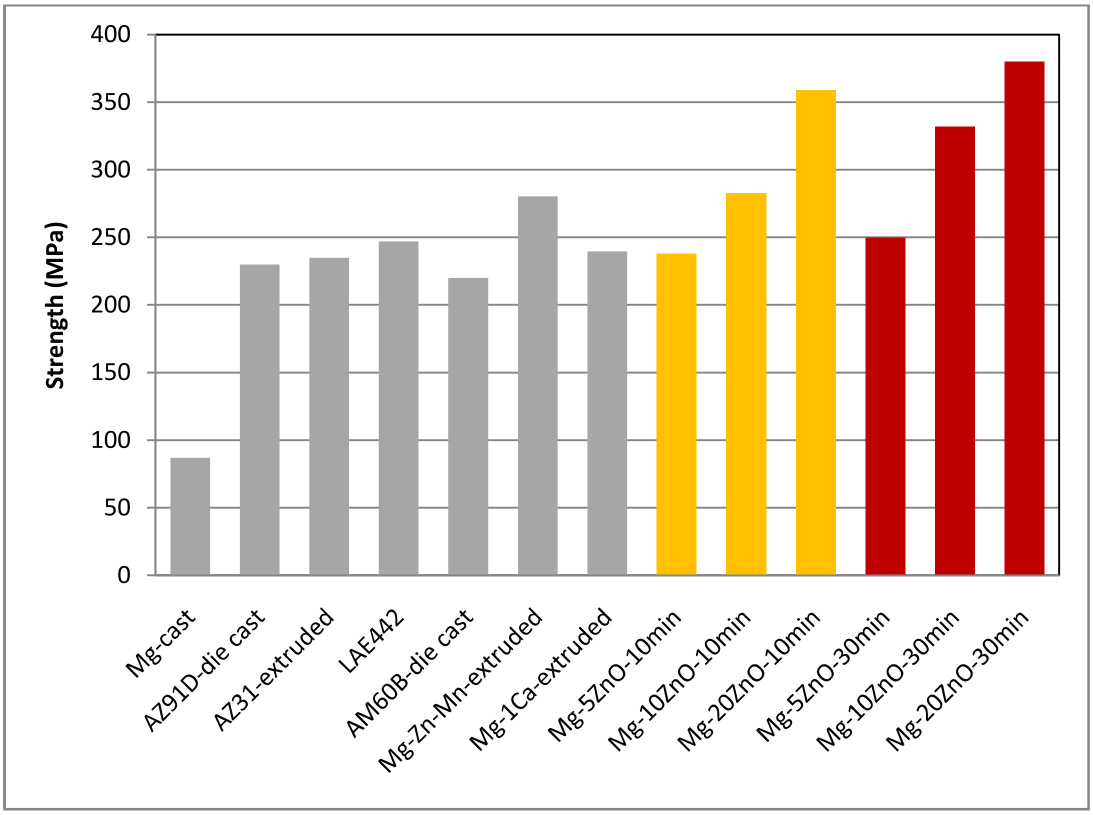

Figure 2.18. Comparison of strength of fabricated composites with other Mg based biomaterials.

2.4. Conclusion

Mg matrix *in situ* composites with some reaction products as reinforcements were successfully synthesized. There were two *in situ* reactions occurred during sintering process from room temperature to 550 ^{o}C to form Zn, MgO and Mg-Zn intermetallic compounds.

Sintering pressure is attributed as increasing reaction rate of *in situ* reaction (1) and become activator for *in situ* reaction (2).

Microstructure of the composites showed high sintering quality without noticeable aggregation of reaction products.

Sintered Mg-ZnO composites exhibited much higher mechanical properties compared to those of sintered pure Mg and other conventional Mg based biomaterials.

Sintered Mg-ZnO composites showed similar Young's modulus to that of cortical bone.

With these results, as-produced Mg-ZnO composites have very good mechnical properties for implant applications.

Reference

[1] C. Cup, Y. Shen, F. Meng, Review on Fabrication Methods of in situ Metal Matrix Composites, J. Mater. Sci. Technol. 16 (2000) 619–626.

[2] R.M. Aikin, The Mechanical Properties of In-Situ Composites, JOM. 49 (1997) 35–39.

[3] Q. Zhang, B.L. Xiao, W.G. Wang, Z.Y. Ma, Reactive mechanism and mechanical properties of in situ composites fabricated from an Al–TiO2 system by friction stir processing, Acta Mater. 60 (2012) 7090–7103.

[4] S. Hao, L. Cui, F. Guo, Y. Liu, X. Shi, D. Jiang, et al., Achieving large linear elasticity and high strength in bulk nanocompsite via synergistic effect, Sci. Rep. 5 (2015) 8892.

[5] L. Xiang, F. Wang, J. Zhu, X. Wang, Mechanical properties and microstructure of Al2O3/TiAl in situ composites doped with Cr2O3, Mater. Sci. Eng. A. 528 (2011) 3337–3341.

[6] H.B. Lee, H. Tezuka, E. Kobayashi, T. Sato, K. Do Woo, Fabrication and Mechanical Properties of Al-Based In Situ Nano-Composites Reinforced by Al2O3 and Intermetallic Compounds, Mater. Trans. 53 (2012) 428–434.

[7] C.S. Ramesh, S. Pramod, R. Keshavamurthy, A study on microstructure and mechanical properties of Al 6061–TiB2 in-situ composites, Mater. Sci. Eng. A. 528 (2011) 4125–4132.

[8] W. Daoush, a. Francis, Y. Lin, R. German, An exploratory investigation on the in-situ synthesis of SiC/AlN/Al composites by spark plasma sintering, J. Alloys Compd. 622 (2015) 458–462.

[9] V.M. Sreekumar, N. Hari Babu, D.G. Eskin, Z. Fan, Structure–property analysis of in-situ Al–MgAl2O4 metal matrix composites synthesized using ultrasonic cavitation, Mater. Sci. Eng. A. 628 (2015) 30–40.

[10] K. Xu, a. M. Russell, L.S. Chumbley, F.C. Laabs, A deformation processed Al-20%Sn In-Situ composite, Scr. Mater. 44 (2001) 935–940.

[11] C.F. Feng, L. Froyen, Formation of Al3Ti and Al2O3 from an Al–TiO2 system for preparing in-situ aluminium matrix composites, Compos. Part A Appl. Sci. Manuf. 31 (2000) 385–390.

[12] H. Zreiqat, C.R. Howlett, a. Zannettino, P. Evans, G. Schulze-Tanzil, C. Knabe, et al., Mechanisms of magnesium-stimulated adhesion of osteoblastic cells to commonly used orthopaedic implants, J. Biomed. Mater. Res. 62 (2002) 175–184.

[13] L. Li, J. Gao, Y. Wang, Evaluation of cyto-toxicity and corrosion behavior of alkali-heat-treated magnesium in simulated body fluid, Surf. Coatings Technol. 185 (2004) 92–98.

[14] J.W. Seong, W.J. Kim, Development of biodegradable Mg–Ca alloy sheets with enhanced strength and corrosion properties through the refinement and uniform dispersion of the Mg2Ca phase by high-ratio differential speed rolling, Acta Biomater. 11 (2015) 531–542.

[15] X. Gu, W. Zhou, Y. Zheng, L. Dong, Y. Xi, D. Chai, Microstructure, mechanical property, bio-corrosion and cytotoxicity evaluations of Mg/HA composites, Mater. Sci. Eng. C. 30 (2010) 827–832.

[16] Y.F. Zheng, X.N. Gu, Y.L. Xi, D.L. Chai, In vitro degradation and cytotoxicity of Mg/Ca composites produced by powder metallurgy, Acta Biomater. 6 (2010) 1783–1791.

[17] F. Witte, F. Feyerabend, P. Maier, J. Fischer, M. Störmer, C. Blawert, et al., Biodegradable magnesium-hydroxyapatite metal matrix composites, Biomaterials. 28 (2007) 2163–2174.

[18] Y. Huang, D. Liu, L. Anguilano, C. You, M. Chen, Fabrication and characterization of a biodegradable Mg–2Zn–0.5Ca/1β-TCP composite, Mater. Sci. Eng. C. 54 (2015) 120–132.

[19] A.K. Khanra, H.C. Jung, K.S. Hong, K.S. Shin, Comparative property study on extruded Mg-HAP and ZM61-HAP composites, Mater. Sci. Eng. A. 527 (2010) 6283–6288.

[20] S.H. Kwon, Y.K. Jun, S.H. Hong, H.E. Kim, Synthesis and dissolution behavior of ??-TCP and HA/β-TCP composite powders, J. Eur. Ceram. Soc. 23 (2003) 1039–1045.

[21] C.J. Deng, M.L. Wong, M.W. Ho, P. Yu, D.H.L. Ng, Formation of MgO and Mg-Zn intermetallics in an Mg-based composite by in situ reactions, Compos. Part A Appl. Sci. Manuf. 36 (2005) 551–557.

[22] T. Lei, W. Tang, S.H. Cai, F.F. Feng, N.F. Li, On the corrosion behaviour of newly developed biodegradable Mg-based metal matrix composites produced by in situ reaction, Corros. Sci. 54 (2012) 270–277.

[23] S. Cai, T. Lei, N. Li, F. Feng, Effects of Zn on microstructure, mechanical properties and corrosion behavior of Mg-Zn alloys, Mater. Sci. Eng. C. 32 (2012) 2570–2577.

[24] X. Gu, Y. Zheng, Y. Cheng, S. Zhong, T. Xi, In vitro corrosion and biocompatibility of binary magnesium alloys, Biomaterials. 30 (2009) 484–498.

[25] S. Zhang, X. Zhang, C. Zhao, J. Li, Y. Song, C. Xie, et al., Research on an Mg-Zn alloy as a degradable biomaterial, Acta Biomater. 6 (2010) 626–640.

[26] S. Zhang, J. Li, Y. Song, C. Zhao, X. Zhang, C. Xie, et al., In vitro degradation, hemolysis and MC3T3-E1 cell adhesion of biodegradable Mg-Zn alloy, Mater. Sci. Eng. C. 29 (2009) 1907–1912.

[27] P. Trumbo, A. a. Yates, S. Schlicker, M. Poos, Dietary reference intakes: Vitamin A, Vitamin K, Arsenic, Boron, Chromium, Copper, Iodine, Iron,

Manganese, Molybdenum, Nickel, Silicon, Vanadium and Zinc, J. Am. Diet. Assoc. 101 (2001) 294–301.

[28] H. Tapiero, K.D. Tew, Trace elements in human physiology and pathology: zinc and metallothioneins., Biomed. Pharmacother. 57 (2003) 399–411.

[29] M. Omori, Sintering, consolidation, reaction and crystal growth by the spark plasma system (SPS), Mater. Sci. Eng. A. 287 (2000) 183–188.

[30] T. Chartier, A. Badev, Handbook of Advanced Ceramics, Second Edi, Elsevier Inc., 2013.

[31] Astm, ASTM E384: Standard Test Method for Knoop and Vickers Hardness of Materials, ASTM Stand. (2012) 1–43.

[32] ASTM Standard E9-09, Standard Test Methods of Compression Testing of Metallic Materials at Room Temperature, Annu. B. ASTM Stand. 3.01 (2012) 92–100.

[33] T. Kokubo, H.M. Kim, M. Kawashita, Novel bioactive materials with different mechanical properties, Biomaterials. 24 (2003) 2161–2175.

[34] K. Tun, V. Tungala, Q. Nguyen, J. Chan, R. Kwok, J. Kuma, et al., Enhancing tensile and compressive strengths of magnesium using nanosize (Al2O3 + Cu) hybrid reinforcements, J. Compos. Mater. 46 (2012) 1879–1887.

[35] K.S. Tun, M. Gupta, Compressive deformation behavior of Mg and Mg/(Y2O3+Ni) nanocomposites, Mater. Sci. Eng. A. 527 (2010) 5550–5556.

[36] K.S. Tun, P. Jayaramanavar, Q.B. Nguyen, J. Chan, R. Kwok, M. Gupta, Investigation into tensile and compressive responses of Mg–ZnO composites, Mater. Sci. Eng. 28 (2011) 582-588.

CHAPTER 3

IN VITRO CORROSION PROPERTIES OF Mg MATRIX *IN SITU* COMPOSITES FABRICATED BY SPARK PLASMA SINTERING

3.1. Introduction

In the past decades, traditional metallic biomaterials including pure Ti and its alloys, CoCr alloys, stainless steels have been widely applied into bone replacement, bone fixation devices in order to repair bone fractures or support in healing process. However, these types of traditional metallic biomaterials required secondary surgery in order to remove the implants after healing [1-3]. Recently, Magnesium and its alloys emerged as promising candidates for biodegradable implant applications which do not require additional surgery for removal of implant after healing. Mg and its alloys are not only biocompatible but also contribute to the stimulation of bone growth and the healing process [4,5]. In addition, Mg based materials have similar mechanical properties and Young's modulus compared with those of natural bone, avoiding stress shielding effect [6,7]. However, the drawback of Mg and its alloys is fast degradation rate *in vivo*, affecting mechanical integrity of the healing process [8]. Thus, it is essential to improve both initial mechanical properties and corrosion resistance of Mg based materials. So far, there have been many research works on development of mechanical properties and corrosion resistance of conventional Mg matrix composites for biodegradable implant applications. However, as-developed composites either exhibited poor mechanical properties [9-11] or were not fully biodegradable due to very low solubility of reinforcements *in vivo* [12-15]. In such a situation, Mg matrix *in situ* composites became potential candidates.

Deng et al. [16] and Lei et al. [17] successfully fabricated Mg matrix *in situ* composites from mixed Mg-ZnO powder by conventional sintering method. However, the as fabricated composites exhibited limitation in the improvement of mechanical properties and corrosion resistance due to the insufficient sintering degree. In previous chapter, spark plasma sintering (SPS) technique was employed to fabricated Mg matrix *in situ* composites with excellent mechanical properties from mixed Mg-ZnO powder.The work indicated that *in situ* reaction products including MgO, Zn, and intermetallic compounds significantly reinforced mechanical performance of the as fabricated composites. Previous research has shown that Zn is an effective additive that improves the mechanical properties as well as the corrosion resistance of Mg based biomaterials [19-22]. In addition, Zn is also biocompatible and biodegradable with a daily moderate amount of allowance [23,24]. In this study, with the purpose of using Zn and its compounds as reinforcements in order to improve corrosion resistance, Mg matrix *in situ* composites were fabricated from homogeneously mixed Mg-ZnO powder via the spark plasma sintering (SPS) technique.

The SPS is a relatively new sintering method and has received increasing attention as a high-speed powder consolidation technology. During the SPS process, spark plasma is generated by direct pulse current and is used simultaneously with a uniaxial pressure on powders. With rapid heating on the surface of the powders due to the direct pulse current, the metal powders with different melting temperatures can be synthesized easily. The SPS working temperatures are lower than that of conventional sintering, and its process time is approximately within a range of 10 min. These advantages of the SPS make it capable to prepare Mg matrix composites, which are difficult to fully sinter using conventional sintering methods [25,26].

In this study, SPS was employed for fabricating Mg matrix *in situ* composites from mixed Mg-ZnO powders. The corrosion property of fabricated composites was investigated by various corrosion tests.

3.2. Experimental procedure

3.2.1. Sample preparation

Mg powders with a purity of 99.5% and particle size of 180 μm and ZnO powders with a purity of 99.9% and particle size of 1 μm supplied by Kojundo Chemical Laboratory were used for sample preparation. Mg/ZnO powders with three different weight fractions (0, 10, 20 wt-%) were mixed homogeneously with zirconia balls (2.5 of ball to powder weight ratio) in an argon atmosphere using a planetary micro ball mill (Pulverisette 7) with rotation speed of 500 rpm for 12 h. No process control agent was used. The mixed powders were set inside the Tungsten-Carbide die of 120 mm in height and 15 mm in an inner diameter for the spark plasma sintering using a 511S, Syntex SPS system.

Five kinds of samples naming A, B-1, B-2, C-1, and C-2 were fabricated with different ZnO weight fractions and sintering conditions. Sample A, B-1, and C-1 were directly sintered by SPS while sample B-2 and C-2 were sintering in vacuum furnace before sintering by SPS. The details of fabrication process are shown in Table 3.1.

All the sintering processes were performed in a high vacuum chamber. After sintering processes, the samples were cooled down to room temperature inside the vacuum chamber.

Table 3.1. Composition and sintering conditions of five kinds of samples.

Sample name	**Composition**	**Sintering in vacuum furnace** Time/Temperature/Pressure	**Sintering by SPS** Time/Temperature/Pressure
A	Mg-0 wt-% ZnO	-	10 min/550°C/50 MPa
B-1	Mg-10 wt-% ZnO	-	10 min/550°C/50 MPa
B-2	Mg-10 wt-% ZnO	2.5 h/550°C/0MPa	10 min/550°C/50 MPa
C-1	Mg-20 wt-% ZnO	-	10 min/550°C/50 MPa
C-2	Mg-20 wt-% ZnO	2.5 h/550°C/0MPa	10 min/550°C/50 MPa

3.2.2. Composition and microstructure analysis

The sintered composites were machined into disk shape with the size of Φ15 × 2 (mm). The machined samples were ground using SiC papers up to 4000 grit, successively polished with ¼-µm diamond paste, ultrasonically cleaned with ethanol and then dried for sample characterisation. X-ray diffractometry (XRD) was conducted using a RINT2100 RIGAKU diffractometer. Microstructural observation was performed using a backscattering electron microscope (BSEM) (Miniscope 1000, Hitachi).

3.2.3. Immersion Tests

Disk shape specimens with dimensions of Φ14 x 2 (mm) were immersed in Hanks' solution at 37°C for 14 days in air. The specimens were placed on a clip to expose the bottom surface to the solution. The composition of Hanks' solution is described in Table 2. The ratio of surface area to solution volume was 1 cm^2 : 50 ml. The immersion test was conducted in triplicate for each sample condition.

Amount of Mg^{2+} ions dissolved in the sampled medium were quantified by a colorimetric method using Xylidyl blue-I [27,28]. In addition, hydrogen gas generated was collected by a burette with a funnel which was placed over the immersed sample. XRD, SEM, EDX, and Fourier-transform infrared spectroscopy (FTIR) were conducted for the samples after the immersion test for 14 days.

Table 3.2. Composition of Hanks' solution using for immersion tests.

Reagent	**NaCl**	**KCl**	**$Na_2HPO_4.H_2O$**	**KH_2PO_4**	**$MgSO_4.7H_2O$**	**$NaHCO_3$**	**$CaCl_2$**
Concentration (g/L)	8.00	0.40	0.06	0.06	0.20	0.35	0.14

3.2.4. Polarization and Impedance Tests

In order to evaluate the dynamic corrosion resistance and corrosion behaviour of the as fabricated composites, polarization and impedance tests were carried out. Polarization tests were carried out in Hanks' solution. The surface was coated with epoxy resin to expose the measurement area of 1 cm^2 to to Hanks' solution at 37°C. The open circuit potential was mesured for 1500 s. Subsequently, potentiodynamic polarisation curves were mesured in the potential range from -0.1 V vs. open circuit potential (E_{ocp}) at a scan rate of 1 mV/s. Electrochemical impedance spectroscopy (EIS) measurements were performed at E_{ocp} with the scan frequency ranged from 100 kHz to 0.01 Hz, and with the perturbation amplitude of 5 mV. The reference and counter electrodes were saturated Ag/AgCl and Pt electrodes, respectively.

3.3. Results and Discussion

3.3.1. Composition and microstructure of composites

XRD patterns of the samples A, B-1, B-2, C-1, and C-2 in Figure 1-(a), (b), and (c) show that there are peaks of MgO, Zn, and Mg-Zn intermetallic compounds for all composite samples. In addition, there are peaks of ZnO detected for samples C-1 and C-2.

In previous chapter, it was demonstrated that the following *in situ* reactions occurred during sintering mixed Mg-ZnO powders from room temperature to 550°C.

$$Mg_{(s)} + ZnO_{(s)} \xrightarrow{450-500\ ^{\circ}C} MgO_{(s)} + Zn_{(l)} \quad (1)$$

$$Mg_{(s)} + Zn_{(l)} \xrightarrow{500-550\ ^{\circ}C} Mg\text{-}Zn_{(l)} \quad (2)$$

$$Mg\text{-}Zn_{(l)} \xrightarrow{\text{Cooling}} Mg_xZn_y \quad (3)$$

where the subscripts (s) and (l) refer to solid state and liquid state, respectively, and Mg_xZn_y includes MgZn, Mg_2Zn_3 and Mg_7Zn_3 intermetallic compounds.

The peak of ZnO of sample C-1 is higher than that of sample C-2, indicating that the amount of remained ZnO in sample C-1 is larger than that in sample C-2. This is reasonable because sintering time of sample C-1 was much shorter than that of sample C-2. Consequently, the amount of ZnO in sample C-2 involved in reaction (1) was much higher than that in sample C-1 resulting in lower amount of remained ZnO in sample C-2 compared with that in sample C-1. Similarly, the intensity of MgO peak of samples C-1 and C-2 is higher than that of samples B-1 and B-2. Therefore, the amount of newly produced MgO in samples C-1 and C-2 is much higher than that in samples B-1 and B-2 because the amount of initial ZnO in sample C-1 and C-2 is the double of that in samples B-1 and B-2, respectively.

Figure 3.2 shows SEM images of four samples B-1, B-2, C-1, and C-2. Focus on second phase region, it can be seen that there are remained ZnO white particles randomly distributed in reaction products. The amount of remained ZnO increased in the following order: C-2<C-1<B-2<B-1. This is reasonable because of following reason. Firstly, the initial amount of ZnO in samples B-1 and B-2 is 10%, and the initial amount of ZnO in samples C-1 and C-2 is 20%. Sintering time of samples B-1 and C-1 is 10 min, while sintering time of samples B-2 and C-2 is 2.5 h. Consequently, ZnO involved in reaction (1) of sample B-2 is higher than that of sample B-1. Similarly, ZnO involved in reaction (1) of sample C-2 is higher than that of sample C-1. In addition, from SEM images, it can be seen that ZnO displayed as while particles distributed in the second phase region. The density of while particles

in second phase increased in the following order: C-2<C-1<B-2<B-1. Combining all above reasons and XRD result, It is able to conclude that the amount of remained ZnO increased in the following order: C-2<C-1<B-2<B-1. This reveals that sintering in vacuum furnace significantly decreased the remained ZnO in samples C-2 and B-2 compared to C-1 and B-1, respectively.

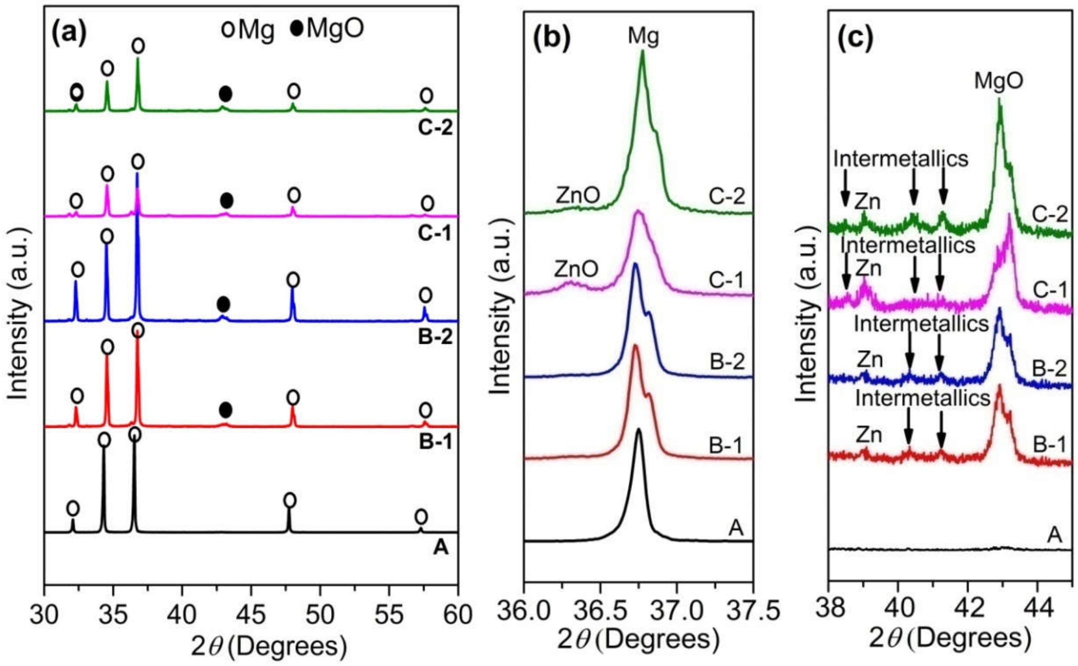

Figure 3. 1: XRD patterns of as fabricated samples, (a): full scan range of 2θ from 30 to 60 degrees, (b): magnification of 2θ from 36 to 37.5 degrees, and (c): magnification of 2θ from 38 to 45 degrees.

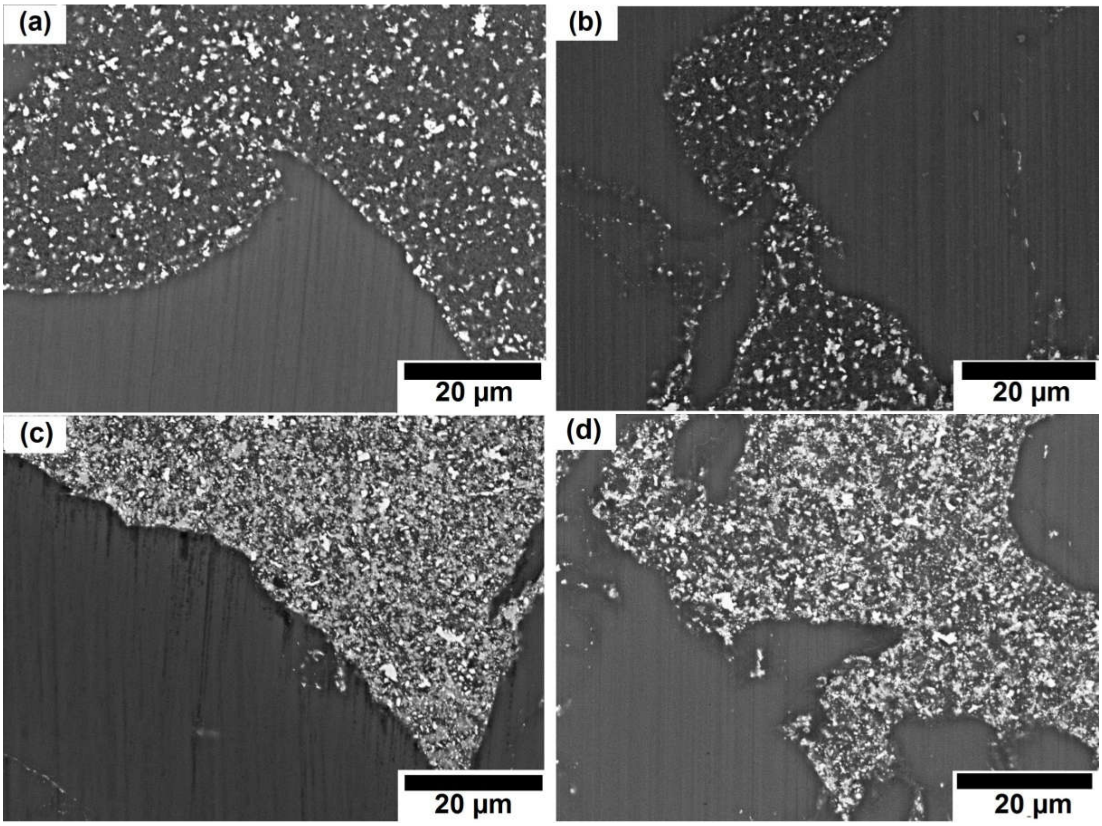

Figure 3. 2: SEM images of (a) sample B-1, (b) sample B-2, (c) sample C-1, and (d) sample C-2.

3.3.2. Corrosion behavior under static immersion

a) Mg^{2+} ion release behavior

Figure 3.3 shows amount of Mg^{2+} ion released per cm^2 in Hanks' solution as a function of immersion period of fabricated samples. It could be seen that all samples show the highest Mg^{2+} ion release rate in the first 2 days. After 2 days, the Mg^{2+} ion release rate decreased. This suggested that, corrosion occurred most severely during the first 2 days. After 2 days, corrosion products formed and deposited on the surface of samples. This corrosion product layer acted as a protective layer which inhibited severe corrosion, leading to lower Mg^{2+} ion release rates in the subsequent days. In another aspect, Mg-10 wt-% ZnO composites (samples B-1 and B-2) exhibited the lowest corrosion rates, while pure Mg sample (sample A) showed the highest corrosion rate. Although Mg-20 wt-% ZnO composites (samples C-1 and C-2) showed a slight improvement in corrosion resistance compared with pure Mg sample, they exhibited much higher corrosion rate than that of Mg-10 wt-% ZnO composites.

As for the effect of sintering time, with the same initial composition, the composites sintered in vacuum furnace for 2.5 h and by SPS for 10 min showed lower corrosion rates than the composites sintered only by SPS for 10 min. The improvement of corrosion resistance of the composites can be understood by the positive effect of produced Zn and Mg-Zn intermetallic compounds. As demonstrated in previous works [19-22], Zn is able to significantly improve the corrosion resistance of Mg matrix. On the other hand, the above results suggested that remained ZnO and newly produced MgO had negative effect on the corrosion resistance of these composites. The composite with the higher amount of remained ZnO and newly produced MgO, the higher corrosion rate it exhibited.

b) H_2 gas evolution behavior

Figure 3.4 reveals hydrogen-evolution behavior of fabricated samples during immersion in Hanks' solution. The hydrogen-evolution behavior exhibited similar trend to Mg^{2+} ion release behavior. Specifically, sample A showed strongest gas evolution over the limitation of the gas container after 1 day. Samples C-1 and C-2 exhibited second and third gas evolution rates and over the limitation of gas container after 6 and 8 days, respectively. Whereas samples B-1 and B-2 featured the lowest gas evolution rates. This result is in agreement with the result of Mg^{2+} ion release measurement shown in Figure 3.3 that samples B-1 and B-2 showed lowest corrosion rates, while sample A showed highest corrosion rate.

c) Surface morphology and composition of immersed sample surface.

Figure 3.5 shows surface morphology of the samples before and after immersion tests. The images of samples A and C-1 were taken in Hanks' solution. As could be seen that, samples A (Figure 3.5(f)) and C-1 (Figure 3.5(i)) were fractured during the immersion period, indicating the lowest corrosion resistance. While sample B-2 (Figure 3.5(h)) showed the least corrosion with partially corroded area on the surface. Surface appearance of sample C-2 (Figure 3.5(k)) showed filiform corrosion on the most surface area with corrosion products deposited. On the surface of sample B-1 (Figure 3.5(g)), there were a lot of pits on the surface area instead of filiform corrosion. On the sample B-2 (Figure 3.5(h)), there was a part of surface area covered by filiform corrosion and randomly pits appeared. It could be seen that the corrosion area ratios are consistent to the amounts of released Mg^{2+} ion showed in Figure 3.3.

Figure 3.6 shows SEM images of surface of immersed samples B-1, B-2, and C-2. The SEM images were taken at non-corroded areas of samples. All three surfaces showed deposited corrosion products. Sample B-1 and B-2 showed similar corrosion product structure; however, the corrosion product layer on surface of sample B-1 is thicker than that on surface of sample B-2. Corrosion product deposited on surface of sample C-2 showed porous structure. The structure of corrosion product layers on surface of samples B-1 and B-2 indicated that they played an important role as protective layers avoiding severe corrosion. On the other hand, porous structure of corrosion product on surface of sample C-2 indicated weak protective layer. It was easily diffused or broken by solution resulting in severe corrosion.

Table 3.3 shows the result of EDX analysis of corrosion products on the surface of samples B-1, B-2, and C-2. The analyzed areas were mark by yellow circles on Figure6. As for samples B-1 and B-2, the ratio of atomic percents of Ca : P : O suggesting formation of calcium phosphate on the surfaces of these samples.

The atomic percents of Mg and Zn on surface of sample B-1 were lower than those on surface of sample B-2 confirming that corrosion product layer on sample B-1 was thicker than that on sample B-2. As discussed by previous works [29,30], the formation of calcium phosphate on surface of sample B-1 and B-2 not only increases the corrosion resistance of Mg based materials but also enhances the osseointegration.

On the other hand, the EDX analysis result on sample C-2 suggested the formation of $Mg(OH)_2$ on the surface of this sample because the ratio of atomic percent of Mg : O ≈ 1 : 2.

Figure 3.10 shows XRD patterns of sample B-1, B-2, and C-2 samples. The results confirmed that $Mg(OH)_2$ formed only on the surface of sample C-2 since the peak of $Mg(OH)_2$ was detected only on the pattern of this sample. The formation of $Mg(OH)_2$ on C-2 sample might be due to the high amount of MgO existing in this sample before immersion. It should be noted that this sample contained highest amount of MgO compared with that in B-1 and B-2 sample.

It was confirmed in previous work [12] that the corrosion products of the Mg based materials in the simulated body fluid were composed of magnesium hydroxide and calcium phosphate. Therefore, the formation of $Mg(OH)_2$ on the surface of sample C-2 and calcium phosphate compounds on the surface of sample B-1 and B-2 as the protective layers are reasonable in this research. However, calcium phosphate is attributed to strongly increase the corrosion resistance of B-1 and B-2 sample, while $Mg(OH)_2$ contributed to slight improvement in corrosion resistance of C-2 sample.

Figure 3.11 shows FTIR spectra of immersed samples B-1, B-2, and C-2. It could be seen that the presence of OH^- peak only for sample C-2 confirming that $Mg(OH)_2$ formed only on surface of sample C-2. The presence of PO_4^{3-} and CO_3^{2-} peaks for all three samples suggested that calcium phosphate and carbonates formed on the surface of three samples. However, the amount of calcium phosphate formed on surface of sample C-2 and amount of carbonates formed on the surface of three samples are too low to be detected by EDX analysis.

From EDX analysis, XRD patterns, and FTIR spectra of immersed samples B-1, B-2, and C-2, it can be concluded that $Mg(OH)_2$ is main corrosion product deposited on the surface of sample C-2, while calcium phosphate formed as main corrosion product on the surface of samples B-1 and B-2.

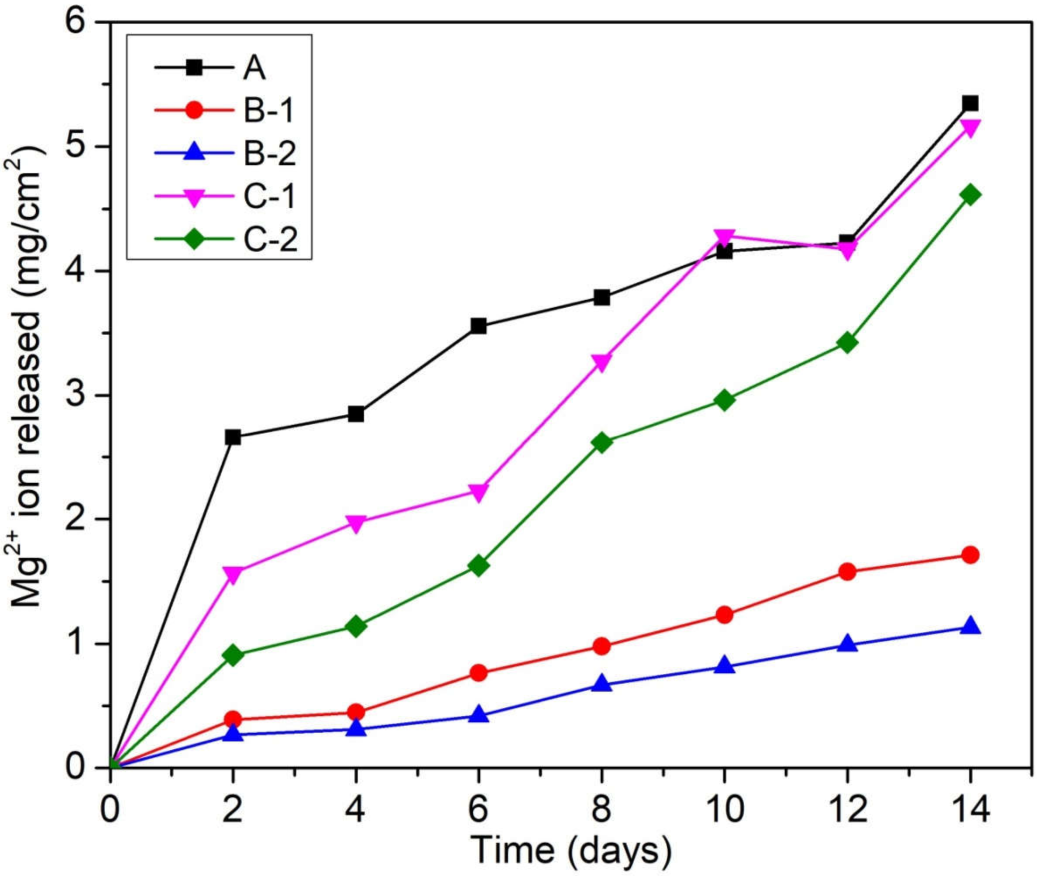

Figure 3.3. Mg^{2+} ion release in the Hanks' solution during immersion test.

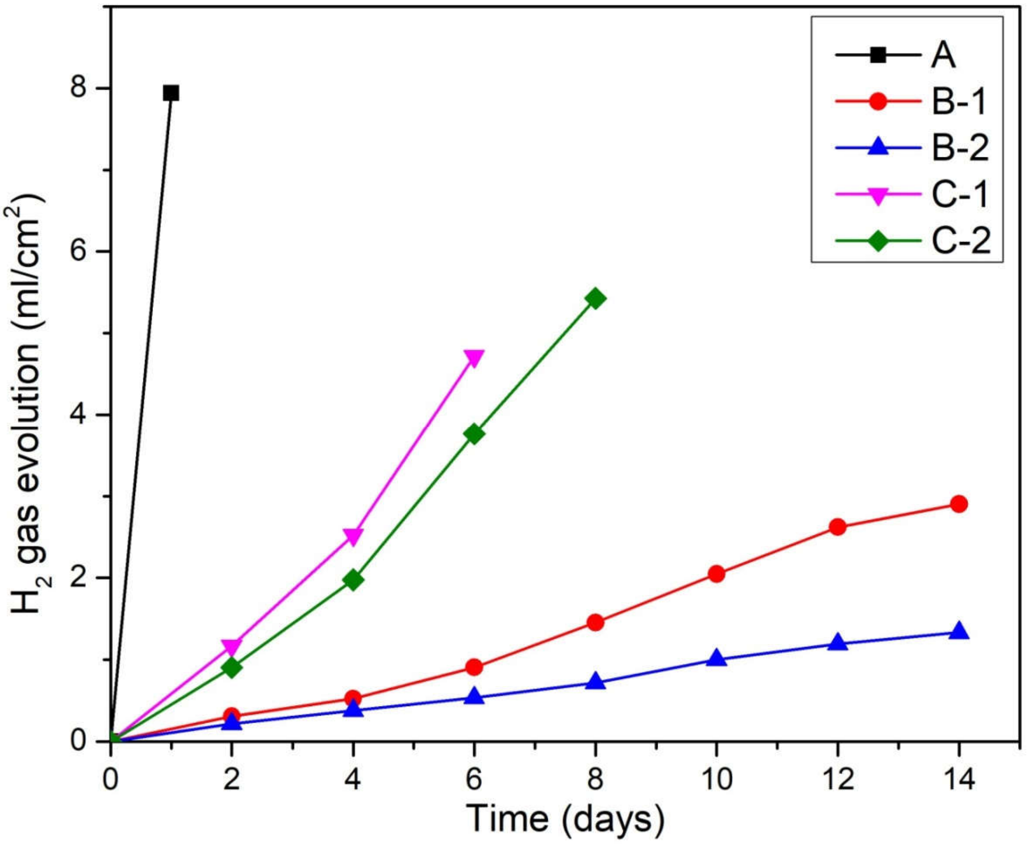

Figure 3. 4. Hydrogen gas evolution during immersion test.

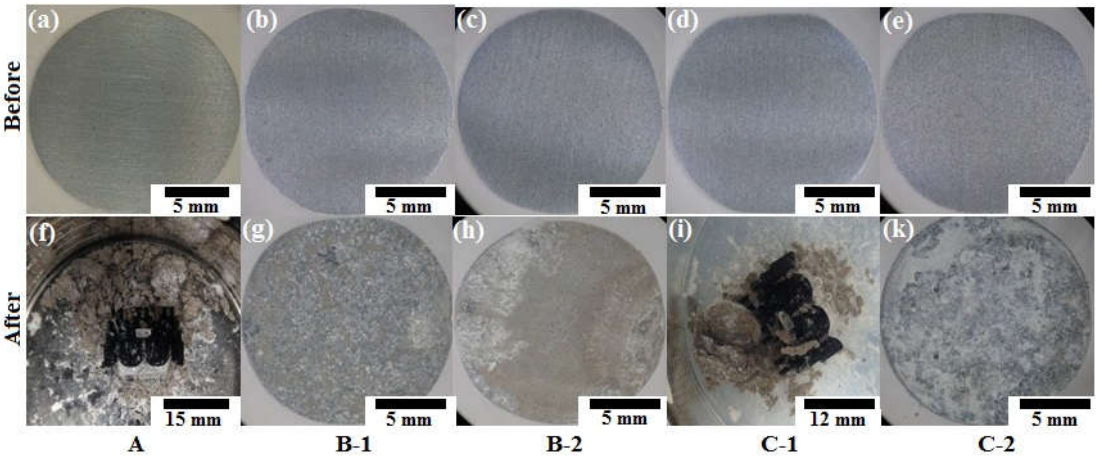

Figure 3. 5: Surface morphology of samples before and after immersion test.

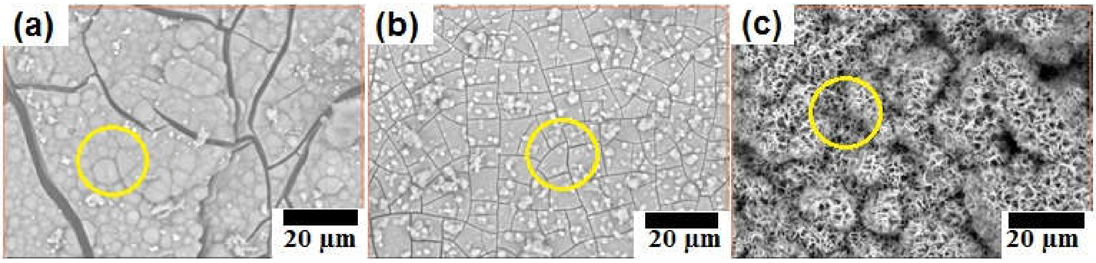

Figure 3. 6: SEM images of immersed samples: (a) B-1, (b) B-2, and (c) C-2.

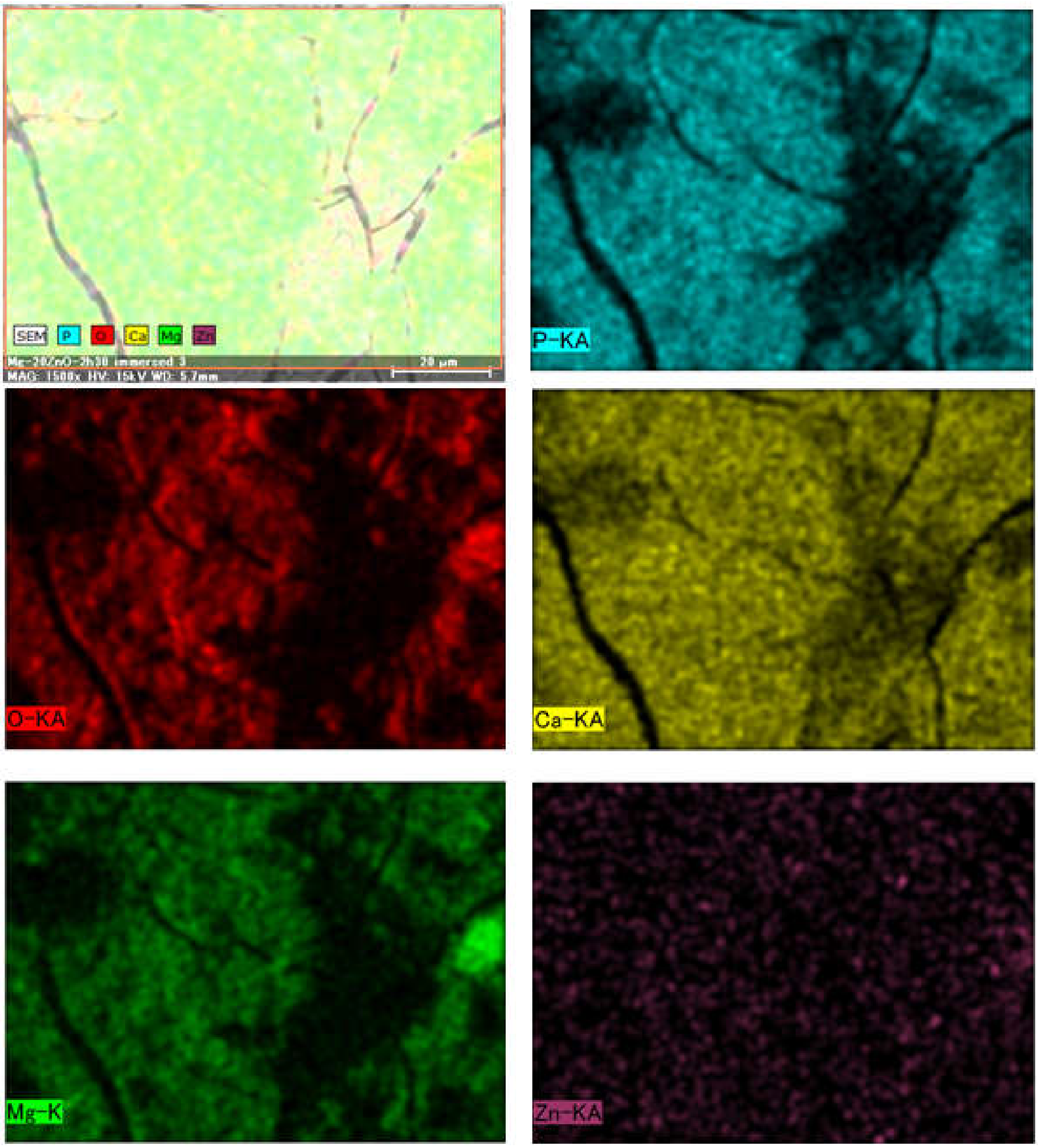

Figure 3.7. SEM images of elemental mapping images of immersed sample B-1.

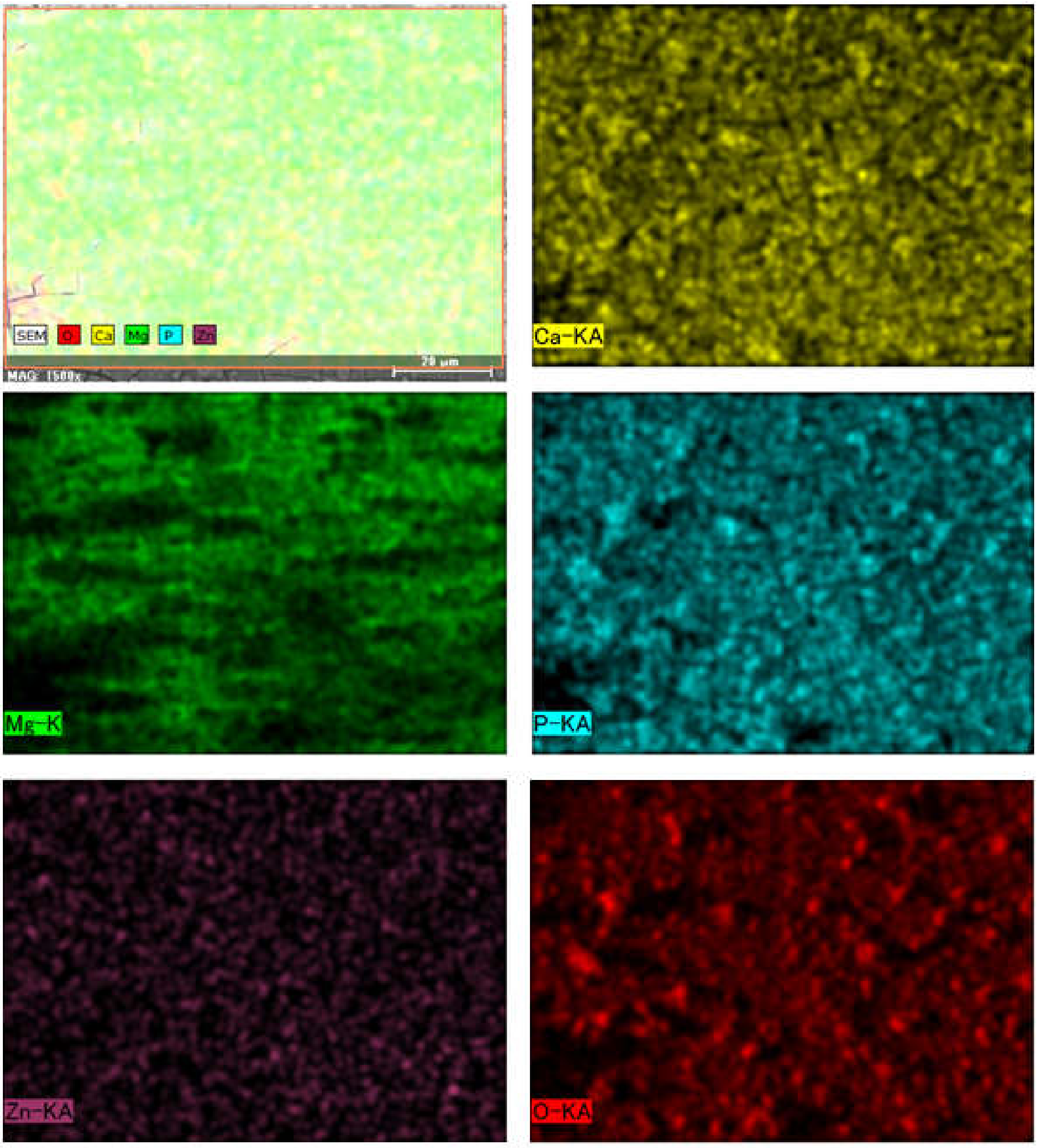

Figure 3.8. SEM images of elemental mapping images of immersed sample B-2.

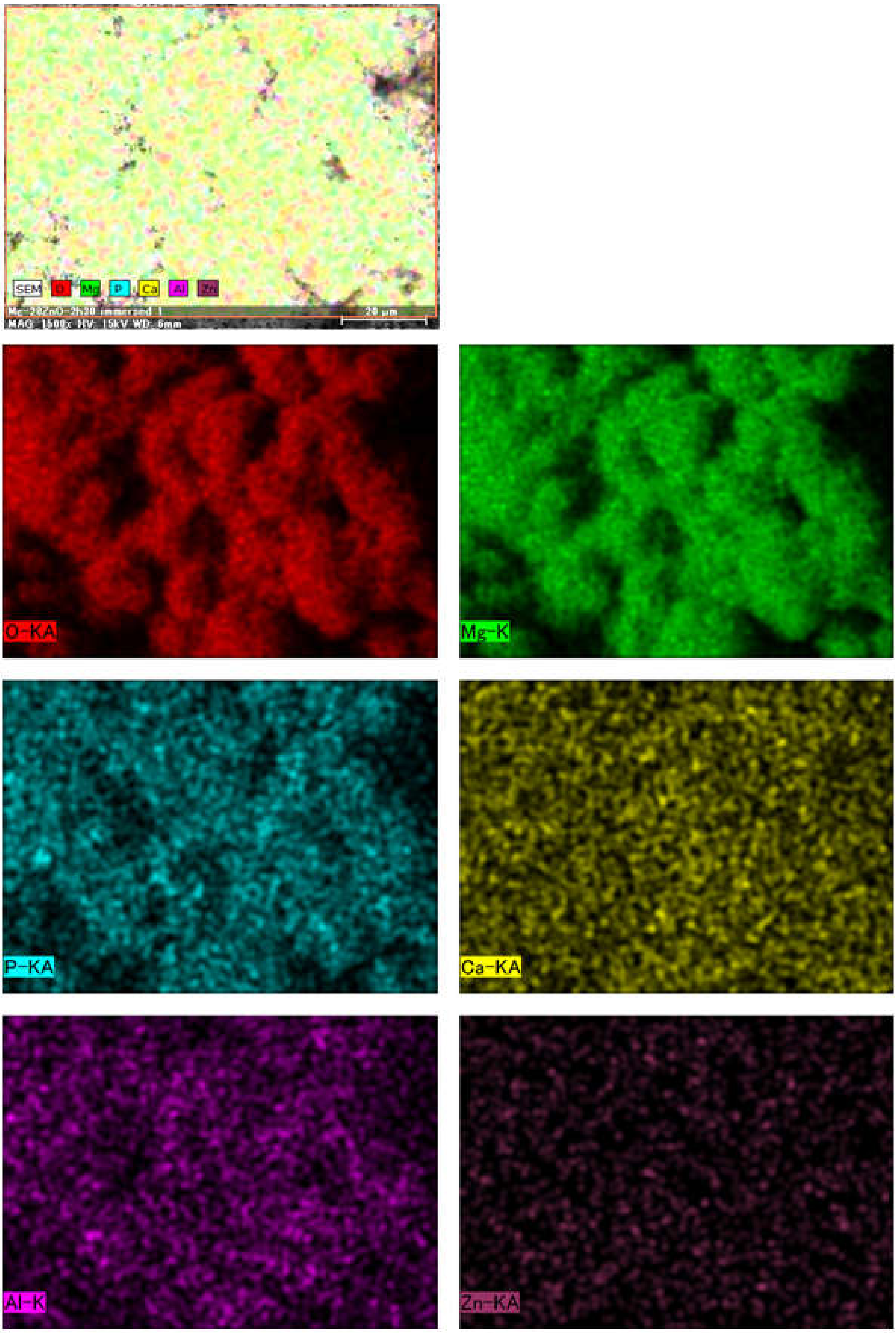

Figure 3. 9. SEM images of elemental mapping images of immersed sample C-2.

Table 3. 3: EDX analysis result on the surfaces of immersed samples.

Element	Sample B-1	Sample B-2	Sample C-2
Oxygen (at.%)	70	62	68
Calcium (at.%)	14	15	0
Phosphorus (at.%)	10	12	1
Magnesium (at.%)	6	11	31

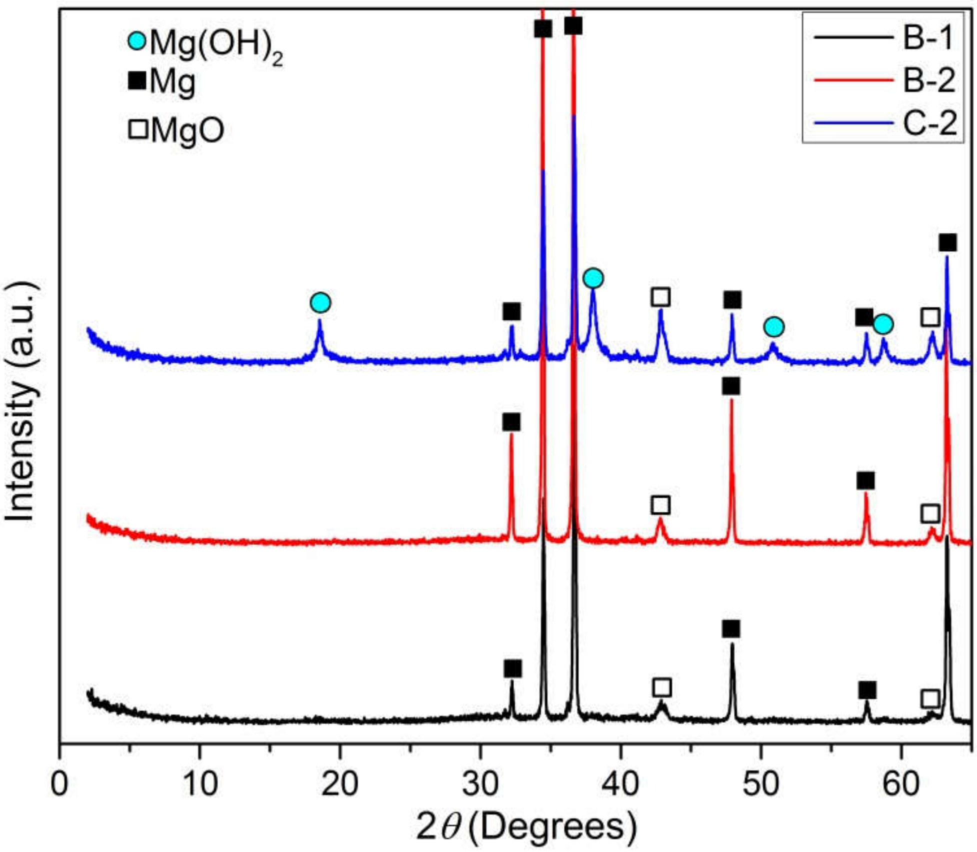

Figure 3. 10. XRD patterns of immersed samples B-1, B-2, and C-2.

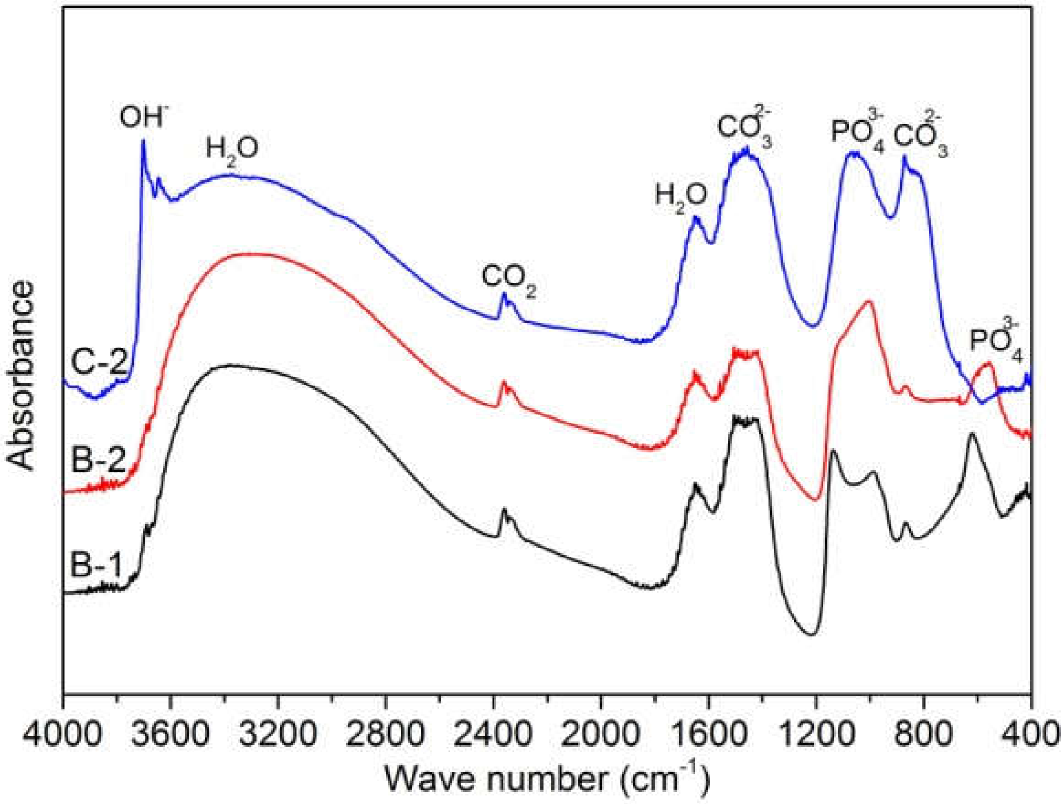

Figure 3. 11. FTIR spectra of immersed samples B-1, B-2, and C-2.

3.3.3. Polarization and Impedance behavior

Figures 3.12 and Figure 3.13 show the polarization curves and Bode plots of all samples in Hanks' solution, respectively. Generally, the dissolution rate of Mg^{2+} ions corresponds the anodic current density, while the reduction rate of water is hydrogen evolution reaction corresponds to the cathodic current density [31].

Anodic reaction: $Mg \rightarrow Mg^{2+} + 2e^-$

Cathodic reaction: $2H_2O + 2e^- \rightarrow H_2 + 2OH^-$

In this work, corrosion current density (I_{corr}) was obtained by Tafel extrapolation method since cathodic polarization curves showed a linear region. The corrosion potential (E_{corr}) and corrosion current density (I_{corr}) of the all samples are listed in Table 3.4. As shown, the Tafel curve for sample A exhibits the most negative corrosion potential at -1.63 V (vs. SCE) and highest corrosion current density at 2.7×10^{-5} Acm^{-2} indicating highest corrosion rate. Whereas, Tafel curves for sample B-2 and B-1 exhibits the most positive corrosion potentials at -1.47 V (vs. SCE) and -1.50 V (vs. SCE), and lowest corrosion current densities at 2.2×10^{-6} Acm^{-2} and 3.0×10^{-6} Acm^{-2}, respectively, indicating the lowest corrosion rates. This result is consistent with immersion test result.

The difference in impedance between 10^5 Hz and 10^{-2} Hz corresponds to the polarization resistance (R_p). The initial increase of R_p from 0 h to 0.5 h indicates the formation of a deposited corrosion product layer which showed corrosion protection property. The impedance result indicates that the corrosion product layer was formed in the pre-immersion of polarization test. The magnitude of cathodic current density of all samples except C-1 was similar, which is attributed to the formation of the corrosion product layer.

The impedance spectra showed that the polarization resistance of B-1 increased from 0 h to 2 h, decreased at 4 h and recovered at 6 h. The impedance spectrum at 4 h showed a lot of fluctuations and the phase shift became below zero. These results indicate that the local corrosion occurred around 4 h and the corrosion pit was recovered afterwards. B-2 showed the larger increase of R_p than B-1, and Rp at 6 h of B-2 was higher than that of B-1 although the R_p showed a decrease at 2 h and 4 h.

The higher R_p of B-2 than that of B-1 is consistent with the smaller Mg^{2+} ion release from B-2 than that from B-1 in the static immersion test.

The R_p of C-1 and C-2 increased from 0 h to 0.5, but the impedance decreased and the phase shift showed negative value in low frequency region. This result indicates that the corrosion product layer formed on C-1 and C-2 had defects from the beginning. The low R_p value is consistent with the large Mg^{2+} ion release from C-1 and C-2. The defects may be due to the large area ratio of the reaction product region on the surface. The corrosion product layer might not be able to cover the reaction product region.

It should be noted about the significant noise at some frequencies of the impedance test results. The source of this noise might be from effect of electricity to the measurement devices at some frequencies. This is because during the measurement, the filter to eliminate the noise caused by electricity was not used. However, the result of impedance tests still reveals precisely the measured property and is in consistance with immersion tests and polarization tests.

Table 3. 4. Corrosion potential (E_{corr}) and corrosion current density (I_{corr}) of the as fabricated samples.

Sample	**E_{corr} (V vs. SCE)**	**I_{corr} (A.cm^{-2})**
A	-1.63	$2.7x10^{-5}$
B-1	-1.50	$3.0x10^{-6}$
B-2	-1.47	$2.2x10^{-6}$
C-1	-1.59	$3.0x10^{-5}$
C-2	-1.57	$8.0x10^{-6}$

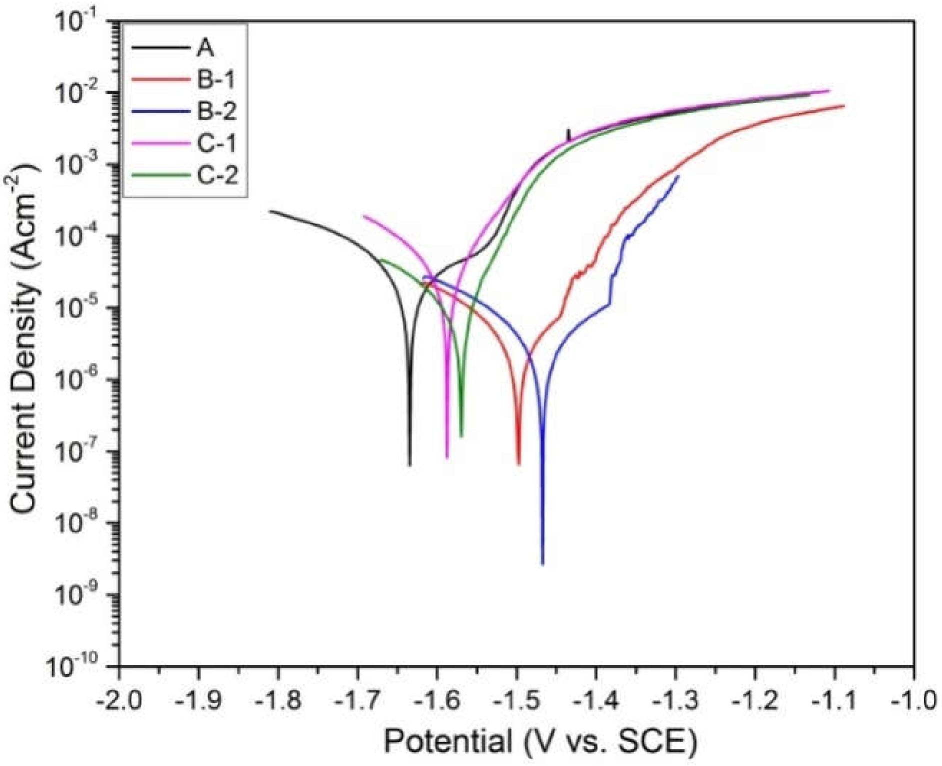

Figure 3. 12. Potentiodynamic polarisation curves of as fabricated samples in Hanks' solution.

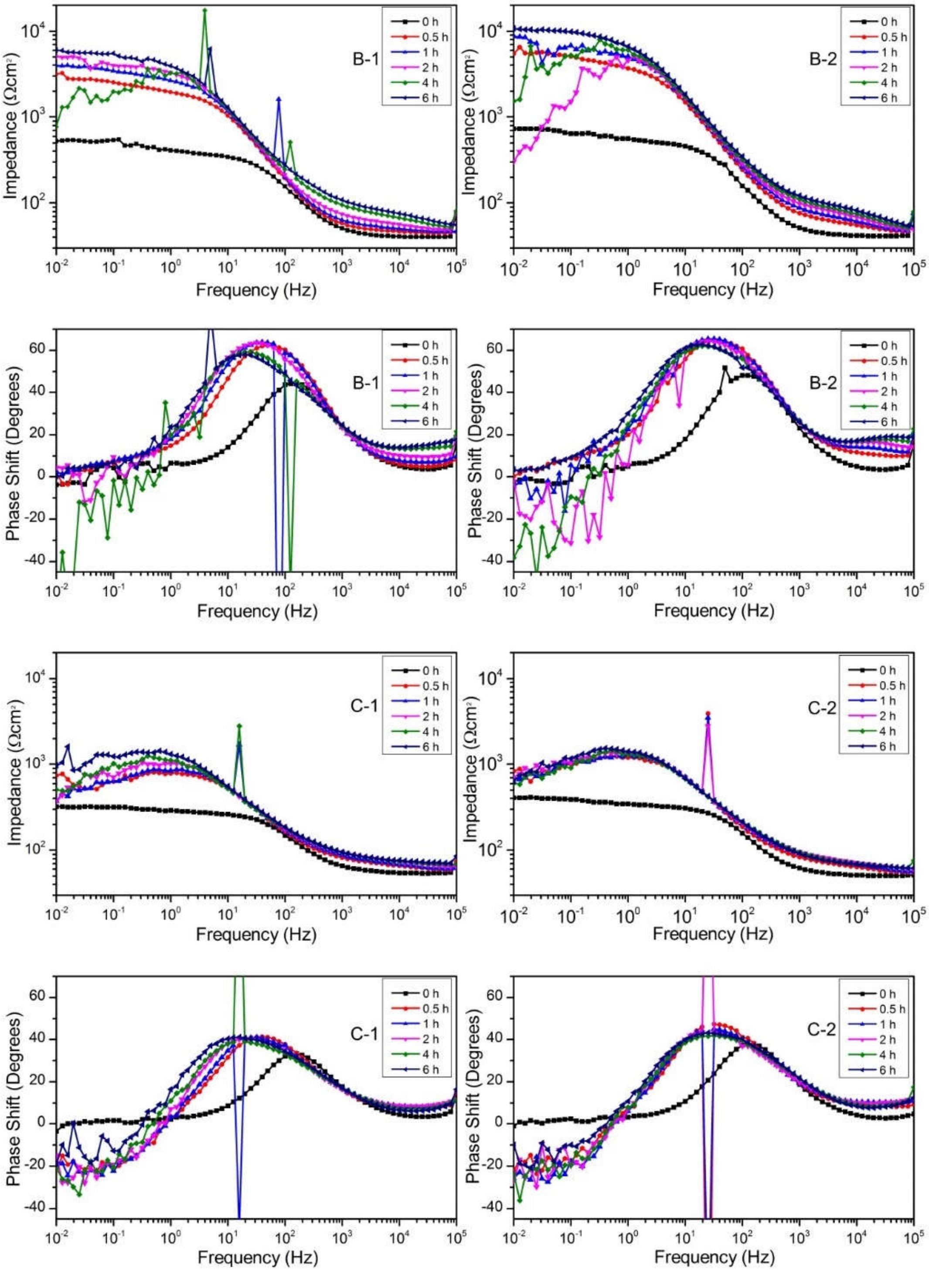

Figure 3. 13. Bode plots of sample B-1, B-2, C-1, and C-2 immersed in Hank's solution.

3.4. Conclusion

Mg-ZnO matrix *in situ* composites were synthesized and their corrosion property was investigated. Findings of the research are summarized as following:

(1) There were several *in situ* reactions occurred during sintering process from room temperature to 550 ^{o}C to form Zn, MgO and Mg-Zn intermetallic compounds.

(2) Newly formed Zn and Mg-Zn intermetallic compounds have positive effect while the remained ZnO has negative effect on the corrosion resistance of as fabricated composites.

(3) Mg-20 wt-% ZnO composites promoted the formation of $Mg(OH)_2$ on the surface of sample during immersion. This $Mg(OH)_2$ film plays as weak protective layer resulting in slight improvement of corrosion resistance.

(4) Mg-10 wt-%ZnO composites promoted the formation of calcium phosphate on the surface of samples. The calcium phosphate layer is possible to not only significantly increase the corrosion resistance of the composites but also is beneficial for osseointegration.

(5) The as produced composites, especially, Mg-10 wt-%ZnO composites have good corrosion properties for temporary implant applications

Reference

[1] Basu, B.; Katti, D.S.; Kumar A. Advanced Biomaterials: Fundamentals, Processing, and Applications, John Wiley &Sons: 2010.

[2] Niinomi, M. Recent metallic materials for biomedical applications.*Metall. Mater. Trans. A***2002**, *33*, 477–486.

[3] Yu, K.; Chen, L.; Zhao, J.; Li, S.; Dai, Y.; Huang, Q.; Yu, Z. In vitro corrosion behavior and in vivo biodegradation of biomedical β-$Ca_3(PO_4)_2$/Mg–Zn composites. *Acta. Biomater.***2012**, *8,* 2845–2855.

[4] Zreiqat, H.; Howlett, C.R.; Zannettino, A.; Evans, P.;Schulze-Tanzil, G.; Knabe, C.; Shakibaei, M. Mechanisms of magnesium-stimulated adhesion of osteoblastic cells to commonly used orthopaedic implants.*J. Biomed. Mater. Res.***2002**, *62,* 175–184.

[5] Li, L.; Gao, J.; Wang, Y. Evaluation of cyto-toxicity and corrosion behavior of alkali-heat-treated magnesium in simulated body fluid. *Surf. Coatings Technol.* **2004**, *185*, 92–98.

[6] Staiger, M.P.; Pietak, A.M.; Huadmai, J.; Dias, G. Magnesium and its alloys as orthopedic biomaterials: A review. *Biomaterials***2006**, *27*, 1728–1734.

[7] Salahshoor, M.; Guo, Y. Biodegradable Orthopedic Magnesium-Calcium (MgCa) Alloys, Processing, and Corrosion Performance. *Materials***2012**, *5,* 135–155

[8] Witte, F.; Hort, N.; Vogt, C.; Cohen, S.; Kainer, K.U.; Willumeit, R.; Feyerabend, F. Degradable biomaterials based on magnesium corrosion. *Curr.Opin.Solid State Mater. Sci.***2008**, *12*, 63–72.

[9] Seong, J.W.; Kim, W.J. Development of biodegradable Mg–Ca alloy sheets with enhanced strength and corrosion properties through the refinement and uniform dispersion of the Mg_2Ca phase by high-ratio differential speed rolling. *Acta. Biomater.***2015**, *11*, 531–542.

[10] Gu, X.; Zhou, W.; Zheng, Y.; Dong, L.; Xi, Y.; Chai, D. Microstructure, mechanical property, bio-corrosion and cytotoxicity evaluations of Mg/HA composites. *Mater. Sci. Eng. C* **2010**, *30*, 827–832.

[11] Zheng, Y.F.; Gu, X.N.; Xi, Y.L.; Chai, D.L. In vitro degradation and cytotoxicity of Mg/Ca composites produced by powder metallurgy. *Acta. Biomater.* **2010**, *6*, 1783–1791.

[12] Witte, F.; Feyerabend, F.; Maier, P.; Fischer, J.; Störmer, M.; Blawert, C.; Dietzel, W.; Hort, N. Biodegradable magnesium-hydroxyapatite metal matrix composites. *Biomaterials***2007**, *28*, 2163–2174.

[13] Huang, Y.; Liu, D.; Anguilano, L.; You, C.; Chen, M. Fabrication and Characterization of a Biodegradable Mg-2Zn-0.5Ca/1β-Tcp Composite.*Mater. Sci. Eng. C***2015**, *54*, 120–132.

[14] Khanra, A.K.; Jung, H.C.; Hong, K.S.; Shin, K.S. Comparative property study on extruded Mg–HAP and ZM61–HAP composites. *Mater. Sci. Eng. A***2010**, *527*, 6283–6288.

[15] Kwon, S.H.; Jun, Y.K.; Hong, S.H.; Kim, H.E. Synthesis and dissolution behavior of β-TCP and HA/β-TCP composite powders. *J. Eur. Ceram. Soc.***2003**, *23*, 1039–1045.

[16] Deng, C.J.; Wong, M.L.; Ho, M.W.; Yu, P.; Dickon, H.L.N. Formation of MgO and Mg–Zn intermetallics in an Mg-based composite by in situ reactions. *Compos. Part A Appl. Sci. Manuf.***2005**, *36*, 551–557.

[17] Lei, T.; Tang, W.; Cai, S.H.; Feng, F.F.; Li, N.F. On the corrosion behaviour of newly developed biodegradable Mg-based metal matrix composites produced by in situ reaction.*Corros. Sci.***2012**, *54*, 270–277.

[18] Cao, N.Q.; Narita, K.; Kobayashi, E.; Sato, T. Evolution of the microstructure and mechanical properties of Mg-matrix in situ composites during spark plasma sintering. *Powder Metall***2016**, *59*, 302-307.

[19] Cai, S.; Lei, T.; Li, N.; Feng, F. Effects of Zn on microstructure, mechanical properties and corrosion behavior of Mg–Zn alloys. *Mater. Sci. Eng. C***2013**, *32*, 2570–2577.

[20] Gu, X.; Zheng, Y.; Cheng, Y.; Zhong, S.; Xi, T. In vitro corrosion and biocompatibility of binary magnesium alloys.*Biomaterials***2009**, *30*, 484–498.

[21] Zhang, S.; Zhang, X.; Zhao, C.; Li, J.; Song, Y.; Xie, C.; Tao, H.; Zhang, Y.; He, Y.; Jiang, Y.; Bian, Y. Research on an Mg-Zn alloy as a degradable biomaterial. *Acta Biomater.***2010**, *6*, 626–640.

[22] Zhang, S.; Li, J.; Song, Y.; Zhao, C.; Zhang, X.; Xie, C.; Zhang Y.; Tao, H.; He, Y.; Jiang, Y.; Bian, Y. In vitro degradation, hemolysis and MC3T3-E1 cell adhesion of biodegradable Mg–Zn alloy. *Mater. Sci. Eng. C***2009**, *29*, 1907–1912.

[23] Trumbo, P.; Yates, A.A.; Schlicker, S.; Poos, M. Dietary reference intakes: vitamin A, vitamin K, arsenic, boron, chromium, copper, iodine, iron, manganese, molybdenum, nickel, silicon, vanadium, and zinc. *J. Am. Diet. Assoc.***2001**, *101*, 294–301.

[24] Tapiero, H.; Tew, K.D. Trace elements in human physiology and pathology: zinc and metallothioneins.*Biomed. Pharmacother*. **2003**, *57*, 399–411.

[25] Patrick, K.B.; Emily, R.S.;, Shan, Z.; Roger, J.G.; Feng, Z.; Jeremy, G.; Jaroslaw, W.D.Biodegradable Metals for Cardiovascular Stents: from Clinical Concerns to Recent Zn-Alloys. *Adv Healthc Mater.***2016**, *5*, 1121–1140.

[26] Omori, M. Sintering, consolidation, reaction and crystal growth by the spark plasma system (SPS). *Mater. Sci. Eng. A***2000**, *287*, 183–188.

[27] Chartier, T.; Badev, A. Handbook of Advanced Ceramics, Elsevier Inc: 2013.

[28] Mann, C.K.; Yoe, J.H. Spectrophotometric determination of magnesium with sodium 1-azo-2-hydroxy-3-(2,4-dimethylcarboxanilido)-naphthalene-1-(2-hydroxybenzene-5-sulfonate). *Anal Chem.***1956**, *28*, 202–205.

[29] Watanabe, H.; Tanaka, H. Dual-wavelength spectrophotometric determination of magnesium with xylidyl blue I and nonionic surfactant. *Bunseki-kagaku***1977**, *26*, 635–639.

[30] Kumar, M.; Dasarathy, H.; Riley, C. Electrodeposition of brushite coatings and their transformation to hydroxyapatite in aqueous solutions.*J. Biomed. Mater. Res. Part A***1999**, *45*, 302.

[31] Shadanbaz, S.; Dias, G.J. Calcium phosphate coatings on magnesium alloys for biomedical applications: a review. *ActaBiomater*.**2012**, *8*,20-30.

[32] Ren, M.; Cai, S.; Liu, T.; Huang, K.; Wang, X,; Zhao, H.; Niu, S. Zhang, R. Wu, X. Calcium phosphate glass/MgF_2 double layered composite coating for improving the corrosion resistance of magnesium alloy. *J. Alloy Compd.***2014**, *591*, 34-40.

CHAPTER 4

CORROSION PROPERTIES OF HAp COATED Mg MATRIX *IN SITU* COMPOSITES

4.1. Introduction

Magnesium is one of the lightest structural metals. Magnesium matrix composites show high specific strength [1]. Thus, magnesium matrix composites are potential materials for structural device applications, which can reduce the weight of automotives and mobile electronic devices for good energy efficiency and low CO_2 gas emission.

Recently, magnesium matrix composites have emerged as promising candidates for biodegradable implant applications that do not require additional surgery for removal of the implants after healing. Basically, in order to be applied as biodegradable implant biomaterials, the materials are required to have good biocompatibitlity, ultimate tensile strength higher than that of bone (200 MPa), Young's modulus equivalent to that of bone (30 GPa), and especially, the materials should have suitable degradation rate during biodegradation process. Mg matrix composites have good biocompatibility, high initial tensile strength (>250 MPa), and Young's modulus equivalent to that of bone (30 GPa) to avoid stress shielding effect [2, 3]. However, the main drawback of Mg matrix composites is fast degradation rate *in vivo* and *in vitro* [4-6]. The fast degradation rate of the materials results in fracture of implant before bone healing due to deterioration of material strength. Therefore, it is very essential to moderate the degradation rate by improving corrosion resistance of Mg matrix composites for practical applications. In our previous works, Mg matrix *in situ* composites with good corrosion resistance and mechanical properties were fabricated via spark plasma sintering from mixed Mg-ZnO powder. In this work, in order to enhance significantly corrosion resistance of as fabricated Mg matrix *in situ* composites, surface coating was applied.

Surface coating is very effective method to enhance the corrosion resistance of materials [7-12]. Especially, hydroxyapatite (HAp) and some other calcium phosphate compounds are potential coating materials to avoid severe corrosion of Mg materials [7-12]. Because HAp is main component of bone and the calcium phosphate compounds precipitated from the simulated body fluids enhancing the corrosion resistance of Mg [13, 14]. Recent researches of Hiromoto *et al.* demonstrated that HAp grows well on surface of Mg alloys and shows very effective in improvement of corrosion properties and biocompatibility of Mg alloys [15-17]. Therefore, in this chapter, HAp coating was selected as surface modification method.

4.2. Experimental procedures

4.2.1. Sample preparation

Based on result from corrosion test previously. It could be seen that Mg-10ZnO composites exhibited much better corrosion resistance compared with Mg-20ZnO composites. Therefore, in this chapter, Mg-10ZnO composites are the main objective of research.

Mg powders with a purity of 99.5% and particle size of 180 μm and ZnO powders with a purity of 99.9% and particle size of 1 μm supplied by Kojundo Chemical Laboratory were used for sample preparation. Mg-10 wt-%ZnO powders was mixed homogeneously with zirconia balls (2.5 of ball to powder weight ratio) in an argon atmosphere using a planetary micro ball mill (Pulverisette 7) with rotation speed of 500 rpm for 12 h. No process control agent was used. The mixed powders were set inside the Tungsten-Carbide die of 120 mm in height and 15 mm in an inner diameter for the spark plasma sintering using a 511S, Syntex SPS system.

Three kinds of samples were fabricated with different ZnO weight fractions and sintering conditions. Mg-10ZnO-10min sample was directly sintered by SPS while Mg-10ZnO-2h30+10min sample was sintering in vacuum furnace before sintering by SPS. The details of fabrication process are shown in Table 4.1.

All the sintering processes were performed in a high vacuum chamber. After sintering processes, the samples were cooled down to room temperature inside the vacuum chamber.

Table 4.1. Samples used for surface treatment.

Sample name	Composition	Sintering by vacuum furnace (T=550^{o}C, P=0MPa)	Sintering by SPS (T=550^{o}C, P=50MPa)
Mg	Pure Mg powder	0	10 min
Mg-10ZnO-10min	Mg-10 mass% ZnO	0	10 min
Mg-10ZnO-2h30+10min	Mg-10 mass% ZnO	2h30	10min

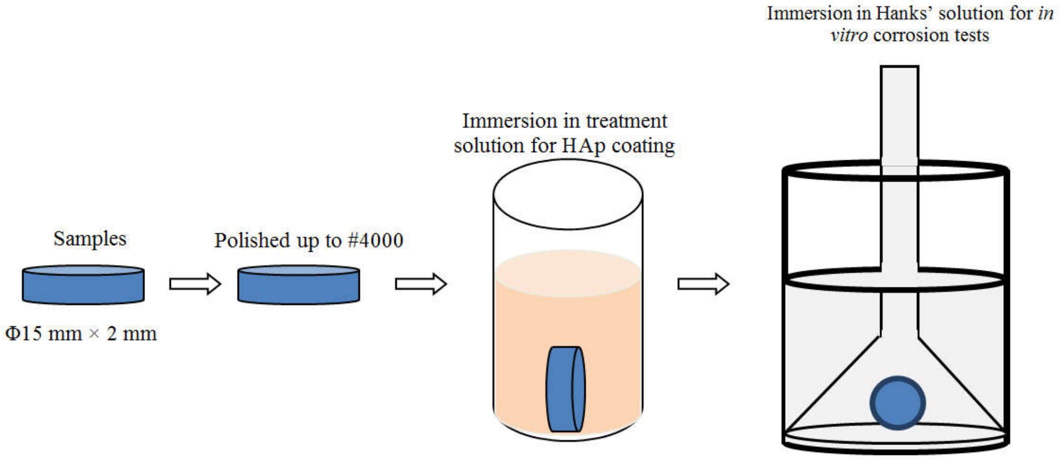

Figure 4.1. Illustration of sample preparation, HAp coating, and immersion test process.

4.2.2. HAp coating

The sintered composites were machined into disk shape with the size of *Φ*15 × 2 (mm). The machined samples were ground using SiC papers up to 4000 grit, successively polished with ¼-μm diamond paste, ultrasonically cleaned with ethanol and then dried for HAp coating process. Treatment solutions for HAp coatings were prepared with ethylenediaminetetraaceticacid calcium disodium salt hydrate ($C_{10}H_{12}CaN_2Na_2O_8$, Ca-EDTA) with the concentration of 0.5 M/L, potassium dihydrogen phosphate (KH_2PO_4) with the concentration of 0.5 M/L, and sodium hydroxide (NaOH) was used for pH adjustment. The discs were immersed in the treatment solution at 90 ^oC for 2 h. The HAp coating process is illustrated in Figure 4.1.

The coated samples then were characterized by XRD, OM, and BSEM to evaluate the growth of HAp coating layer.

4.2.3. Immersion Tests

Disk shape specimens with dimensions of *Φ*14 x 2 (mm) were immersed in Hanks' solution at 37^oC for 14 days in air. The specimens were placed on a clip to expose the bottom surface to the solution (Figure 4.1). The composition of Hanks' solution is described in Table 4. 2. The ratio of surface area to solution volume was 1 cm^2 : 50 ml. The immersion test was conducted in triplicate for each sample condition.

Amount of Mg^{2+} ions dissolved in the sampled medium were quantified by a colorimetric method using Xylidyl blue-I [18, 19]. In addition, hydrogen gas generated was collected by a burette with a funnel which was placed over the immersed sample. XRD, SEM, and EDX were conducted for the samples after the immersion test for 14 days.

Table 4.2. Composition of Hanks' solution using for immersion tests.

Reagent	**NaCl**	**KCl**	**$Na_2HPO_4.H_2O$**	**KH_2PO_4**	**$MgSO_4.7H_2O$**	**$NaHCO_3$**	**$CaCl_2$**
Concentration (g/L)	8	0.4	0.06	0.06	0.2	0.35	0.14

4.2.4. Polarization Tests and Impedance Tests

Polarization tests were carried out in Hanks' solution. The surface was coated with epoxy resin to expose the measurement area of 1 cm^2 to to Hanks' solution at 37^oC. The open circuit potential was mesured for 1500 s. Subsequently, potentiodynamic polarisation curves were mesured in the potential range from -0.1 V vs. open circuit potential (E_{ocp}) at a scan rate of 1 mV/s. Electrochemical impedance spectroscopy (EIS) measurements were performed at E_{ocp} with the scan frequency ranged from 100 kHz to 0.01 Hz, and with the perturbation amplitude of 5 mV. The reference and counter electrodes were saturated Ag/AgCl and Pt electrodes, respectively.

4.3. Results and Discussion

4.3.1. HAp growth on surface of sintered samples

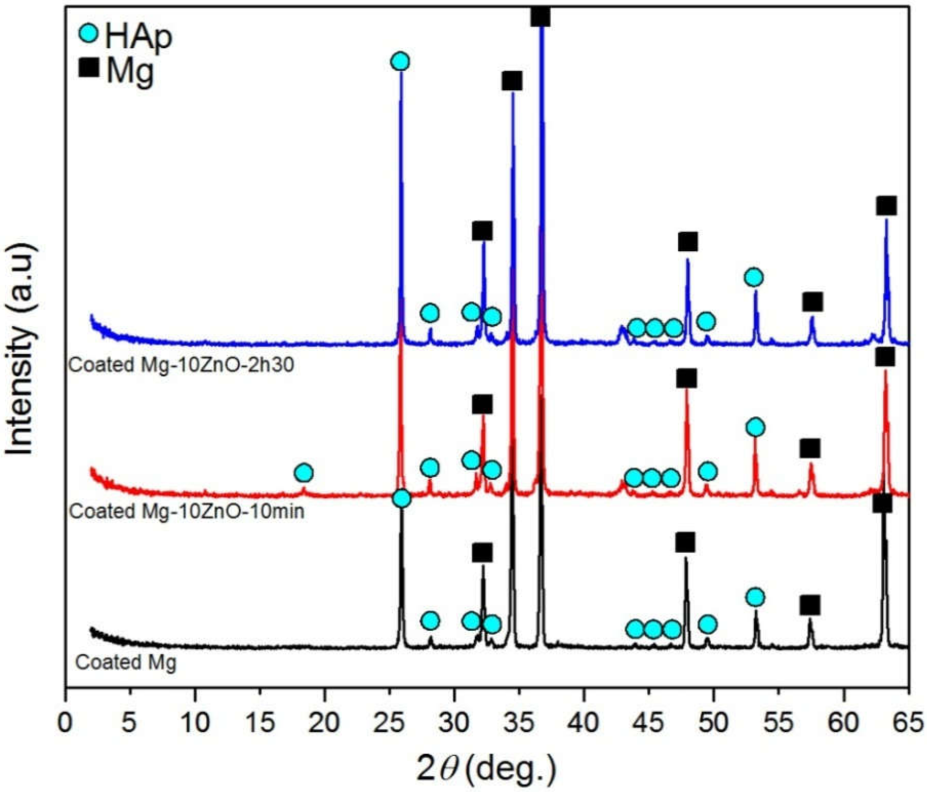

Figure 4.2. XRD patterns of 2h coated Mg, Mg-10ZnO-10min, and Mg-10ZnO-2h30+10min.

Figure 4.2 shows XRD patterns of 2h coated Mg, Mg-10ZnO-10min, and Mg-10ZnO-2h30 samples. It can be seen that all samples show high peaks of HAp and there were no peaks related to OCP detected. This demonstrated good growth of HAp on the surface of all samples. In addition, peaks of HAp on XRD pattern of coated Mg-10ZnO-2h30 samples shows highest intensity, while those of coated Mg shows lowest intensity. This indicates that HAp grows better on the surface of composites than on the surface of pure Mg.

Figure 4.3 to Figure 4.5 show SEM micrographs of 2h coated Mg, Mg-10ZnO-10min, and Mg-10ZnO-2h30+10min samples with different magnifications. As could be seen that all surfaces were covered by HAp layers. For Mg-10ZnO-2h30+10min, there were random appearance of flower-like crystal on the surface. This might suggested higher growth quality of HAp on this sample. In addition, it can be seen that the grain boundaries appreared on the surface of coated Mg, it demonstrated that the HAp layer on surface of pure Mg is very thin.

Optical micrographs of coated samples were shown in Figure 4.6. As for the HAp coated Mg sample, although the HAp layer grows homogeneously on the surface of Mg substrate, the grain boundaries between Mg particles appear clearly indicating that HAp layer is thin. There is no grain boundary appeared on the surface of HAp coated composites, however, the second phase can be seen through transparent HAp layer. From optical micrograph of HAp coated Mg-10ZnO-10min sample, it can be seen that the HAp crystal is preferred to grow following the boundaries between Mg matrix and the second phase. This is might be due to high amount of MgO at these areas of the substrate promotes the growth of HAp in these areas faster than other areas.

As for HAp coated Mg-10ZnO-2h30+10min, the coating layer shows homogeneouly with random distribution of white partiles. These white particles appear as flower-like structure in the SEM images of this samle. This might suggested highest quality of HAp growth on this sample compared to two other samples.

Figure 4.7 shows cross section SEM images of HAp coated samples. As could be seen that, HAp layers on all three samples show structure of two sub-layers, the inner dense sub-layer and the outer sub-layer with plate like structure. HAp layer on pure Mg has thickness at around 3 µm, while the thickness of HAp layer on the composites is around 5 µm. This result confirms that HAp grows on composites better than on pure Mg.

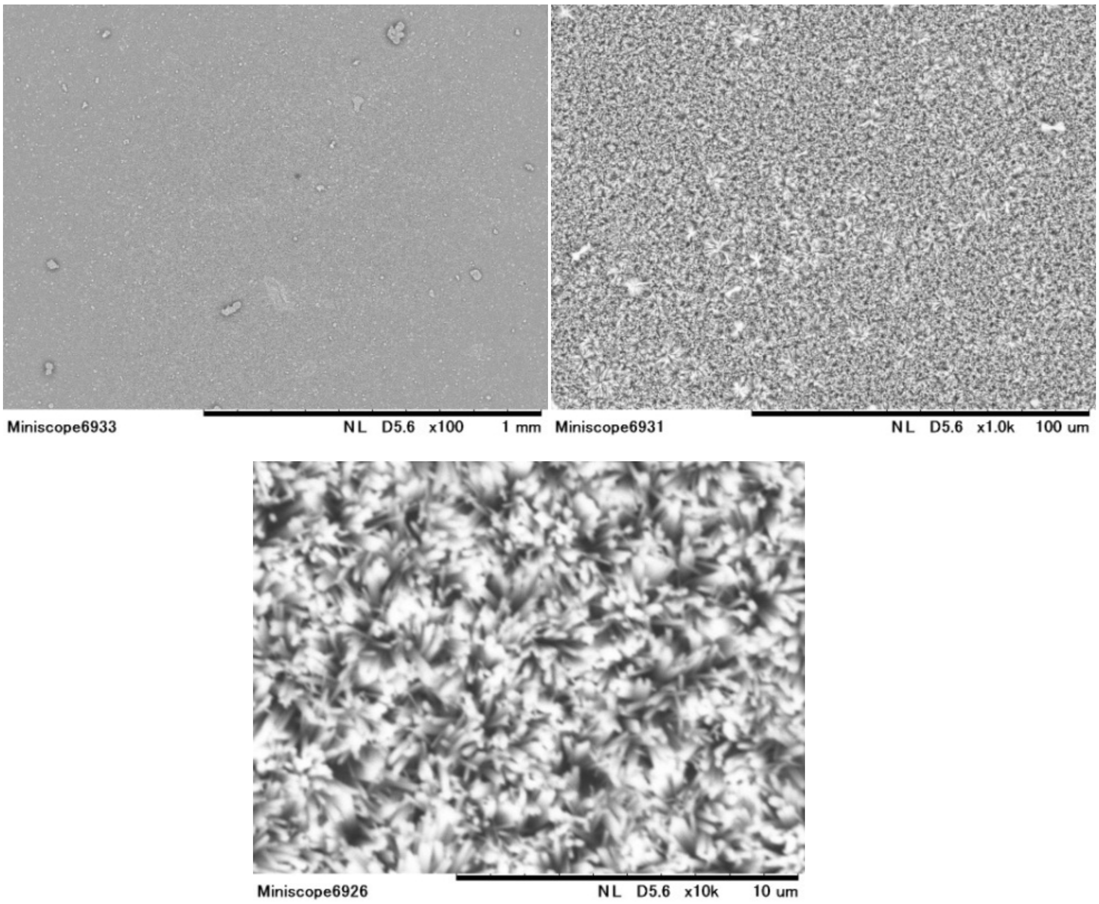

2h coated Mg

Figure 4.3. SEM micrographs of HAp coated pure Mg

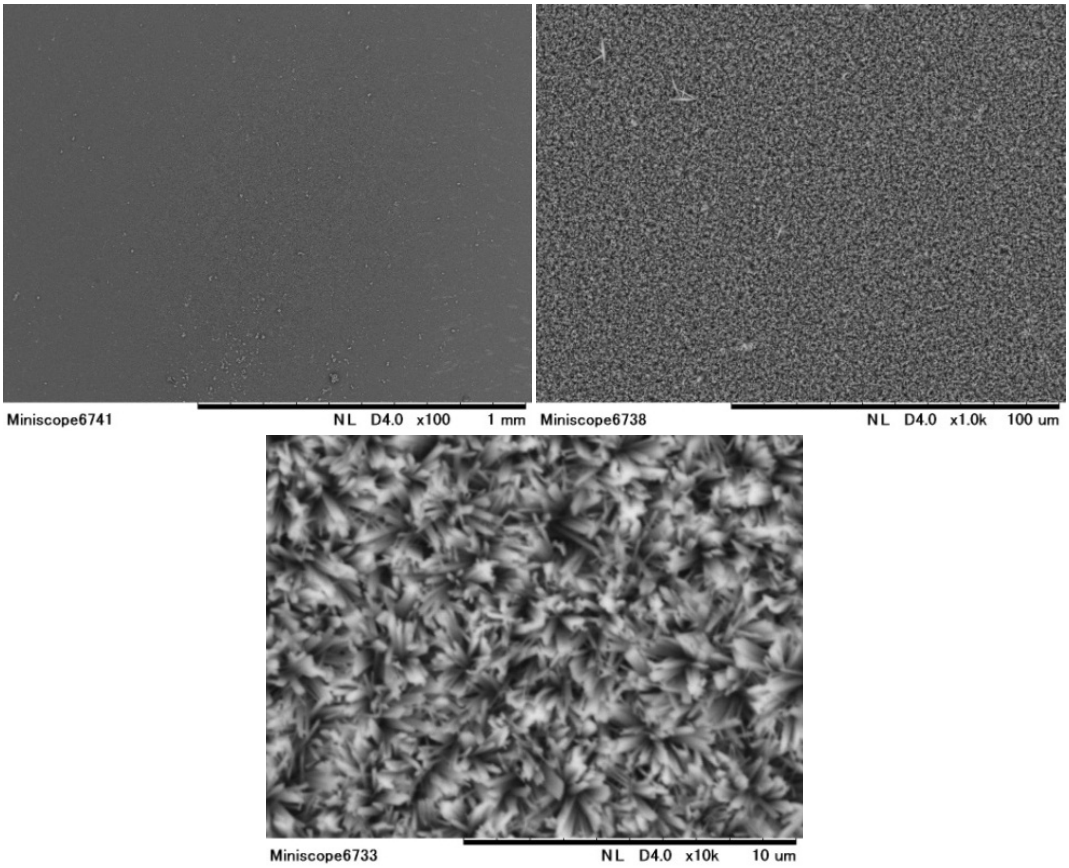

2h coated Mg-10ZnO-10min

Figure 4.4. SEM micrographs of HAp coated Mg-10Zn0-10min

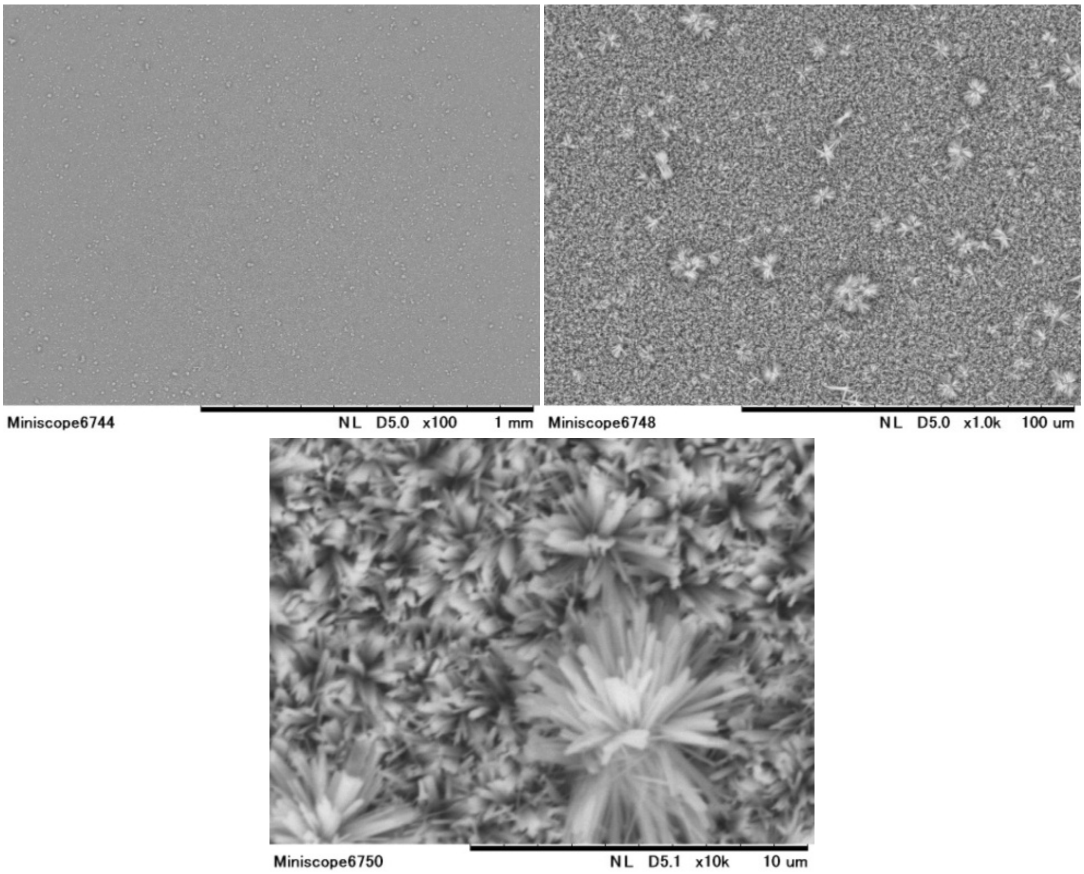

2h coated Mg-10ZnO-2h30

Figure 4.3. SEM micrographs of 2h coated Mg-10ZnO-2h30+10min.

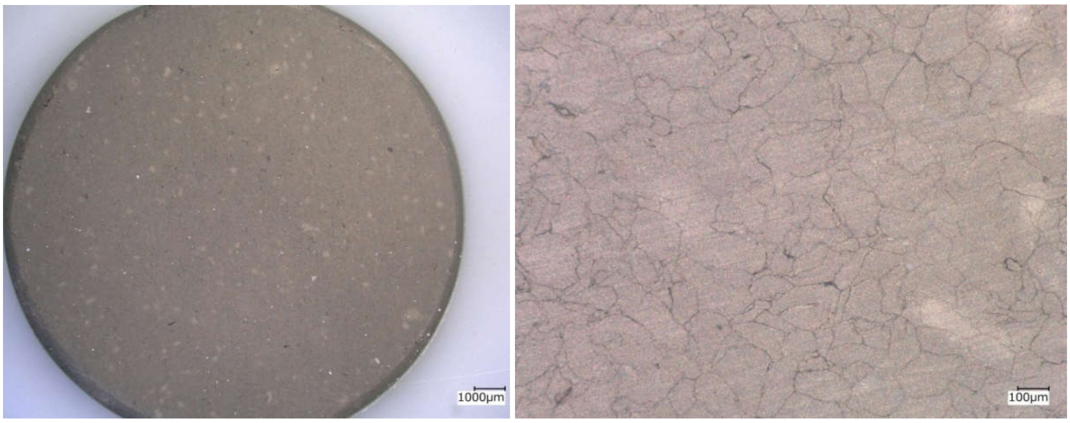

2h coated Mg

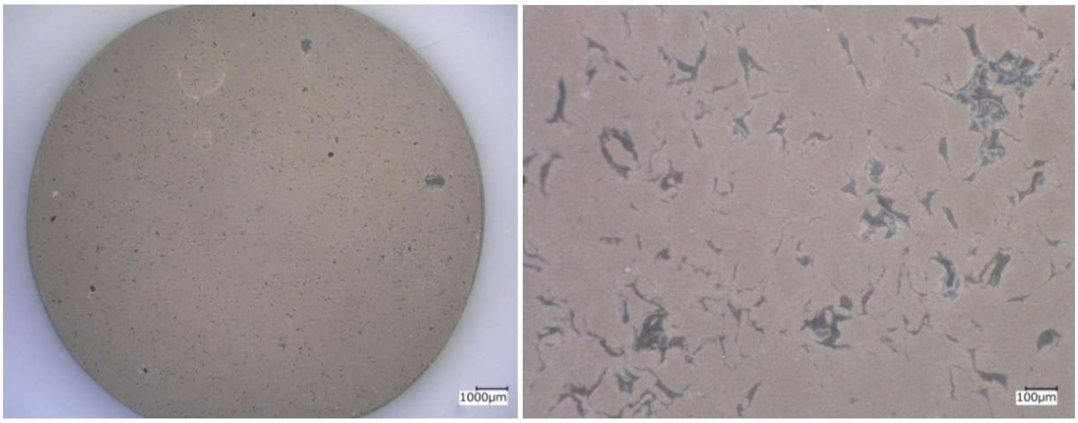

2h coated Mg-10ZnO-10min

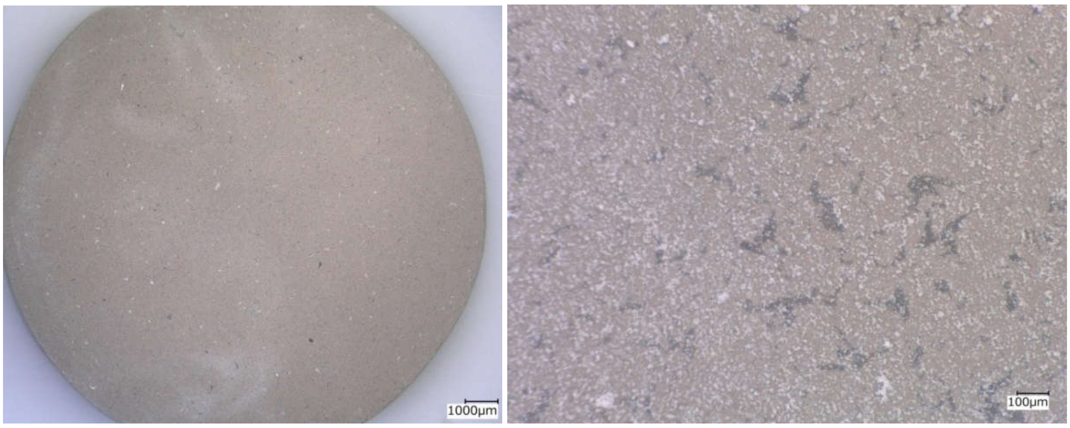

2h coated Mg-10ZnO-2h30

Figure 4.6. Optical micrographs of 2h coated Mg, Mg-10ZnO-10min, and Mg-10ZnO-2h30+10min.

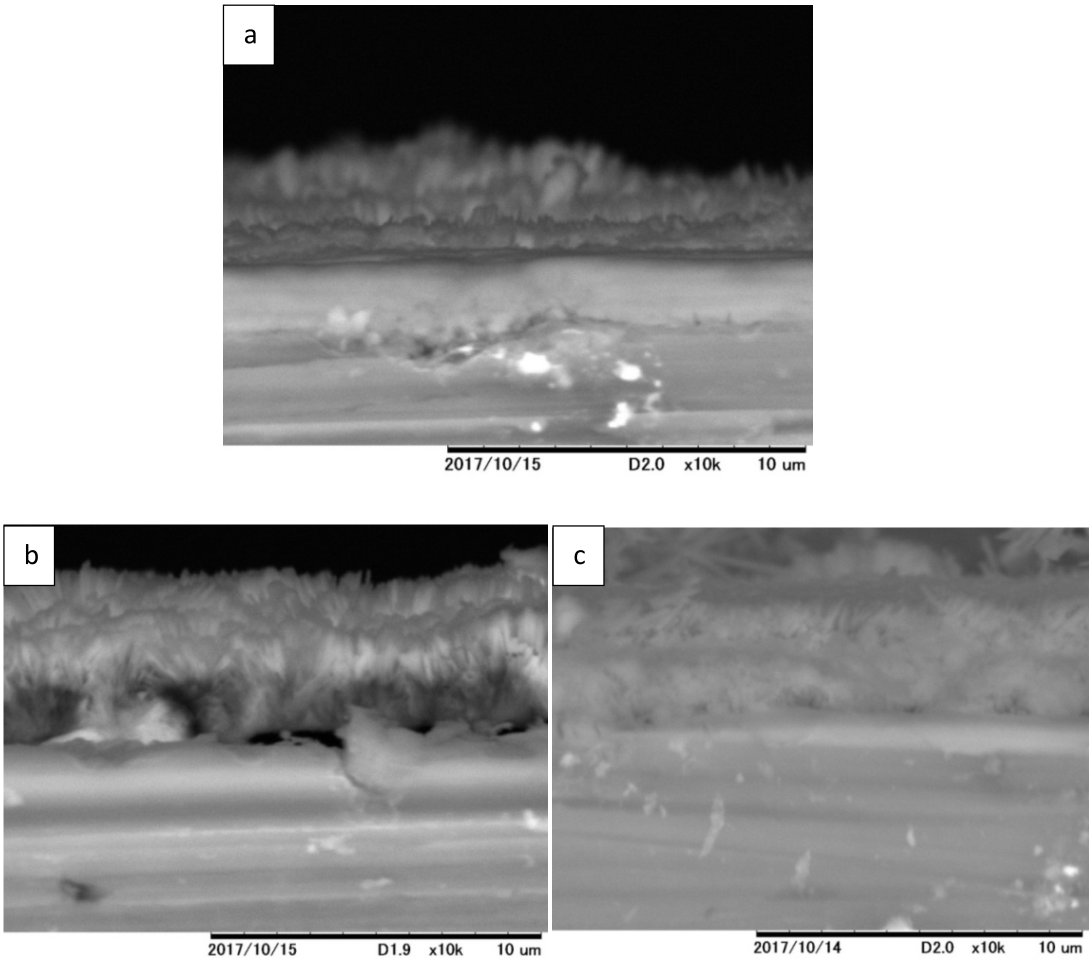

Figure 4.7. SEM micrographs of cross section of HAp coated samples, a) pure Mg, b) Mg-10ZnO-10min, and c) Mg-10ZnO-2h30+10min

4.3.2. Immersion tests

Figure 4.8 shows amount of Mg ion released per cm^2 in Hanks' solution as function of immersion period of 2h coated Mg, Mg-10ZnO-10min, and Mg-10ZnO-2h30+10min samples. It could be seen that coated Mg-10ZnO-2h30+10min samples showed lowest corrosion rate while Mg exhibited highest amount of Mg^{2+} ion released. Compared to uncoated samples from previous chapter, all coated samples showed less amout of Mg^{2+} ion released at the same periods of immersion. This suggested positive effect of HAp coating on the corrosion resistance of as-fabricated composites.

Figure 4.9 shows hydrogen-evolution trend of HAp coated samples during 14 days immersion in Hanks' solution. The hydrogen-evolution trend shows similar trend to Mg^{2+} ion release behavior. Specifically, coated Mg-10ZnO-2h30+10min samples showed lowest hydrogen gas release while coated Mg exhibited highest amount of hydrogen gas release. This result confirms that coated Mg-10ZnO-2h30+10min samples has lowest corrosion rate, while coated pure Mg showed highest corrosion rate.

Figure 4.10 shows surfaces of immersed coated Mg-10ZnO-10min and Mg-10ZnO-2h30+10min samples. For coated pure Mg, the samples were almost fractured during immersion tests. As could be seen clearly that the surface of coated Mg-10ZnO-10min demonstrated more severe corrosion and much corrosion product deposited, while there was local corrosion occurred on small area on the surface of Mg-10ZnO-2h30+10min samples. This result is in consistence with Mg^{2+} ion released measurement from immersion tests.

Figure 4.11 shows SEM images of Mg-10ZnO-10min and Mg-10ZnO-2h30+10min samples after immersion for 14 days in Hanks' solution. It can be seen that, there is a thick corrosion product layer on the surface of immersed coated Mg-10ZnO-10min samples. While, the the crystal structure of HAp layer on the surface of coated Mg-10ZnO-2h30+10min sample still can be seen. This suggested that, only outer layer of HAp coated layer on the surface of Mg-10ZnO-2h30+10min sample was corroded.

Figure 4.12 and Figure 4.13 show EDX analysis and SEM image with elemental mapping on the surface of immersed HAp coated Mg-10ZnO-10min sample. From atomic pecent analysis, it could be seen that calcium phosphate is main component of corrosion product on the surface of this sample. As the result, atomic percent ratio between Ca and P is approximately 15:11.5. Since atomic percent ratio of Ca and P of HAp is 10:6, it might be concluded that there are some other calcium phosphate compounds as corrosion product deposited on the surface of this sample during immersion test.

Figure 4.14 and Figure 4.15 show EDX analysis and SEM image with elemental mapping on the surface of immersed HAp coated Mg-10ZnO-2h30+10min sample. From atomic percent analysis, it should be noticed that atomic percent ratio of Ca and P is approximately 19:11, this is similar to atomic percent ratio of Ca and P in HAp (10:6). This indicates that there is only little corrosion product deposited on the surface of immersed HAp coated Mg-10ZnO-2h30+10min sample. The surface of this sample consists of mainly HAp with corroded outer sub-layer. This is in consistent with SEM image because, the structure of inner sub-layer of HAp appeared clearly on the surface of immersed sample.

The above results indicate that HAp coated Mg-10ZnO-2h30+10min has much better corrosion resistance compared with HAp coated Mg-10ZnO-10min composite. This is reasonable, because of 2 reasons. Firstly, Mg-10ZnO-2h30+10min substrate has better corrosion resistance compared to HAp coated Mg-10ZnO-10min substrate. This was demonstrated in previous chapter. Secondly, HAp coating layer on HAp coated Mg-10ZnO-2h30+10min show little thicker and denser compared to that on HAp coated Mg-10ZnO-10min sample.

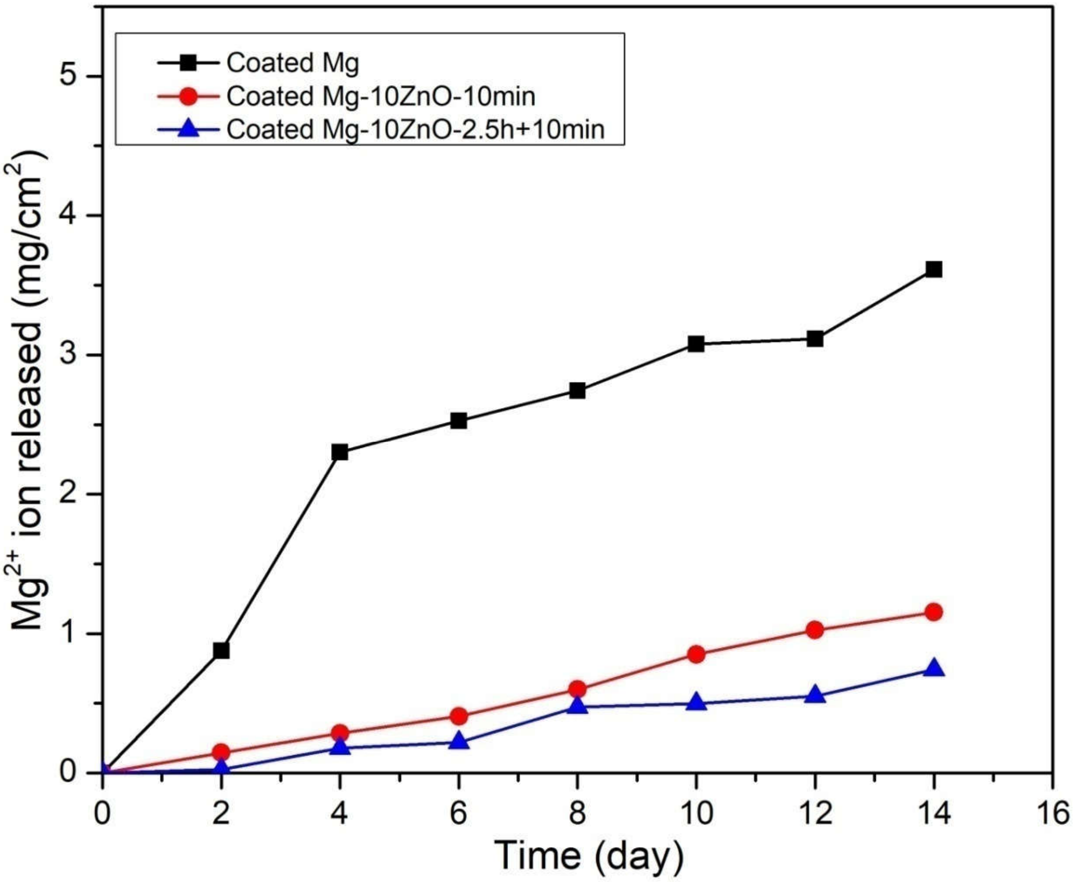

Figure 4.8. Amount of Mg^{2+} ion release per cm^2 in the medium during immersion tests.

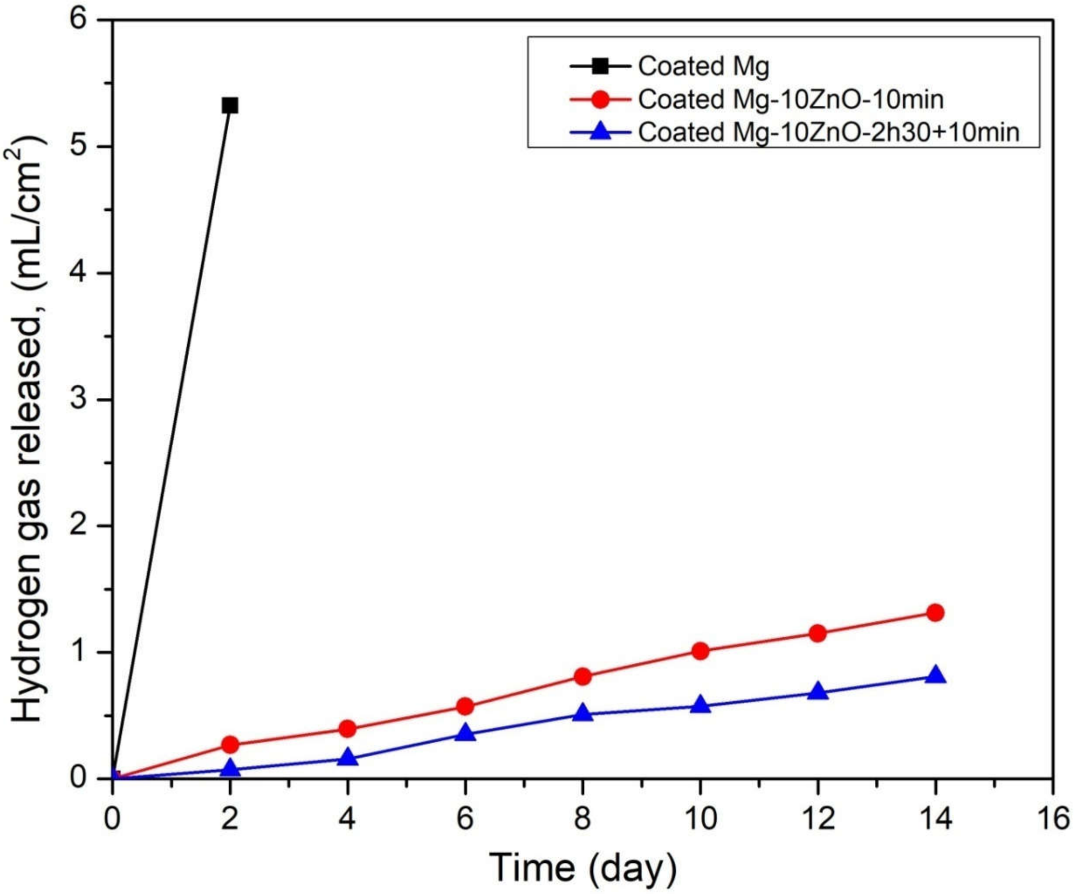

Figure 4.9. Hydrogen gas evolution during immersion tests

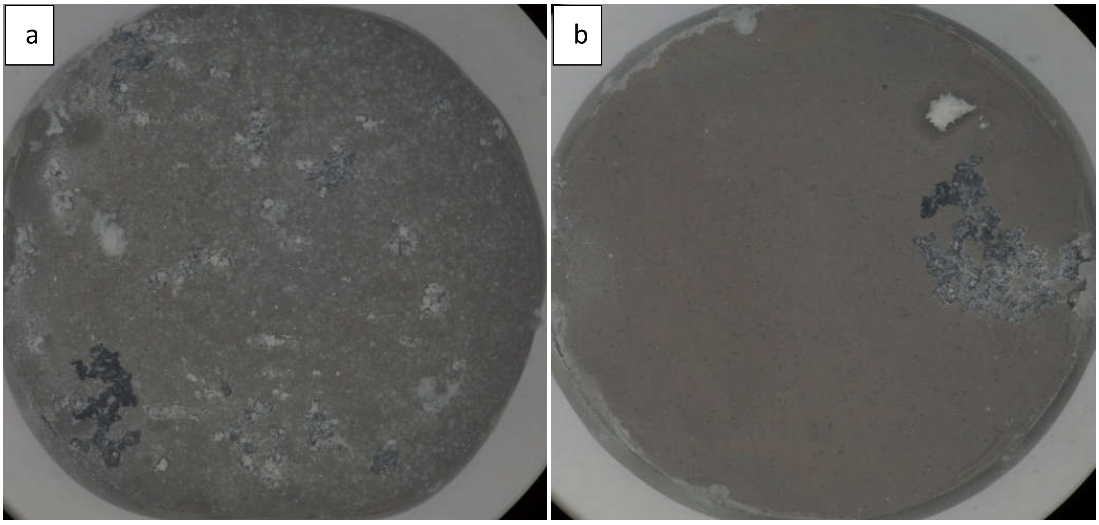

Figure 4. 10. Surfaces of immersed samples: a. coated Mg-10ZnO-10min, b. coated Mg-10ZnO-2h30+10min.

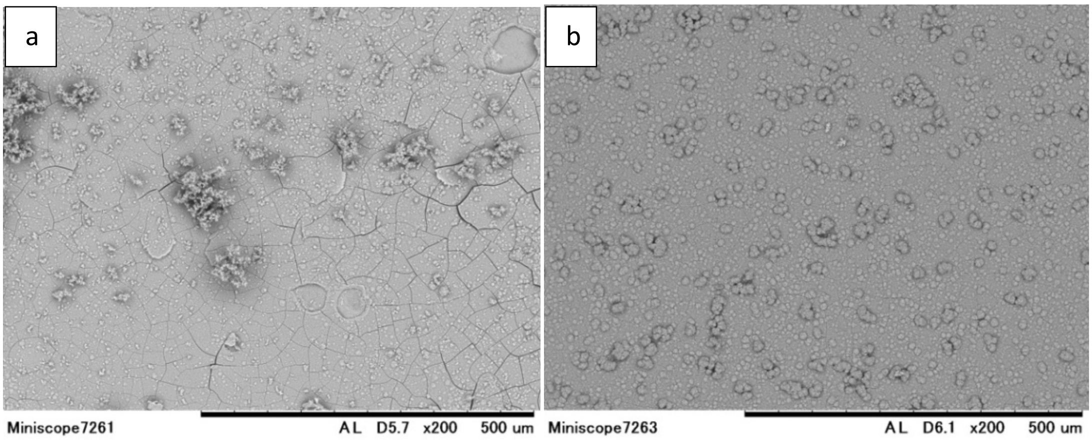

Figure 4.11. SEM micrographs of immersed samples: a. coated Mg-10ZnO-10min, b. coated Mg-10ZnO-2h30+10min.

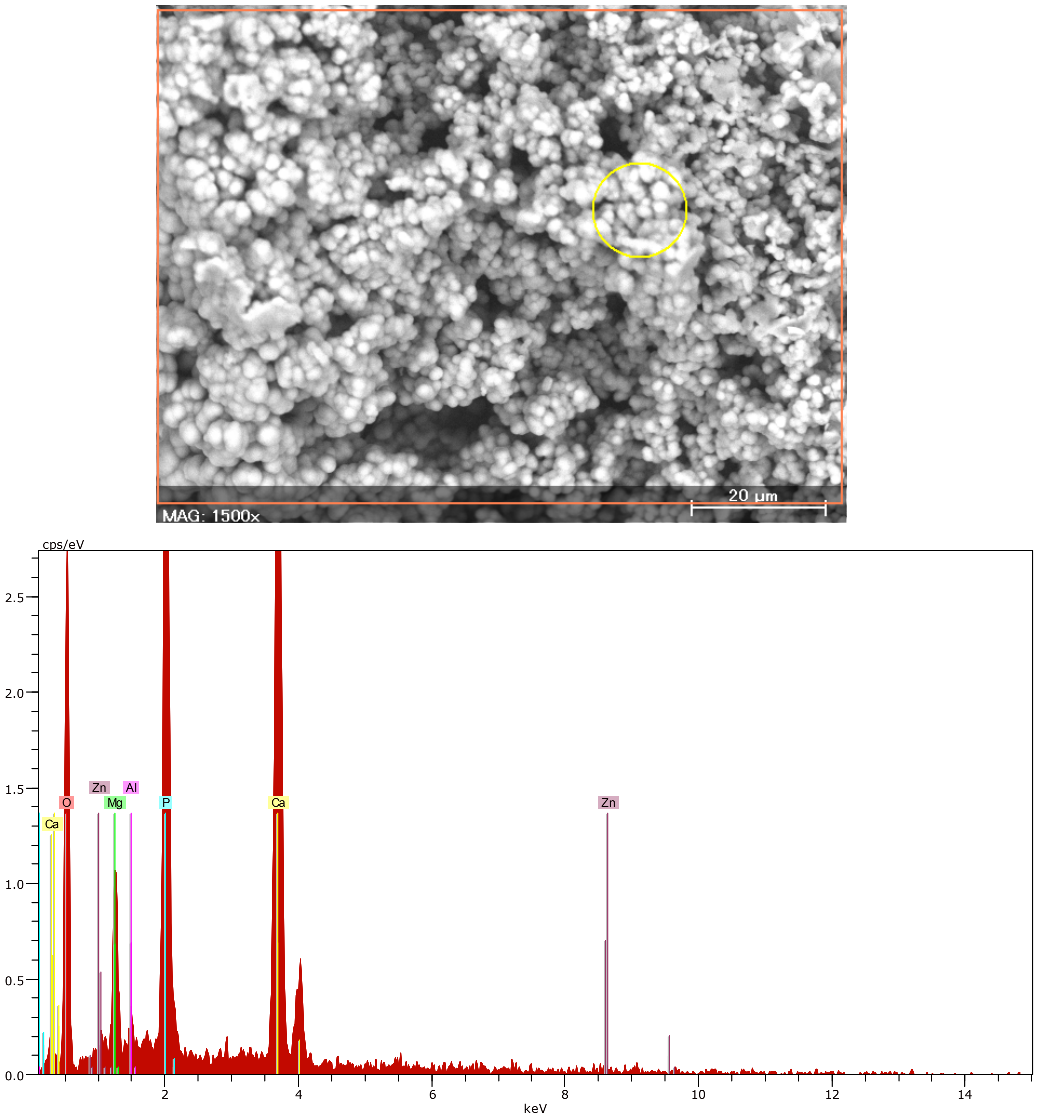

```
Element     AN  Series   norm. C Atom. C
                          [wt.%]  [at.%]
--------------------------------------
Oxygen       8  K-series   50.52   68.98
Calcium     20  K-series   27.36   14.91
Phosphorus  15  K-series   16.22   11.44
Magnesium   12  K-series    4.23    3.80
Aluminium   13  K-series    0.65    0.53
Zinc        30  K-series    1.02    0.34
```

Figure 4.12. EDX analysis of immersed HAp coated Mg-10ZnO-10min

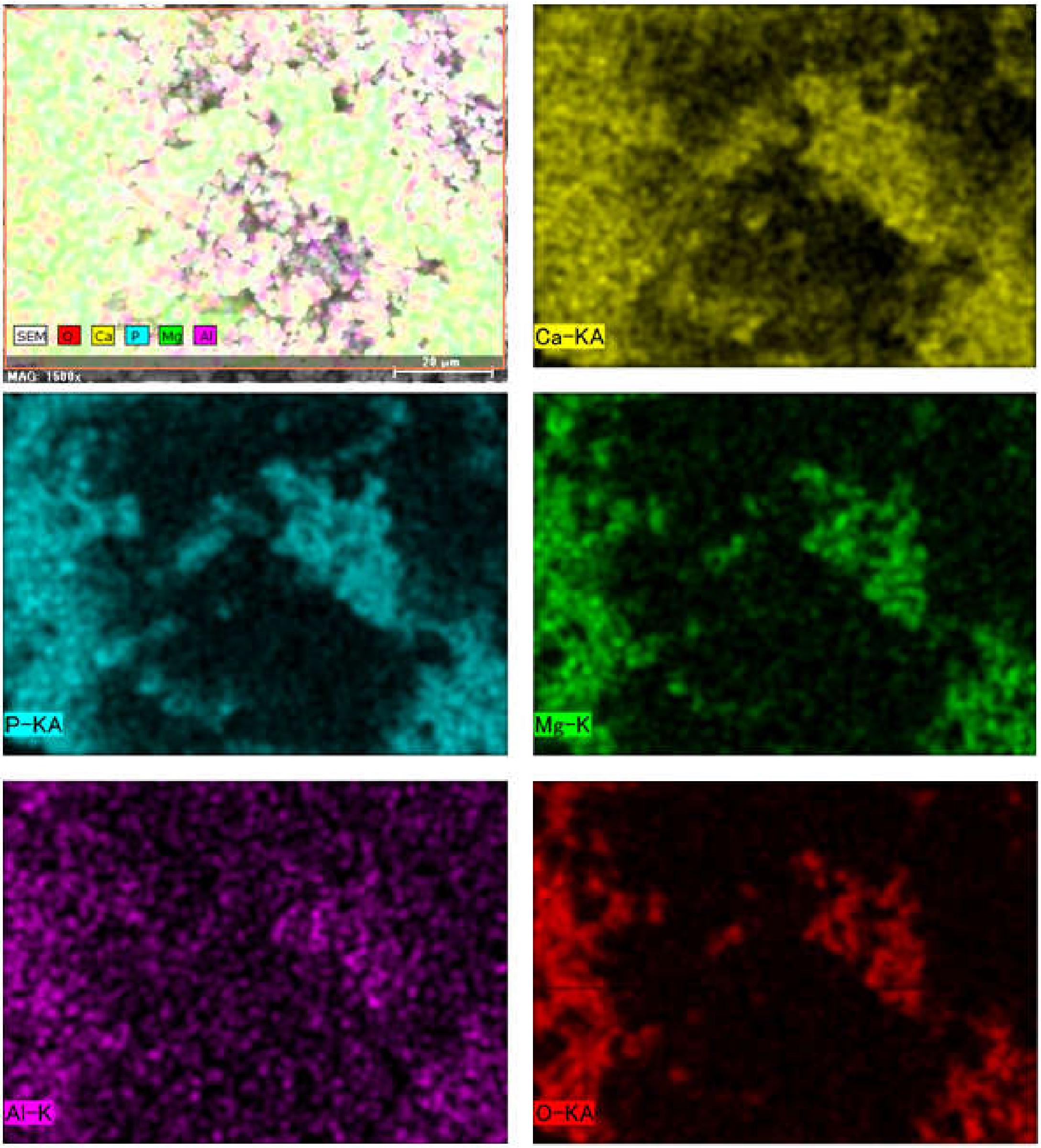

Figure 4. 13. SEM images of elemental mapping images of immersed HAp coated Mg-10ZnO-10min

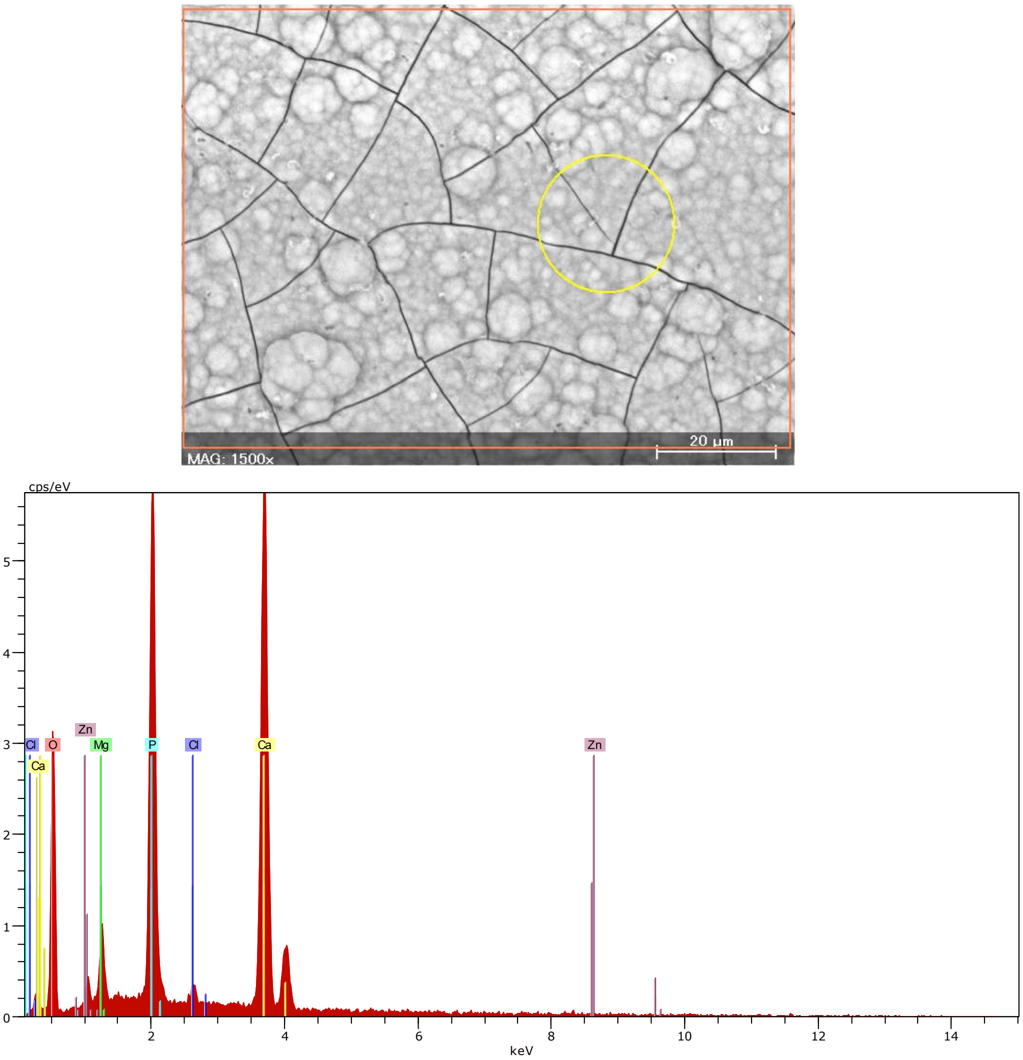

```
Element     AN  Series   norm. C Atom. C
                          [wt.%]  [at.%]
----------------------------------------
Oxygen      8  K-series   47.59   67.11
Calcium     20 K-series   33.88   19.07
Phosphorus  15 K-series   15.30   11.14
Magnesium   12 K-series    2.36    2.19
Chlorine    17 K-series    0.66    0.42
Zinc        30 K-series    0.21    0.07
```

Figure 4.14. EDX analysis of immersed HAp coated Mg-10ZnO-2h30+10min

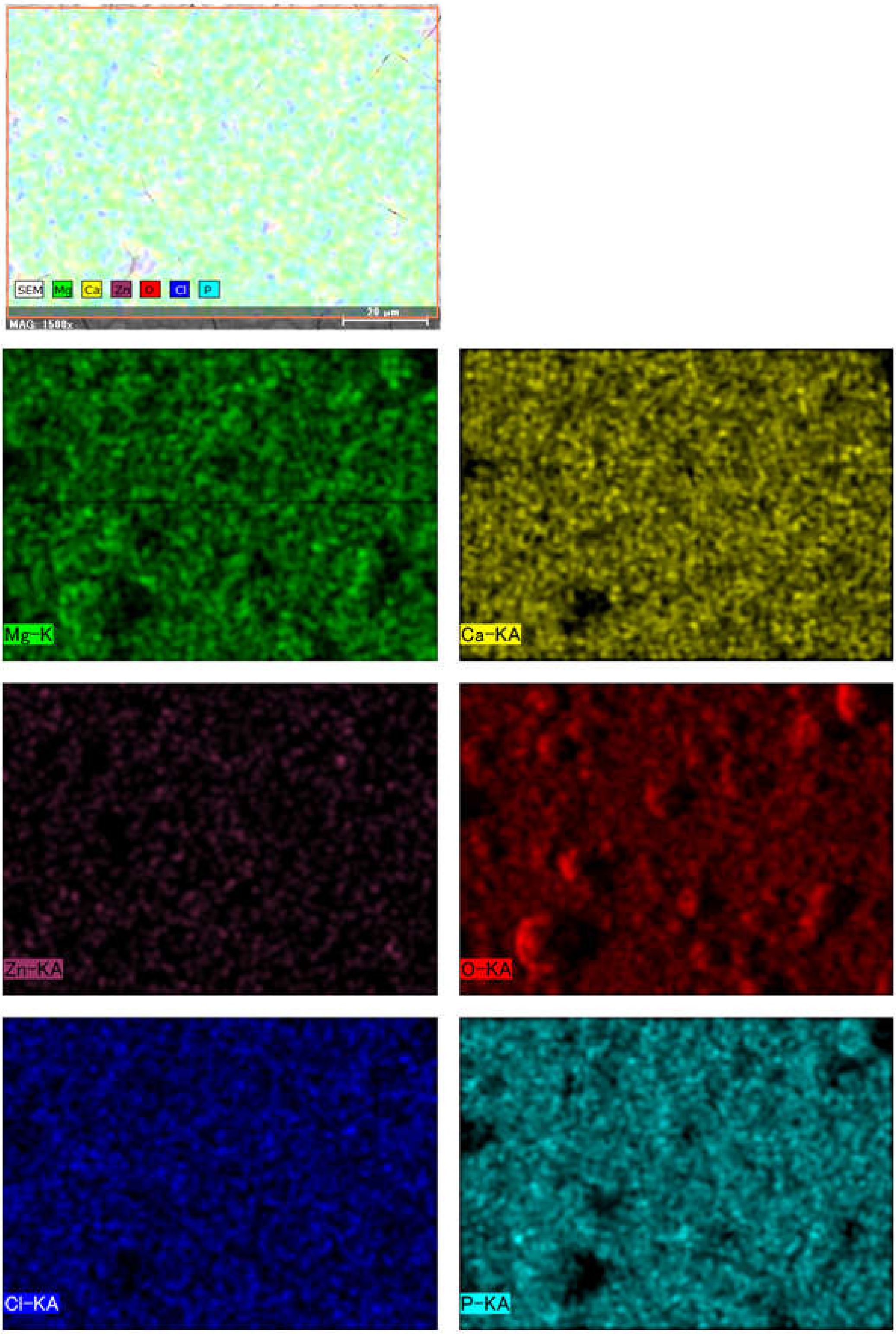

Figure 4. 15. SEM images of elemental mapping images of immersed HAp coated Mg-10ZnO-2h30+10min

4.3.3. Polarization and Impedance tests

Figure 4.16 shows polarization curves of 2h coated Mg, Mg-10ZnO-10min, and Mg-10ZnO-2h30+10min samples. As shown, coated Mg-10ZnO-2h30+10min specimen exhibited lowest corrosion current density (I_{corr}) and most positive corrosion potential (E_{corr}), while coated Mg specimen showed highest corrosion current density and most negative corrosion potential. The order of corrosion current densities and corrosion potentials confirmed that coated Mg-10ZnO-2h30+10min specimen exhibited highest corrosion resistance while coated Mg showed lowest. The result also indicated that coated composites sintered for 2h30+10min exhibited lower corrosion compared with composites sintered only by SPS for 10min. This result is agreement with immersion test results.

Figure 4.17 shows Bode plots of 2h coated Mg, Mg-10ZnO-10min, and Mg-10ZnO-2h30+10min samples. The impedance spectra showed that the polarization resistance of Mg-10ZnO-10min sample increased from 0 h to 0.5 h, decreased from 1 h to 4 h, and recovered at 6 h. The impedance spectrum from 1 h to 4 h showed a lot of fluctuations and the phase shift became below zero. These results indicate that the local corrosion occurred from 1 h to 4 h and the corrosion pit was recovered afterwards. HAp coated Mg-10ZnO-2h30+10min samples shows larger increase of R_p than HAp coated Mg-10ZnO-10min sample. In addition, Rp at 6 h of HAp coated Mg-10ZnO-2h30+10min samples was higher than that of B-1 than HAp coated Mg-10ZnO-10min sample. This result is consistent with the smaller Mg^{2+} ion release from HAp coated Mg-10ZnO-2h30+10min samples than that from HAp coated Mg-10ZnO-10min sample in the static immersion test. In addition, Bode plots of HAp coated Mg-10ZnO-2h30+10min samples also suggest that local corrosion occurred at 0.5 h to 4h since there are a lot of fluctuations and the phase shift became below zero during this period of immersion.

Figure 4.18 shows impedance (Z) of coated Mg, Mg-10ZnO-10min, and Mg-10ZnO-2h30+10min samples at different immersion times. As could be seen that, for coated composites, Z increased significantly at the beginning of immersion and decreased after 0.5 hour immersion. This indicates local corrosion occurred after 0.5 hour. However, Z increased again after 1 hour for coated Mg-10ZnO-2h30+10min samples and after 4 hours for coated Mg-10ZnO-10min sample. This is attributed as calcium phosphate precipitated on the surface of the composites to form protective layer and avoid corrosion occurred after 1 hour or 4 hours for coated Mg-10ZnO-10min and Mg-10ZnO-2h30+10min samples respectively. While for coated Mg sample, Z decreased throughout all immersion period. The result from impedance tests also confirmed that coated Mg-10ZnO-2h30+10min samples has highest corrosion resistance while coated pure Mg exhibited lowest. The result also demonstrated improvement of corrosion resistance of coated samples compared to uncoated samples.

Figure 4.19 shows morphology of samples after impedance tests. As could be seen that, corrosion occurred on whole surface of pure Mg sample, while some local corrosion appeared on the surface of composites. Some white particles on the local corrosion regions are calcium phosphate – corrosion product. This corrosion product acts as protective layer for to avoid further severe corrosion. This explains the recovery of impedance of composites during impedance tests.

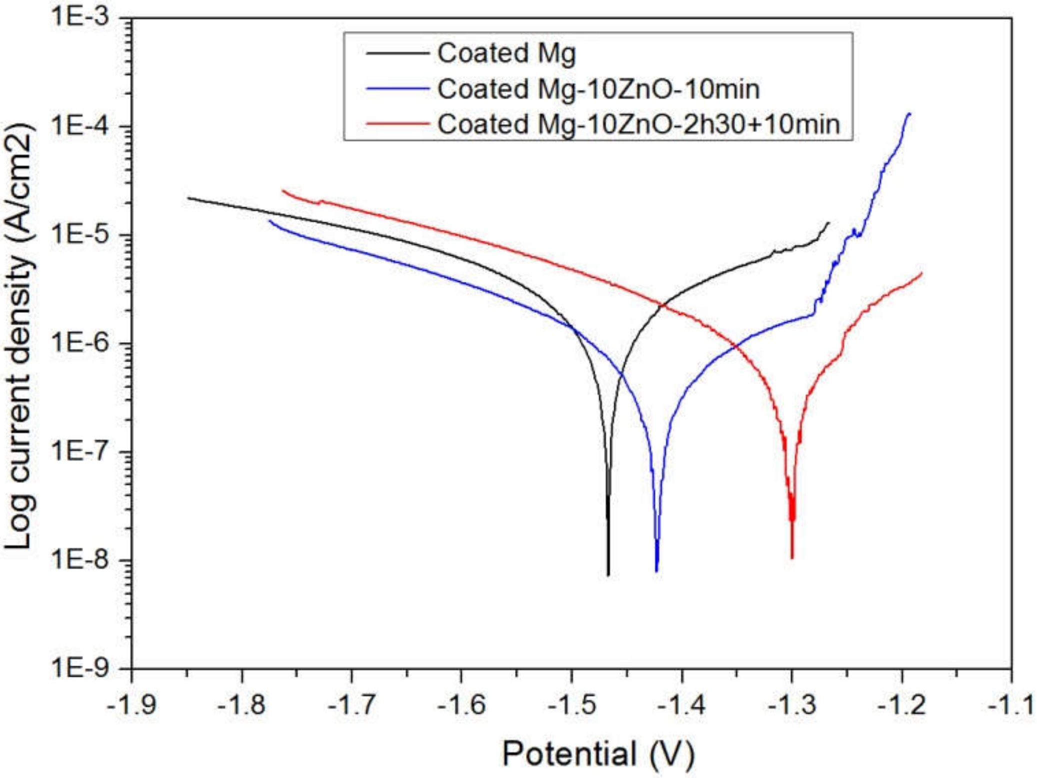

Figure 4.16. Polarization curves of as coated samples in Hanks' solution.

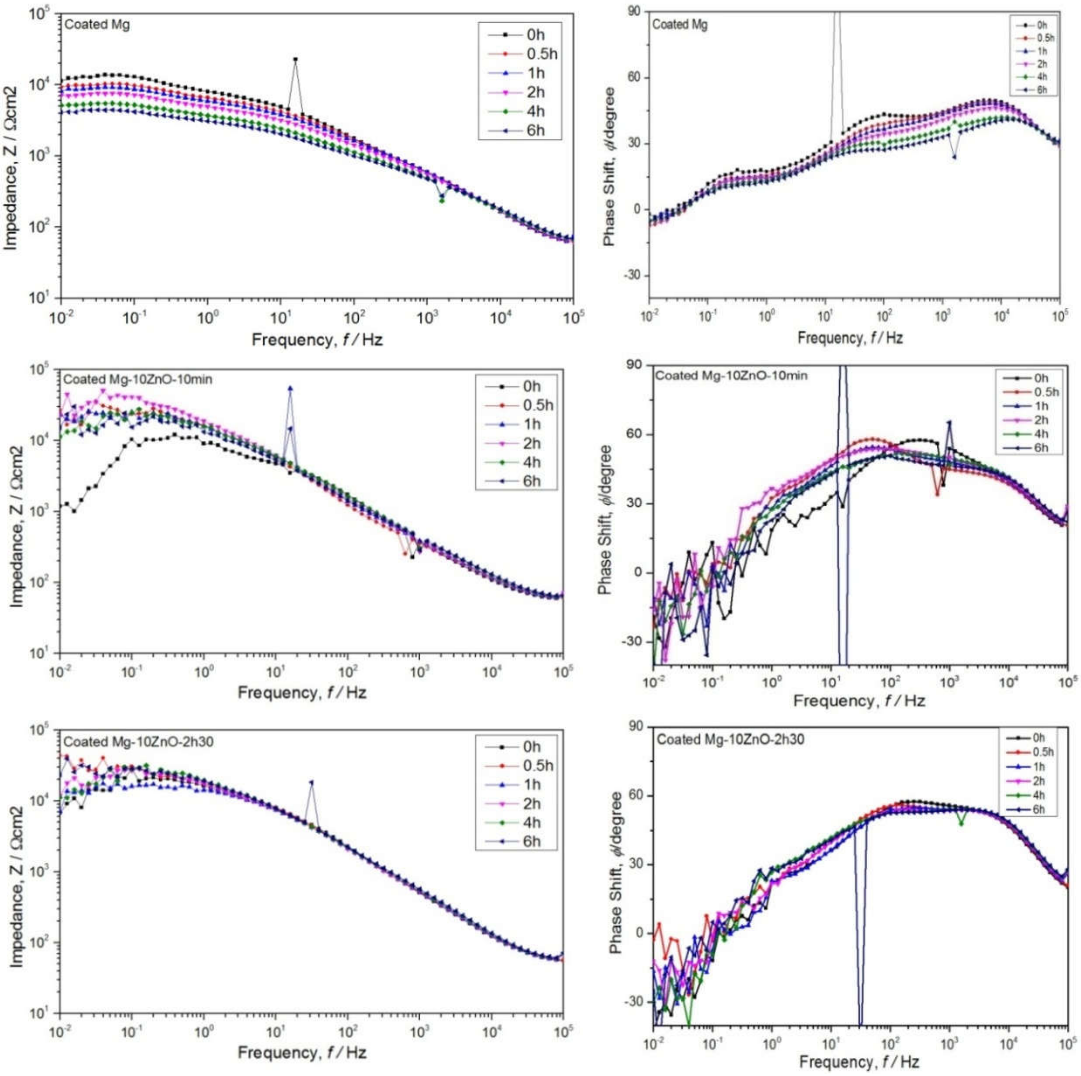

Figure 4.12. Bode plots of HAp coated sample immersed in Hank’s solution.

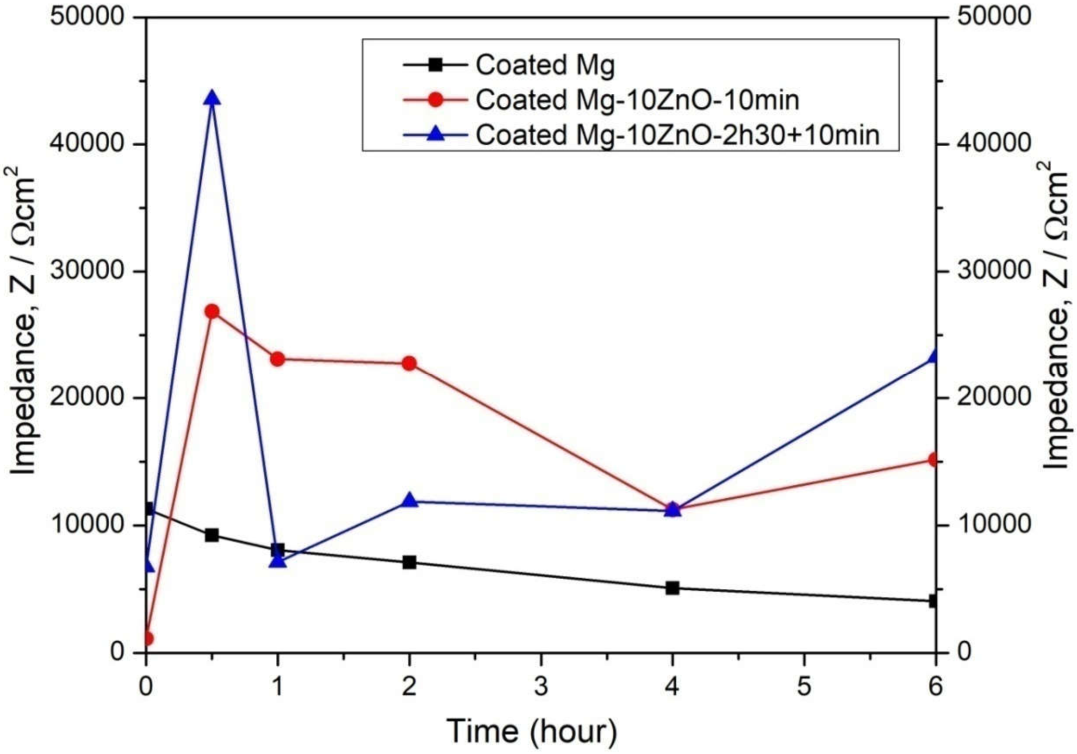

Figure 4.17. Impedance of coated samples at different immersion periods.

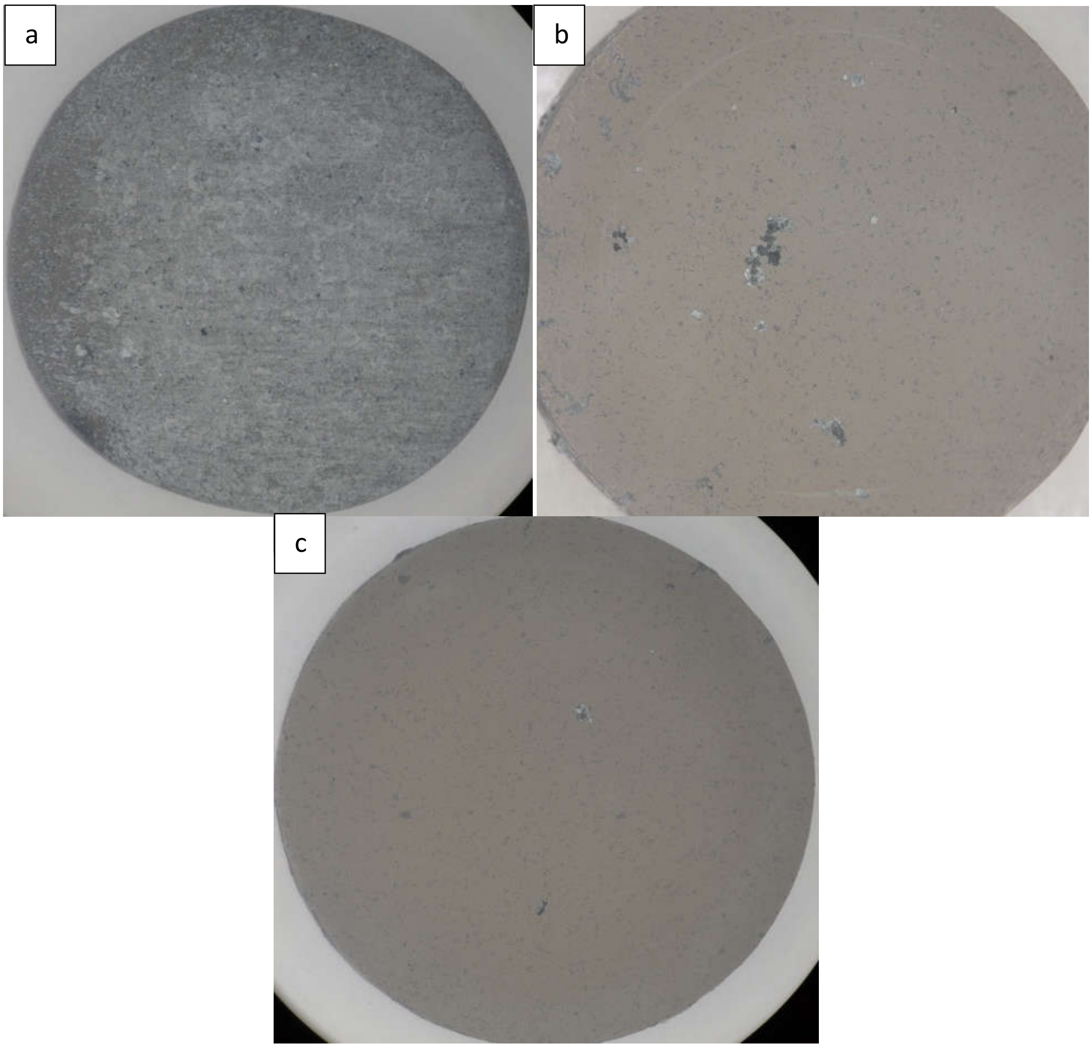

Figure 4.19. Surface morphology of HAp coated samples after impedance tests: a) HAp coated Mg, b) HAp coated Mg-10ZnO-10min, and c) HAp coated Mg-10ZnO-2h30+10min.

4.4. Conclusion

HAp coating was carried out successfully on as fabricated composites. The results of suggested that:

- HAp grows homogeneously on the surfaces of pure sintered Mg as well as composites.
- HAp layer on the surface of composites is thicker than that on pure Mg
- The structure of HAp layer consisting of two sub-layer: inner dense subl-layer and outer plate like sub-layer
- HAp coating improves significantly the corrosion resistance of the as fabricated composites, especialy HAp coated Mg-10ZnO-2h30+10min.
- Corrosion product deposited on the surface of HAp coated Mg-10ZnO-10min after 14 days of immersion contains some calcium phosphate, while HAp is main component on the surface of immersed HAp coated Mg-10ZnO-2h30+10min.
- Based on these results, HAp coating is considered as good method for improving corrosion resistance of Mg matrix composites.

Reference

[1] Peter H, Mordike BL. Physical metallurgy. In: Friedrich HE, Mordike BL, editors.
Magnesium technology –metallurgy, design data, applications. Berlin: Springer; 2006. p. 76–7.

[2] Staiger MP, Pietak AM, Huadmai J, Dias G. Magnesium and its alloys as orthopedic biomaterials: A review. Biomaterials. 27, 2006, 1728-1734.

[3] Meisam S, Yuebin G. Biodegradable Orthopedic Magnesium-Calcium (MgCa) Alloys, Processing, and Corrosion Performance. Materials. 2012, 5, 135–155.

[4] Witte F, Hort N, Vogt C, Cohen S, Kainer KU, Willumeit R, Feyerabend F. Degradable biomaterials based on magnesium corrosion. Curr.Opin.Solid State Mater. Sci. 12, 2008, 63–72.

[5] Witte F, Fischer J, Nellesen J, Crostack HA, Kaese V, Pisch A, Beckmann FS, Windhagen H. In vitro and in vivo corrosion measurements of magnesium alloys. Biomaterials. 27, 2006, 1013-1018.

[6] Sikora-Jasinska M, Paternoster C, Mostaed E, Tolouei R, Casati R, Vedani M, Mantovani D. Synthesis, mechanical properties and corrosion behavior of powder metallurgy processed Fe/Mg_2Si composites for biodegradable implant applications. Materials science & engineering. C. 2017, 81, 511-521.

[7] Al-Abdullat Y, Tsutsumi S, Nakajima N, Ohta M, Kuwahara H, Ikeuchi K. Surface Modification of Magnesium by NaHCO3 and Corrosion Behavior in Hank's solution for New Biomaterial Applications. Mater. Trans. 42, 2001, 1777–1780.

[8] Longchuan L, Jiacheng G, Yong W. Evaluation of cyto-toxicity and corrosion behavior of alkali-heat-treated magnesium in simulated body fluid. Surf. Coat. Tech. 185, 2004, 92–98.

[9] Song YW, Shan DY, Han EH. Electrodeposition of hydroxyapatite coating on AZ91D magnesium alloy for biomaterial application. Mater. Lett. 62, 2008, 3276–3279.

[10] Yang JX, Jiao YP, Cui FZ, Lee IS, Yin QS, Zhang Y. Modification of degradation behavior of magnesium alloy by IBAD coating of calcium phosphate. Surf. Coat. Tech. 202, 2008, 5733–5736.

[11] Cuilian W, Shaokang G, Li P, Chenxing R, Xiang W, Zhonghua H. Characterization and degradation behavior of AZ31 alloy surface modified by bone-like hydroxyapatite for implant applications. Appl. Surf. Sci. 255, 2009, 6433–6438.

[12] Zhang Y, Zhang G, Wei M. Controlling the biodegradation rate of magnesium using biomimetic apatite coating. J. Biomed. Mater. Res. 89B, 2009, 408–414.

[13] Hideyuki K, Al-Abdullat Y, Naoko M, Sadami T, Tatsuhiko A. Precipitation of Magnesium Apatite on Pure Magnesium Surface during Immersing in Hank's Solution. Mater. Trans. 42, 2001, 1317–1321.

[14] Hiromoto S, Shishido T, Yamamoto A, Maruyama N, Somekawa H, Mukai T. Precipitation control of calcium phosphate on pure magnesium by anodization. Corr. Sci. 50, 2008, 2906–2913.

[15] Hiromoto S, Tomozawa M. Hydroxyapatite coating of AZ31 magnesium alloy by a solution treatment and its corrosion behavior in NaCl solution. Surf. Coat. Technol. 205, 2011, 4711–4719.

[16] Hiromoto S, Tomozawa M. Corrosion Behavior of Magnesium with Hydroxyapatite coatings Formed by Hydrothermal Treatment. Mater. Trans. 51, 2010, 2080–2087.

[17] Hiromoto S, Inoue M, Taguchi T, Yamane M, Ohtsu N. In vitro and in vivo biocompatibility and corrosion behaviour of a bioabsorbable magnesium alloy coated with octacalcium phosphate and hydroxyapatite. Acta Biomater. 11, 2015, 520–530.

[18] Mann CK, Yoe JH. Spectrophotometric determination of magnesium with sodium 1-azo-2-hydroxy-3-(2,4-dimethylcarboxanilido)-naphthalene-1-(2-hydroxybenzene-5-sulfonate). Anal Chem. 28, 1956, 202–205.

[19] Watanabe H, Tanaka H. Dual-wavelength spectrophotometric determination of magnesium with xylidyl blue I and nonionic surfactant. Bunseki-kagaku. 26, 1977, 635–639.

CHAPTER 5

IN VITRO BIOCOMPATIBILITY OF Mg MATRIX *IN SITU* COMPOSITES FABRICATED BY SPARK PLASMA SINTERING

5.1 Introduction

Magnesium alloys and magnesium matrix composites are potential candidates for biodegradable materials including temporary implants and cardiovascular devices [1–5]. As for cardiovascular device application, magnesium materials have demonstrated excellent progress in practical applications [1,4,6–9]. However, as for the temporary implant applications, fast biodegradation of magnesium materials result in deterioration of material strength and some concerns related to biocompatibility of these materials [2,10,11]. Many techniques have been studies to improve the corrosion resistance and biocompatibility of magnesium materials for practical application including adding alloy elements, surface modification [12–16]. However, most of the past researches show limitation in improvement of corrosion resistance of Mg matrix composites. In previous chapters, we have develoloped successfully new Mg matrix in situ composites with superior mechanical properties as well as good corrosion resistance from initial Mg and ZnO powder via spark plasma sintering (SPS) method. HAp coating for as fabricated composites by hydrothermal treatment method was carried out successfully. The results suggested that the HAp coating played as vital role in the improvement of corrosion resistance of Mg matrix composites *in vitro.* In this study, the *in vitro* biocompatibility of HAp coated and uncoated Mg matrix *in situ* composites have been evaluated by cell culture tests in MEM-α medium. Cell viability was evaluated by Giemsa staining method.

5.2. Experimental Procedures

5.2.1. Sample preparation

Mg powders with a purity of 99.5% and particle size of 180 μm and ZnO powders with a purity of 99.9% and particle size of 1 μm supplied by Kujundo Chemical Laboratory were used for sample preparation. Mg-10 wt-%ZnO powders was mixed homogeneously with zirconia balls (2.5 of ball to powder weight ratio) in an argon atmosphere using a planetary micro ball mill (Pulverisette 7) with rotation speed of 500 rpm for 12 h. No process control agent was used. The mixed powders were set inside the Tungsten-Carbide die of 120 mm in height and 15 mm in an inner diameter for the spark plasma sintering using a 511S, Syntex SPS system.

Three kinds of samples were fabricated with different ZnO weight fractions and sintering conditions. Mg-10ZnO-10min sample was directly sintered by SPS while Mg-10ZnO-2h30+10min sample was sintering in vacuum furnace before sintering by SPS. The details of fabrication process are shown in Table 5.1.

All the sintering processes were performed in a high vacuum chamber. After sintering processes, the samples were cooled down to room temperature inside the vacuum chamber.

Table 5. 1.Sample names and treatment conditions.

Sample name	**Composition**	**Sintering by vacuum furnace (T=550^{o}C, P=0MPa)**	**Sintering by SPS (T=550^{o}C, P=50MPa)**
Mg	Pure Mg powder	0	10 min
Mg-10ZnO-10min	Mg-10 mass% ZnO	0	10 min
Mg-10ZnO-2h30+10min	Mg-10 mass% ZnO	2h30	10min

5.2.2. HAp coating process

The sintered composites were machined into disk shape with the size of $\Phi 15 \times 2$ (mm). The machined samples were ground using SiC papers up to 4000 grit, successively polished with ¼-µm diamond paste, ultrasonically cleaned with ethanol and then dried for HAp coating process. Treatment solutions for HAp coatings were prepared with ethylenediaminetetraaceticacid calcium disodium salt hydrate ($C_{10}H_{12}CaN_2Na_2O_8$, Ca-EDTA), potassium dihydrogen phosphate (KH_2PO_4), and sodium hydroxide (NaOH). The pH of the solution will be adjusted to be 7.6 by NaOH solution The discs were immersed in the treatment solution at 90 ^{o}C for 2 h. The HAp coating process is illustrated in figure 5.1.

The coated samples then were characterized by XRD, OM, and BSEM to evaluate the growth of HAp coating layer.

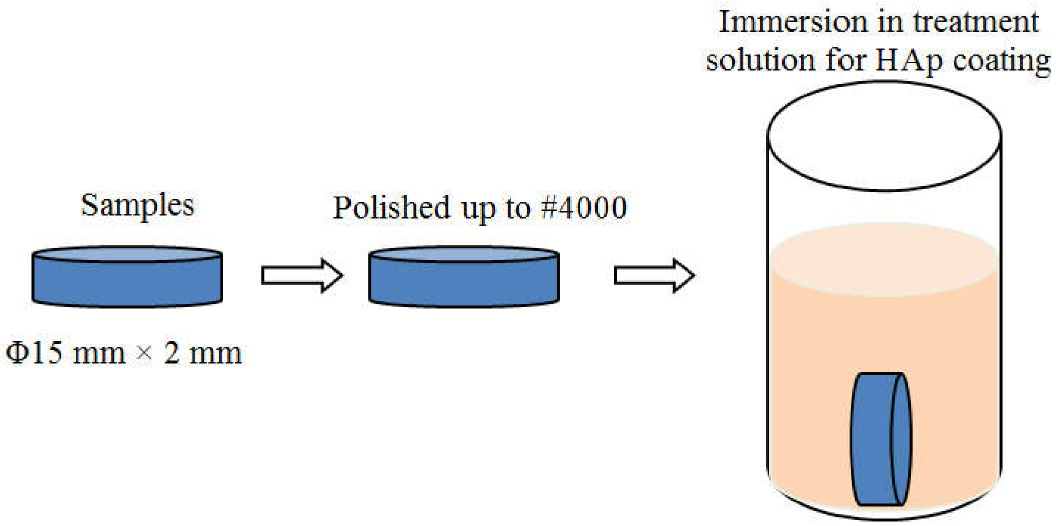

Figure 5.1. Illustration of HAp coating process

5.2.3. *In vitro* biocompatibility investigation

As-coated samples were then investigated the *in vitro* biocompatibility by cell culture tests. Cell culture tests were carried out using MC3T3-E1 cell line in MEM-α medium supplemented with 10 vol.% fetal bovine serum for 1, 2, and 3 days respectively at 37 ± 0.5 ^{o}C. The cell density in cell culture tests was 2,500 cell/cm^2.

After immersion in the medium for 1, 2, or 3 days, the samples were removed from the medium for cell counting by Giemsa staining method.

5.3. Results and Discussion

5.3.1. HAp growth

Figure 5.2 shows XRD patterns of 2h coated Mg, Mg-10ZnO-10min, and Mg-10ZnO-2h30 samples. It can be seen that all samples show high peaks of HAp and there were no peaks related to OCP detected. This demonstrated good growth of HAp on the surface of all samples. However, peaks related to HAp on composites samples show higher intensity compared to those on coated pure sintered Mg. This suggested better growth of HAp on composites than on pure Mg.

Figure 5.3 shows morphology of samples before and after HAp coating. It can be seen from morphology of coated samples that HAp coating layer grows homogeneously on the surface of composites as well as pure Mg. The color of the coated samples suggested that HAp layers on the composites are thicker than on pure Mg. This is in agreement with result in previous chapter.

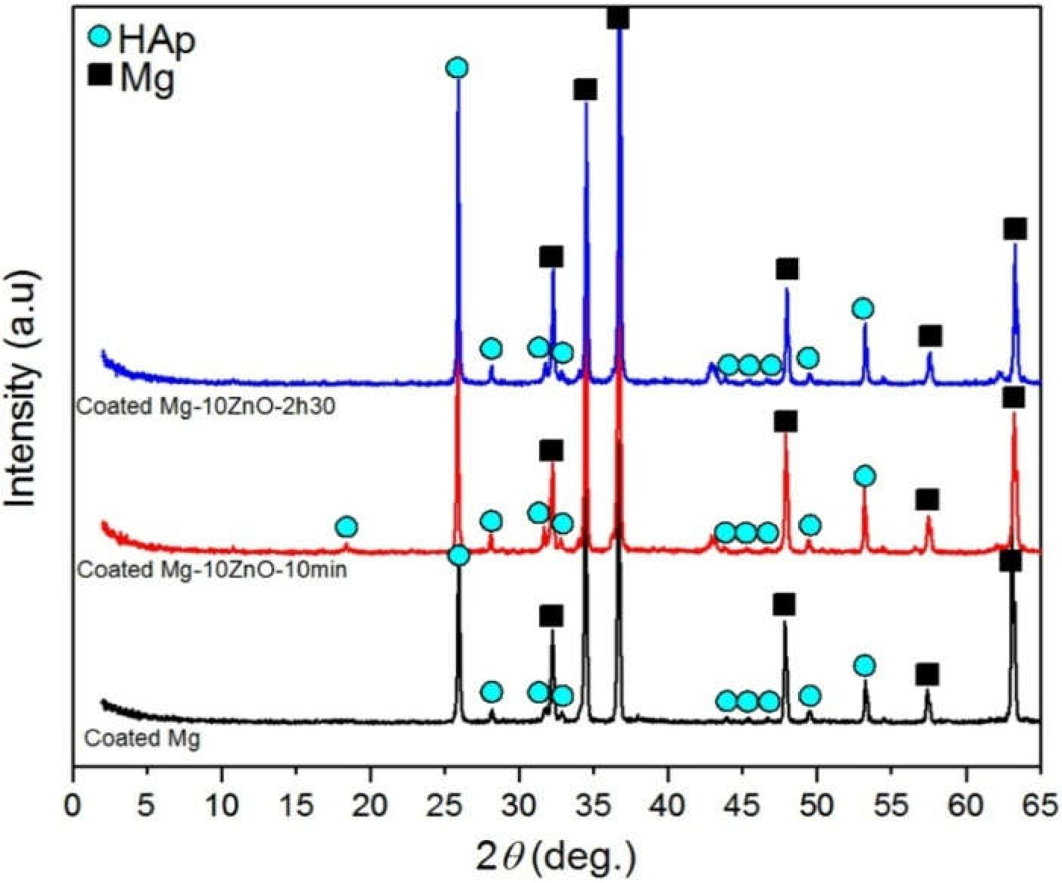

Figure 5.2. XRD patterns of 2h coated Mg, Mg-10ZnO-10min, and Mg-10ZnO-2h30+10min.

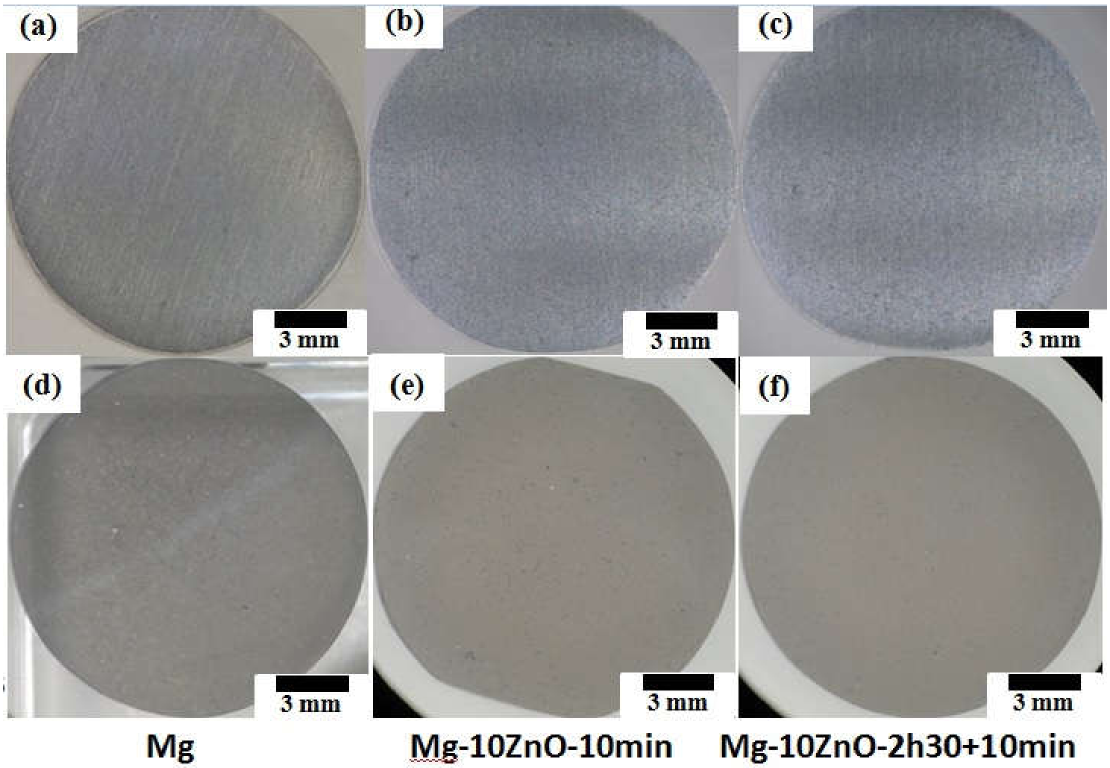

Figure 5.3. Morphology of samples before and after HAp coating
(a), (b), and (c): Before coating
(d), (e), and (f): After coating

5.3.2. Cell viability

Figure 5.4 and Figure 5.5 show surface morphology of uncoated samples after cell culture test for 1, 2, and 3 days in MEM-α medium. It can be seen that, after one day, pure Mg sample was corroded severely on whole surface. There is no cell remained on this sample after 1 day. On the other hand, the surface of composite samples were only corroded locally at some points after 1 day. There are many cell survived on the surface of composites samples after 1 day. After 2 days of immersion, pure Mg sample was corroded more severely and corrosion product covered entire surface of this sample. Mg-10ZnO-10min sample was also corroded seriously after 2 days of immersion. There is no cell survived on the surface of this sample after 2 day and there is corrosion product deposited on majority of the sample surface. As for Mg-10ZnO-2h30+10min sample, the surface is almost the same with the surface of sample after 1 day of immersion. There is local corrosion at some points on this surface. However, cell still can survive well on this sample after 2 days, and it seems that cell density increased compared to that on the surface of sample immersed for 1 day. After 3 days of immersion, pure Mg sample was covered by very thick layer of corrosion product. Corrosion product also covered almost entire surface of Mg-10ZnO-10min sample. There is no cell survived on the surface of 2 above samples. As for Mg-10ZnO-2h30+10min sample, corrosion occurred at bigger areas. Although majority of sample surface was not corroded, the effect of corrosion on other areas affecting on cell viability. It seems that there are only few cells remained on this sample after 3 days.

The survival of cell decreased by the time can be explained as following.

As for pure Mg sample, corrosion occurred immediately after immersing the sample into the medium. Due to severe corrosion, hydrogen gas released quickly avoiding cells attach on to the surface of the sample. This lead to all of cell on this well can not survive after only 1 day.

As for the composites, corrosion did not occurred during the first day of immersion. Thereofore, there is almost no hydrogen gas released during this time. And cell can survive well during the first day of immersion. After that, severe corrosion occurred on the surface of Mg-10ZnO-10min sample resulting in hydrogen gas evolution. Consequently, no cell remained on this sample after 2 days of immersion. The similar phenomena occurred for the Mg-10ZnO-2h30+10min sample. However, the process taked place slower than on Mg-10ZnO-10min sample because corrosion resistance of Mg-10ZnO-2h30+10min sample is better than that of Mg-10ZnO-10min sample. As for Mg-10ZnO-2h30+10min sample, there are many cell remained on the surface of this sample after 2 days of immersion. After 3 days of immersion, the corrosion occurred but not very severe. Only some parts on the surface corroded and only little corrosion product deposited on the surface of this sample. However, due to corrosion occurred and hydrogen gas released, cell density decreased significantly compared to that on the surface of sample immersed for 2 days.

Figure 5.6 shows high magnification of the surface of Mg-10ZnO-2h30+10min sample after 3 days of immersion. It could be seen that, on the corroded areas, the is no cell remained. Some corrosion product deposited on some regions of corroded areas. On the other hand, there are some cell survived on the non-corroded regions of the surface. This indicates that, cell viability strongly depends on the corrosion or hydrogen gas released rate of the sample.

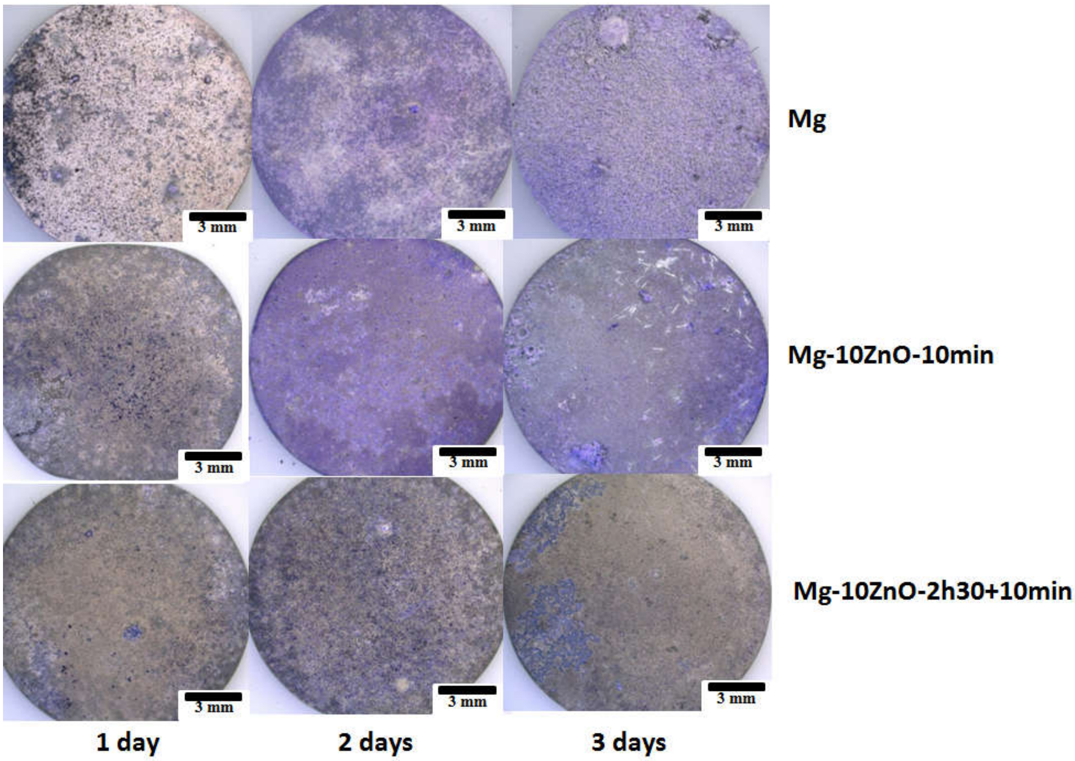

Figure 5.4. Surface morphology of uncoated samples after cell culture test for 1, 2, and 3 days in MEM-α medium.

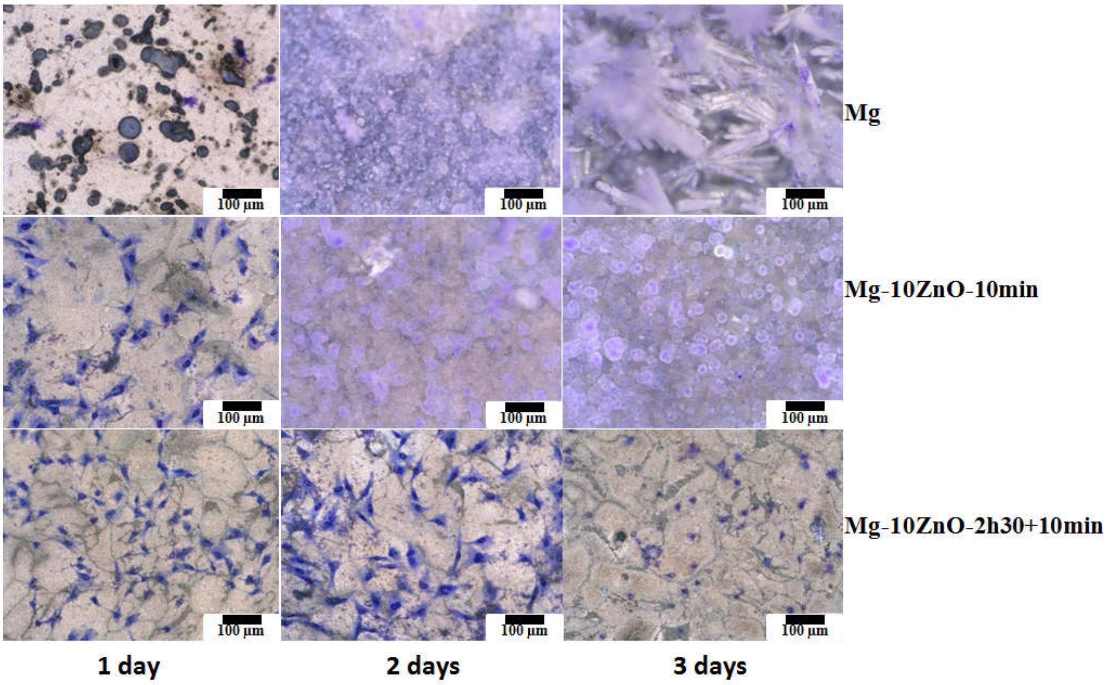

Figure 5.5. Surface morphology of uncoated samples after cell culture test for 1, 2, and 3 days in MEM-α medium.

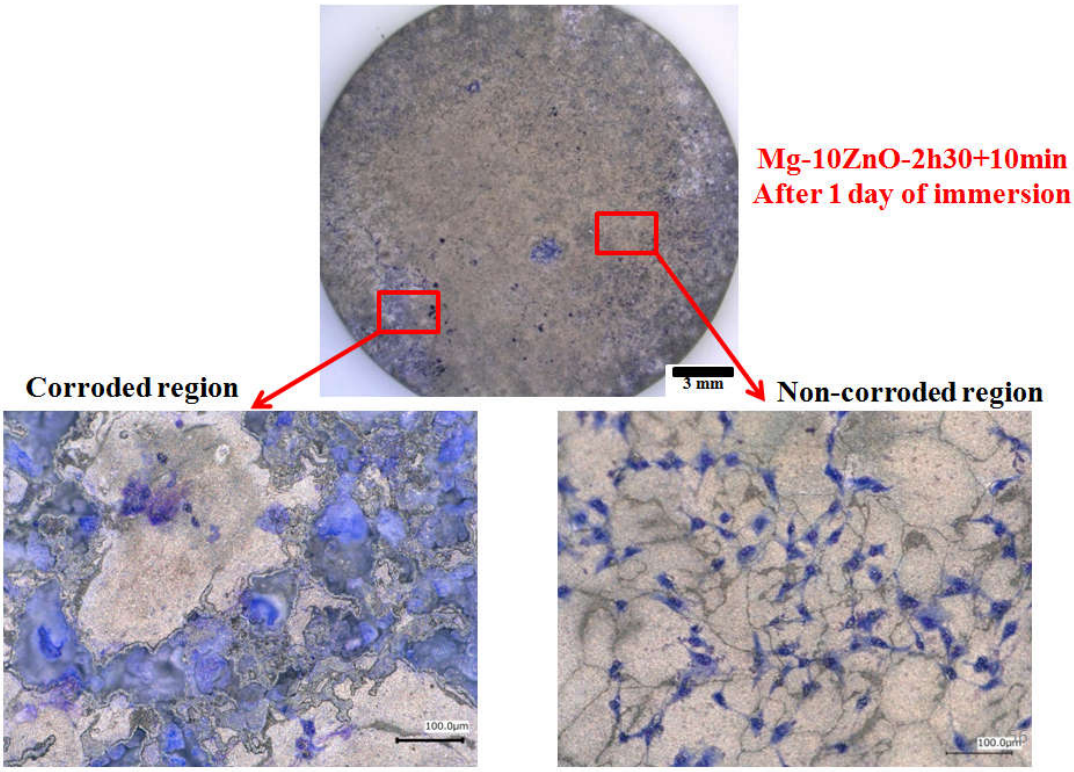

Figure 5.6. High magnification of the surface of Mg-10ZnO-2h30+10min sample after 3 days of immersion

Figure 5.7 and Figure 5.8 show surface morphology of HAp coated samples after cell culture test for 1, 2, and 3 days in MEM-α medium. As could be seen that, as for HAp coated Mg sample, there are some local corrosion occurred after 1 day of immersion. However, majority of samples surface was protected from corrosion. There many cells survived on the surface of this sample after 1 day of immersion. As for the sample immersed for 2 days, corrosion occurred over almost entire suface of sample. Corrosion product deposited and covered on whole surface. There is almost no cells remained on this sample after 2 days of immersion. After 3 days of immersion, HAp coated Mg sample was corroded more severely. There is a thick layer of corrosion product covered entire surface of this sample.

As for HAp coated composites samples, both HAp coated Mg-10ZnO-10min and HAp coated Mg-10ZnO-2h30+10min samples show very good cell viability. There is almost no corrosion occurred on the surface of both HAp coated composites after 3 days of immersion. This indicates that, HAp coating is very effective in improvement of corrosion resistance of the as fabricated composites, and consequently, improve significantly *in vitro* biocompatibility of the composites. The cell density on both composites increases gradually after evey day suggesting good biocompatibility. As for comparison between two composites, cell density on surface of HAp coated Mg-10ZnO-2h30+10min sample is higher than that on surface of HAp coated Mg-10ZnO-10min sample. This is in agreement with corrosion test results since HAp coated Mg-10ZnO-2h30+10min sample has better corrosion resistance compared to HAp coated Mg-10ZnO-10min sample.

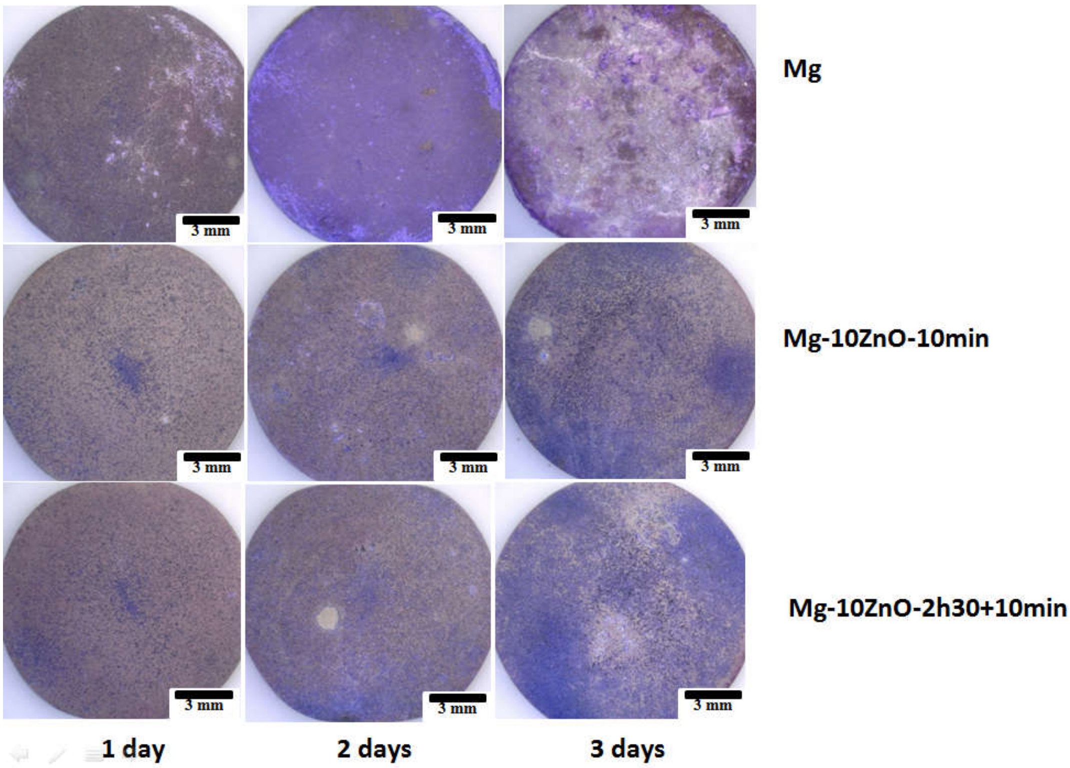

Figure 5.7. Surface morphology of HAp coated samples after cell culture test for 1, 2, and 3 days in MEM-α medium.

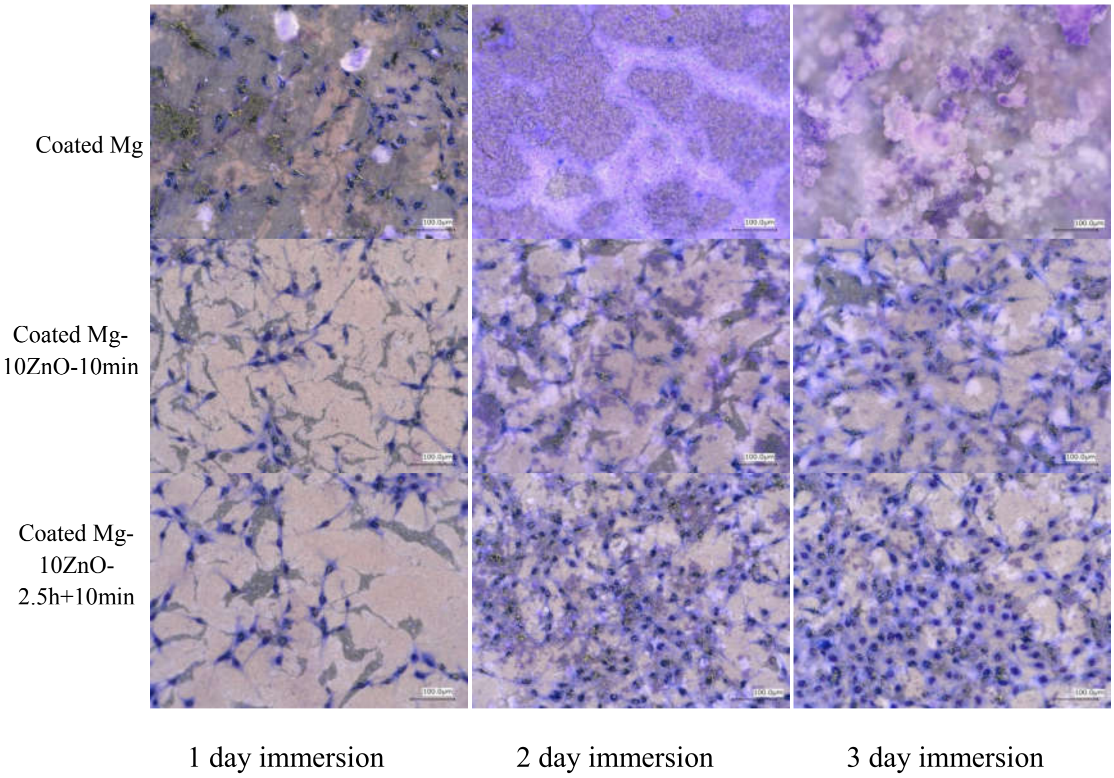

Figure 5.8.Surface morphology of HAp coated samples after cell culture test for 1, 2, and 3 days in MEM-α medium.

5.4. Conclusion

In vitro biocompatibility of HAp coated and uncoated Mg matrix *in situ* composites was investigated by cell culture tests for 1, 2, and 3 days respectively. The results can be summarized as follows:

- Corrosion resistance plays an important role in the cell viability on the surface of uncoated composites.
- High hydrogen gas released rate results in death of cell on the surface of uncoated composites.
- HAp coating improves significantly the corrosion resistance of the composites, resulting in improving significantly cell viability on the surface of coated composites.
- The improvement of cell viability on the surface of the composites might be originated from the preventing of high hydrogen gas released rate at the beginning of immersion. This is very important role of HAp coating on the cell viability on the composite surface.

The results suggest that HAp coated Mg matrix composites are potential candidates for temporary implant applications.

Reference

[1] Heublein B, Rohde R, Kaese V, Niemeyer M, Hartung W, Haverich A. Biocorrosion of magnesium alloys: a new principle in cardiovascular implant technology. Heart. 89, 2003, 651–656.

[2] Staiger MP, Pietak AM, Huadmai J, Dias G. Magnesium and its alloys as orthopedic biomaterials: a review. Biomaterials. 27, 2006, 1728–1734.

[3] Witte F, Calliess T, Windhagen H. Biodegradable synthetic implant materials. Clinical applications and immunological aspects. Orthopade. 37, 2008, 125–130.

[4] R. Zeng, W. Dietzel, F. Witte, N. Hort, C. Blawert. Progress and challenge for magnesium alloys as biomaterials. Adv Biomater 10, 2008, B3–B14.

[5] F. Witte. The history of biodegradable magnesium implants: a review. Acta Biomater 6, 2010, 1680–1692.

[6] Waksman R, Pakala R. Biodegradable and bioabsorbable stents. Curr Pharm Des. 16, 2010, 4041–4051.

[7] Zartner P, Buettner M, Singer H, Sigler M. First biodegradable metal stent in a child with congenital heart disease: evaluation of macro and histopathology. Catheter Cardiovasc Interv. 69, 2007, 443–446.

[8] Erbel R, Di Mario C, Bartunek J, Bonnier J, de Bruyne B, Eberli FR, Erne P, Haude M, Heublein B, Horrigan M, Ilsley C, Böse D, Koolen J, Lüscher TF, Weissman N, Waksman R. Temporary scaffolding of coronary arteries with bioabsorbable magnesium stents: a prospective, non-randomised multicentre trial. Lancet. 369, 2007, 1869–1875.

[9] Haude M, Erbel R, Erne P, Verheye S, Degen H, Böse D, Vermeersch P, Wijnbergen I, Weissman N, Prati F, Waksman R, Koolen J. Safety and performance of the drug-eluting absorbable metal scaffold (DREAMS) in patients with de-novo coronary lesions: 12 month results of the prospective, multicentre, first-in-man BIOSOLVE-I trial. Lancet. 381, 2013, 836–844.

[10] Witte F, Feyerabend F, Maier P, Fischer J, Störmer M, Blawert C, Dietzel W, Hort N. Biodegradable magnesium-hydroxyapatite metal matrix composites. Biomaterials. 28, 2007, 2163–2174.

[11] Jan-Marten Seitz, Janin Reifenrath, Andreas Weizbauer, Friedrich-Wilhelm Bach, Andrea Meyer-Lindenberg, Berend Denkena, Henning Windhagen. Biodegradable magnesium implants for orthopedic applications. J Mater Sci. 48, 2013, 39–50.

[12] Kuwahara H, Al-Abdullat Y, Mazaki N, Tsutsumi S, Aizawa T. Precipitation of magnesium apatite on pure magnesium surface during immersing in Hank's solution. Mater Trans. 42, 2001, 1317–1321.

[13] Al-Abdullat Y, Tsutsumi S, Nakajima N, Ohta M, Kuwahara H, Ikeuchi K. Surface Modification of Magnesium by NaHCO3 and Corrosion Behavior in Hank's solution for New Biomaterial Applications. Mater. Trans. 42, 2001, 1777–1780.

[14] Longchuan L, Jiacheng G, Yong W. Evaluation of cyto-toxicity and corrosion behavior of alkali-heat-treated magnesium in simulated body fluid. Surf. Coat. Tech. 185, 2004, 92–98.

[15] Shadanbaz S, Dias GJ. Calcium phosphate coatings on magnesium alloys for biomedical applications: a review. Acta Biomater. 8, 2012, 20–30.

[16] Hornberger H, Virtanen S, Boccaccini AR. Biomedical coatings on magnesium alloys – a review. Acta Biomater. 8, 2012, 2442–2455.

CHAPTER 6
GENERAL CONCLUSIONS

Chapter 1: In this chapter, general introduction, motivation, background for research have been discussed. Research methodology including material and fabrication technique were described as well. It is concluded that, Mg matrix *in situ* composites are potential objective of research for biomedical applications.

Chapter 2: In this chapter, Mg matrix *in situ* composites were fabricated from Mg and ZnO powder via ball mixing and spark plasma sintering. XRD analysis indicated that *in situ* reactions occurred during sintering process producing MgO, Zn and Mg–Zn intermetallic compounds. The formation of *in situ* products strongly contributed to the enhancement of the strength and the ductility of the fabricated composites compared with pure Mg. Specifically, the highest strength at 380 MPa was observed in the Mg-20 wt-% ZnO composite, and the highest failure strain at 12.9% was achieved in the Mg-5 wt-% composite compared with the 156 MPa strength and the 10.2% failure strain of pure Mg. In addition, the strengths of as-produced composites are as double as that of cortical bones. The mechanical properties of the fabricated composites are considered as very potential candidate for biomedical load-bearing applications.

Chapter 3: In this chapter, *in vitro* corrosion properties of fabricated Mg matrix *in situc* composites were evaluated by immersion and by electrochemical tests using Hanks' solution. The results showed that the formation of in situ products improved significantly the corrosion resistance of the fabricated composites compared with pure Mg; Mg-10 wt % ZnO composites especially exhibited the lowest corrosion rate. In addition, an energy-dispersive X-ray (EDX) analysis showed that calcium phosphate formed as a corrosion product on the surface of Mg-10 wt % ZnO composites, while Mg(OH)2 appeared as a corrosion product on the surface of Mg-20 wt % ZnO composite. The findings suggested Mg-10 wt % ZnO composite have good corrosion resistance for temporary implant application.

Chapter 4: HAp coating was carried out successfully on as fabricated composites. The results of suggested that:

- HAp grows homogeneously on the surfaces of pure sintered Mg as well as composites.
- HAp layer on the surface of composites is thicker than that on pure Mg
- The structure of HAp layer consisting of two sub-layer: inner dense subl-layer and outer plate like sub-layer
- HAp coating improves significantly the corrosion resistance of the as fabricated composites, especialy HAp coated Mg-10ZnO-2h30+10min.
- Corrosion product deposited on the surface of HAp coated Mg-10ZnO-10min after 14 days of immersion contains some calcium phosphate, while HAp is main component on the surface of immersed HAp coated Mg-10ZnO-2h30+10min.
- Based on these results, HAp coating is considered as good method for improving corrosion resistance of Mg matrix composites.

Chapter 5: *In vitro* biocompatibility of HAp coated and uncoated Mg matrix *in situ* composites was investigated by cell culture tests for 1, 2, and 3 days respectively. The results can be summarized as follows:

- Corrosion resistance plays an important role in the cell viability on the surface of uncoated composites.
- High hydrogen gas released rate results in death of cell on the surface of uncoated composites.
- HAp coating improves significantly the corrosion resistance of the composites, resulting in improving significantly cell viability on the surface of coated composites.
- The improvement of cell viability on the surface of the composites might be originated from the preventing of high hydrogen gas released rate at the beginning of immersion. This is very important role of HAp coating on the cell viability on the composite surface.

The results suggest that HAp coated Mg matrix composites are potential candidates for temporary implant applications.

ACKNOWLEDGEMENTS

First of all, I would like to express my deepest thanks to my supervisor, Prof. Equo KOBAYASHI for his strong support and kind advice during my graduate program at Tokyo Institute of Technology. I learned a lot from his guidance, advice, and great motivation when I have some difficulties in my research.

I also would like thanks Prof. Tatsuo Sato who also helps me a lot with many critical advices during my first period of studies.

Special thanks to Prof. Takeyama, Prof. Kawamura, Prof. Ueda, and Prof. Kimura for allowing me using facilities for my research

I also would like to express my sincere thanks to Dr. HIROMOTO Sachiko – National Institute for Materials Science for accepting me as intership student, strongly support for my corrosion and cell culture experiments.

Last but not least, I would like to thanks all of my labmates who always support me thoughout my program. I really appreciated their help in both research and daily matters.

Once again, thank you very much for all of your support for my completion of this thesis.